

NPS ARCHIVE
1961
PETERSEN, E.

AN INVESTIGATION OF THE EARLY WAKE
BEHIND SUBMERGED FLAT PLATES AS INFLUENCED
BY TRAILING EDGE CONFIGURATION

EDWIN J. PETERSEN, JR.
and
GERALD D. SYLVESTER

LIBRARY
U.S. NAVAL POSTGRADUATE SCHOOL
MONTEREY, CALIFORNIA

AN INVESTIGATION OF THE EARLY WAKE
BEHIND SUBMERGED FLAT PLATES
AS INFLUENCED BY
TRAILING EDGE CONFIGURATION

by

LIEUTENANT EDWIN J. PETERSEN, JR., U. S. NAVY

B.S., U. S. Naval Academy

(1953)

and

LIEUTENANT GERALD D. SYLVESTER, U. S. NAVY

B.S., U. S. Naval Academy

(1952)

SUBMITTED IN PARTIAL FULFILLMENT OF THE REQUIREMENTS
FOR THE MASTER OF SCIENCE DEGREE IN NAVAL ARCHITECTURE
AND MARINE ENGINEERING AND THE PROFESSIONAL DEGREE,
NAVAL ENGINEER

at the

MASSACHUSETTS INSTITUTE OF TECHNOLOGY

May, 1961

AN INVESTIGATION OF THE EARLY WAKE BEHIND SUBMERGED FLAT PLATES AS INFLUENCED BY TRAILING EDGE CONFIGURATION

by

Lieutenant Edwin J. Petersen, Jr., U. S. Navy

and

Lieutenant Gerald D. Sylvester, U. S. Navy

Submitted to the Department of Naval Architecture and Marine Engineering on 20 May 1961 in partial fulfillment of the requirements for the Master of Science Degree in Naval Architecture and Marine Engineering and the Professional Degree, Naval Engineer.

ABSTRACT

This report presents the results of an experimental investigation of the behavior of the turbulent early wake behind three flat plates of varying trailing edge configuration submerged in water.

The circumstances surrounding "singing" propellers and the influence of vortex formation upon this and other hydroelastic vibration phenomena are discussed. The significance of the vortex as a forcing function is emphasized.

The influence of plate vibration upon the early wake is essentially eliminated in the investigation by rigidly clamping the test plates.

A prediction of plate profile drag coefficient and of dimensionless shedding frequency, the Strouhal number, is made based upon von Karman's vortex street analysis.

The longitudinal and transverse distribution of local mean velocity, turbulence intensity, and static pressure were measured in the early wake of three selected test plates of varying trailing edge configuration. Turbulence energy density spectra were obtained at selected positions in the early wake. Profile drag coefficients were computed and vortex shedding frequencies measured, and are compared with predicted values.

Thesis Supervisor: James W. Daily
Title: Professor of Hydraulics

ACKNOWLEDGEMENTS

The authors wish to express their appreciation for the guidance and assistance of Dr. J. W. Daily, Professor of Hydraulics, Thesis Supervisor, and of Dr. P. S. Eagleson, Assistant Professor of Hydraulic Engineering.

The investigation reported herein was conducted in the Hydrodynamics Laboratory of the Department of Civil and Sanitary Engineering at the Massachusetts Institute of Technology, Dr. A. T. Ippen, Professor of Hydraulics, Director.

The authors wish further to express their gratitude to LCDR J. R. Baylis, USN, Associate Professor of Naval Engineering; to Mr. F. E. Perkins, Mr. G. Noutsopoulos, Mr. R. A. Grace, and Mr. C. J. Huval of the Hydrodynamics Laboratory; to Mr. J. O. Silvey of the Servomechanisms Laboratory, Massachusetts Institute of Technology; and to Mr. J. P. Doughan of the Portsmouth Naval Shipyard; all of whom gave valuable assistance during phases of this investigation.

TABLE OF CONTENTS

	<u>Page</u>
Title Page	1
Abstract	11
Acknowledgements	111
Table of Contents	1v
List of Figures	v11
List of Tables	viii1
List of Symbols	1x
I. Introduction	1
A. General Statement of the Problem	1
B. Scope of the Investigation	3
II. Review of Previous Work	6
A. Vortex Excited Blade Vibration	6
B. Vortex Formation and Wake Periodicity	7
C. Wake Structure	9
D. Trailing Edge Geometry	9
E. Turbulence	10
III. Theoretical Considerations	12
A. Analysis of the Vortex Street	12
IV. Description of Equipment and Instrumentation	17
A. The Variable Flow Water Tunnel	17
B. Test Plates	20
C. Test Plate Mounting	20
D. Traversing Mechanism	21
E. Flow Measurement Devices	21
1. Turbulence Pressure Transducer	21
2. Transducer Response	24
3. Total Head and Static Pressure Tubes	27

4.	Contraction Manometer	27
F.	Electronics Equipment	27
1.	Electrometer Preamplifier	29
2.	Amplifier	29
3.	Wave Analyzer	32
4.	Voltmeters	32
5.	Oscilloscope	32
V.	Conduct of the Investigation	34
A.	Ambient Turbulence	34
B.	Wake Survey Measurements	34
C.	Wake Energy Spectrum Measurements	35
D.	Longitudinal Variation Measurements	35
E.	Calibration of Equipment	35
F.	Flow Duplication	36
VI.	Reduction of Data	37
A.	Mean Flow Velocity	37
B.	Mean Local Velocity	37
C.	Turbulence Intensity	37
D.	Static Pressure	38
E.	Normalized Turbulence Energy Density	38
F.	Profile Drag Coefficient	38
VII.	Results of the Investigation	40
A.	Wake Structure	40
B.	Profile Drag Coefficients	43
C.	Vortex Shedding Frequencies	44
D.	Turbulence Energy	48
VIII.	Conclusions	56
IX.	Recommendations	58

	<u>Page</u>
Appendices	60
A. Calibration Procedure	60
1. Turbulence Pressure Transducer	61
2. Wave Analyzer	71
3. Amplifier and Preamplifier	75
B. Wake Structure Profile Plots	80
C. Normalized Energy Density Spectra	106
D. Helmholtz Resonance Effects	122
E. Representative Samples of Data	126
F. References	129

LIST OF FIGURES

	<u>Page</u>
Ia. Water Tunnel Test Section	18
Ib. Water Tunnel Test Section	18
Ic. Water Tunnel and Flow Circuit	19
IIa. Water Tunnel Test Section Detail	22
IIb. Water Tunnel Test Section Detail	22
IIc. Traversing System	23
III. Details of Turbulence Probe and Pressure Tubes . . .	28
IVa. Electronics Equipment Components	30
IVb. Electronics Equipment Components	30
V. Electronics Equipment Component Block Diagram	31
VIa. Turbulence Signal Presentation at $y/t = 0.5$	33
VIb. Turbulence Signal Presentation at $y/t = 0$	33
VIc. Turbulence Signal Presentation with Air Bubble in Probe Tip	33
VII. Relative Transverse Vortex Spacing	46
VIII. Comparison of Wave Analyzer Energy Density Spectra .	49
IX. Decay of Vortex Energy Downstream	55
 A-1 Gage Calibration Schematic	 62
A-2 Transducer-Preamplifier Calibration Photograph . . .	63
A-3 Transducer-Preamplifier Calibration Response	70
A-4 Component and System Gain Response	77
A-5 Electrometer Preamplifier Circuit Diagram	79
 B Wake Structure Profile Plots	 80
 C Normalized Energy Density Spectra Plots	 106
 D-1 Sketch of Spindle Cavity	 124

LIST OF TABLES

	<u>Page</u>
I. Dimensions and Geometries of Test Plates	4
II. Profile Drag Coefficients	44
III. Strouhal Numbers and Relative Transverse Vortex Spacing	46
IV. Comparison of Actual and Predicted Shedding Frequencies	47

LIST OF SYMBOLS

- A_p = discrete area under vortex shedding frequency peak in turbulence energy density spectrum, dimensionless.
 A_S = area under entire energy spectrum between frequency limits of vibration analyzer, dimensionless.
 a = longitudinal vortex spacing, inches.
 b = transverse vortex spacing, inches.
 c = chord of test plate, inches.
 C_1 = constant of integration or proportionality, $i = 1, 2, 3, \dots$
 C_D = drag coefficient.
 C_{Dp} = profile drag coefficient.
 C_{Dw} = wetted surface drag coefficient.
 $C_p = \frac{1}{T_p}$
 $C_v = \frac{1}{T_v}$; also vibration analyzer calibration constant, $\frac{\text{volts}^{-1}}{\text{cps}}$
 d = diameter.
 D_p = profile drag, pounds.
 e = 2.7182...
 e_1 = calibration signal rms voltage, volts.
 $E(n)$ = spectral distribution of turbulence kinetic energy density per unit mass, ft^2/sec^2 per cps.
 E_{bw} = total energy of an input signal within the band width of the vibration analyzer.
 g = acceleration due to gravity, 32.174...
 G_a = amplifier gain.
 G_p = preamplifier gain.
 h = distance between rigid boundaries enclosing a vortex street; tunnel test section width, inches.
 H_{tg} = effective instantaneous total head seen by turbulence

gage, feet of water.

\overline{H}_{tg} = average effective total head seen by turbulence gage.

H'_{tg} = turbulent fluctuation of effective total head seen by turbulence gage.

k = vortex strength, ft^2/sec .

K_{tg} = turbulence gage sensitivity, mv/psi or mv/ft of water.

K_{tp} = transducer-preamplifier system sensitivity = $G_p K_{tg}$.

n = frequency, cps.

Δn = band width, cps.

n_c = vibration analyzer band width center, or tuned, frequency.

n_H = Helmholtz resonant frequency.

n_o = natural or resonant frequency.

n_v = vortex shedding frequency, cps.

p = instantaneous pressure intensity, psi.

\overline{p} = average pressure intensity, psi.

p' = turbulent fluctuation of pressure intensity.

p_o = free stream pressure intensity.

R_d = vibration analyzer meter reading.

Re = Reynolds number.

Re_c = chord length Reynolds number = U_c/ν .

Re_d = diameter Reynolds number = U_d/ν .

S = Strouhal number.

S_b = Strouhal number based on transverse vortex separation = nb/U_o .

S_d = diameter Strouhal number for a cylinder = nd/U_o .

S_t = plate thickness Strouhal number = nt/U_o .

t = plate thickness in inches; also time in seconds.

T_p = pressure decay time constant, seconds.

T_v = voltage decay time constant, seconds.

- u = instantaneous local velocity in the downstream or x-direction.
- \bar{u} = average local velocity in the x-direction.
- u' = turbulent fluctuation of velocity in the x-direction.
- u_v = vortex translation velocity relative to free stream velocity in the x-direction.
- u_1 = velocity in the x-direction immediately outside the plate boundary layer near the separation point.
- \bar{U} = faired value of \bar{u} measured at $y/t = 1.5$.
- U_0, U = free stream velocity in the x-direction.
- $\sqrt{u'^2}$ = measure of turbulence intensity in the x-direction, rms deviation about the average velocity \bar{u} .
- v' = turbulent velocity fluctuation in the y-direction (transverse, horizontal, and normal to the test plate).
- w' = turbulent velocity fluctuation in the z-direction (span-wise and vertical).
- x = downstream coordinate, measured from trailing edge of test plate and positive in direction of mean flow.
- y = transverse coordinate, normal to the test plate, horizontal, and positive to the right when facing upstream.
- α = angle of incidence; $\alpha \approx 0$ with respect to mean flow for this investigation.
- β = trailing edge reentrant angle; also measure of annihilation of boundary layer vorticity at separation point.
- γ_m = specific weight of mercury, lb/ft³.
- γ_w = specific weight of water, lb/ft³.
- δ = boundary layer thickness.
- ζ = vorticity, fps/ft.
- ν = kinematic viscosity, ft²/sec.

π = 3.14159...

ρ = mass density, slugs/ft³.

Δ = an increment.

I. INTRODUCTION

A. General Statement of the Problem.

One of the most vital problems in ship design today, and particularly in warship design, is the reduction of noise and vibration. Of the many and varied sources of noise and vibration in ship structures, one of the more significant is the hydroelastic vibration of propeller blades and control surfaces. The phenomenon of "singing" propellers has interested workers in several fields since the 1930's, when higher propeller speeds and the use of airfoil blade sections instead of ogival sections became prevalent^[1]. Fundamentally, blade vibration of some sort has been held responsible in the literature for this phenomenon, but writers have differed in their analyses of the vibration and in their several explanations for the cause of this vibration^[1-8].

While propeller in-flow variations, blade back pressure variations, and wheel unbalance may indeed contribute to the phenomenon, most writers, however, agree that the probable cause of singing appears to be the formation and shedding of vortices in resonance with the natural frequency of the blade and its entrained water. If the vibrations set up by the process of forming of eddies at the trailing edge of a propeller blade are in the audible range of frequency, a singing note may be emitted^[9]. It has been found that for a given propeller system singing occurs in a relatively narrow frequency band and over a relatively narrow range of propeller rpm.

While audible singing is generally not encountered in

larger foil or plate structures such as rudders, hydrofoils, submarine diving planes and other control surfaces, vibration and flutter are significant problems^[10,11]. It appears reasonable to consider that vortex induced vibration may be at least in part responsible for this.

It has been found in practice that modifications to the geometry of propeller blade sections will alter the characteristics of singing or eliminate it entirely. Den Hartog^[12] and others discuss the procedure of sharpening the leading edge of propeller blades and turbine blade runners to eliminate undesirable singing. Propeller sections with sharp leading edges have, however, been known to sing violently, and several authors^[1,4,9] discuss the practice of blunting the trailing edges of blades to alleviate this condition. The periodic transverse forces due to alternate shedding of vortices incite a resonant mode of vibration in some part of the propeller blade, and according to Saunders^[9] the remedy is to change the shape of the trailing edge in some manner so that the vortex formation is eliminated or that the vortices and circulation are stabilized. One simple method is to cut off the trailing edge square, so that the separation points are "well defined and fixed in position;" another is to plane the trailing edge flat at some angle to the base chord. Various other trailing edge geometry modifications are discussed in the literature.

Since practical experience shows that modification of the trailing edge will alter the response of a blade section, and since it is not reasonable that such modifications would

materially alter the mass or the internal damping of the system^[7], it follows that it is the forcing function, i.e., the shedding of vortices, which has in some way been modified.




A large body of literature exists on the subject of wake flows behind various types of bodies. The majority of it, however, deals with the wakes behind bodies of revolution and bluff bodies, and almost all of it treats the so-called fully developed wake well downstream of the body. In order to conduct a study of trailing edge vortex phenomena at their origin, it becomes necessary to investigate the "early wake" or the region within about ten characteristic dimensions downstream of a foil or flat plate. Such a study should properly consider the distribution of the energy present in the early wake and the variations of velocity, pressure, and turbulence intensity in this region. Furthermore, the plate boundary layer itself and the free shear layer where vorticity becomes pronounced may be expected to influence these phenomena. These considerations have prompted an investigation by the authors of the early wake behind three flat plates of varying trailing edge configuration at the variable flow water tunnel of the Massachusetts Institute of Technology Hydrodynamics Laboratory.

B. Scope of the Investigation.

As part of a general investigation of wake mechanics conducted at the Massachusetts Institute of Technology Hydrodynamics Laboratory and sponsored by the David Taylor Model Basin, Huval^[13] recently conducted an investigation of the early wake behind a fixed flat plate having a semi-cylindrical

leading edge, a chord-to-thickness ratio of 8.0 and a 60° included angle trailing edge. This particular plate was one of a series studied by Ippen, Toebes, and Eagleson^[14] for the purpose of investigating hydroelastic behavior of flat plates with various trailing edge configurations. The authors chose three other plates from this systematic series for their investigation; their dimensions and geometries are listed below in Table I:

TABLE I
DIMENSIONS AND GEOMETRIES OF TEST PLATES

<u>PLATE</u>	<u>LEADING EDGE</u>	<u>THICKNESS</u>	<u>CHORD</u>	<u>TRAILING EDGE</u>
A	semi-cylindrical	1/4"	2"	 $\beta = 90^\circ$
B	semi-cylindrical	1/4"	2"	
C	semi-cylindrical	1/4"	2"	

These three plates correspond respectively to Plates 12, 11, and 15 of Reference [14].

The experimental program for this investigation provided for the measurement of velocity and pressure distributions and distribution of turbulence intensity across the wake at several longitudinal positions in the early wake of the test plates, and for measurement of the turbulence energy spectra at several longitudinal positions on the wake centerline and in the vicinity of the paths of shed vortices.

Plates A and B were originally selected from consideration of vibrational amplitude responses as a function of restraint (Figure 29 of 14); these particular plates represented respectively the lowest and one of the highest

response curves presented. During the course of the investigation, it became desirable to include an intermediate configuration, and Plate C was incorporated into the investigation. As in Huval's investigation, the authors decided to clamp the plate rigidly in the water tunnel test section in order to be able to study the wake energy with minimum contribution from plate vibrations. In order to facilitate future comparison with Huval's results, it was decided to conduct measurements at a free stream velocity, U_0 , in the neighborhood of 10 feet per second.

II. REVIEW OF PREVIOUS WORK

A. Vortex Excited Blade Vibration

Of the large number of explanations postulated for singing propeller blades over the past 30 years, the suggestion that vortex formation and shedding might be the responsible mechanism appears to be one of the most plausible. Experimental work conducted in the United States and in the Soviet Union in recent years^[8,15] support strongly the contention that singing occurs when the vortex shedding frequency is in resonance with one of the natural modes of vibration of a given structure.

Considering that at resonance singing frequency coincides with vortex shedding frequency, Gongwer^[8] presented an empirical modification of the Strouhal formulation, suggesting that the characteristic trailing edge dimension should include a portion of the boundary layer thickness. Introducing this factor, he obtained experimentally from his work with vanes

$$S_b = \frac{nb'}{U_1} \approx 0.185 \quad (1)$$

$$\text{where } b' = t + \frac{0.0297x}{\left(\frac{Ux}{v}\right)^{0.2}} \quad (2)$$

and where U_1 is the component of the free stream velocity normal to the trailing edge of the body. Krivtsov also illustrates^[15] the essentially constant behavior of Strouhal number for a given trailing edge thickness.

Several writers have been concerned with the fact that the singing behavior of identical propellers may be quite

different. However, when one considers the processes involved in propeller manufacture and balancing, it is not at all surprising that two propellers of the same class might have slightly different natural frequencies, and that the frequencies of the individual blades might vary somewhat. Lankester^[7] points out that slight differences in natural frequencies between blades are not at all uncommon. This may increase the response or decrease the equivalent damping of one propeller with respect to another having blades of identical natural frequency. If propeller singing is due to self-excited vibration, a small difference in response could make all the difference between singing and non-singing.

Propeller singing has been shown to be dependent upon water temperature^[1] and ambient pressure, indicating further the flow dependence of the phenomenon.

B. Vortex Formation and Wake Periodicity

Since Strouhal's work in the latter part of the 19th century, a large number of investigators have studied the vortex shedding of cylindrical and spherical bodies, and more recently of bluff bodies. While this work is of considerable interest in theory and in practice, and valuable as background, it is not immediately applicable to the case of thin flat plates and other blade sections, and will be treated only cursorily.

The Reynolds number dependence of the Strouhal number, suggested by Raleigh^[16] has been clearly demonstrated recently for circular cylinders by Kovasznay^[17] and by Roshko^[18]. Roshko presents empirical expressions for S_d

for two Reynolds number regimes of flow:

$$S_d = 0.212 (1 - 21.2/Re_d) \quad 40 < Re_d < 150 \quad (3)$$

and

$$S_d = 0.212 (1 - 12.7/Re_d) \quad 300 < Re_d < 5000 \quad (4)$$

For wakes behind various bluff bodies, Ippen et al. review the work of several investigators^[14] and indicate that the general range of Strouhal numbers based upon the largest characteristic dimension normal to the direction of the flow is from about 0.12 to 0.21, i.e., below the value of 0.2 applicable to circular cylinders.

Fage and Johansen in experiments on the early wake behind inclined flat plates showed that Strouhal number is dependent upon angle of incidence, α , increasing as α becomes small^[19]. Expressing S in terms of the separation between free shear layers, S was found to be approximately constant and ≈ 0.16 . Both in Gongwer's experiments and in other experiments on oval struts^[7] it was found that the effect of small angles of incidence was to alter the amplitude of vibration without materially affecting the frequency.

In none of the theoretical treatments of the problem is an explanation of the actual mechanism of vortex formation presented. The work of Betchov^[20] suggests that a possible approach may lie in the treatment of boundary layer oscillations.

Von Karman's classical treatment of periodic wakes has crystallized and stimulated significant work in this field. His stability criterion for a vortex array in a wake has theoretical and practical significance and will subsequently

be utilized to predict shedding frequencies and to analyze free shear layer separation. This concept and Birkhoff's modification will be discussed further under "Theoretical Considerations." Von Karman's treatment makes no attempt to describe the mechanism of vortex formation and is in fact independent of the mechanism and of the geometry of the structure behind which it applies.

C. Wake Structure

The similarity principles of von Karman applied to the Reynolds equations of motion have proven useful in treating axially symmetric or two-dimensional turbulent wakes. Unfortunately, similarity hypotheses apply to a state of statistical equilibrium of flow processes relatively far downstream in a wake, and cannot be considered applicable to the early wake.

Roshko's experiments^[18] and those of Cooper and Lutzky^[21] present results of velocity and turbulence distributions in the relatively early wake behind cylinders and bluff bodies respectively.

Birkhoff^[22] and others point out that contrary to the predictions of the Kirchhoff wake model, actual large wake underpressures exist.

D. Trailing Edge Geometry

Ippen et al. point out the effect of trailing edge geometry on drag coefficients for various shapes. Schlichting^[23] shows that the drag coefficient can be related to the vortex street through momentum analysis, but notes that this procedure is applicable only relatively far downstream

where the static pressure at the measuring station is equal to the free stream pressure. The correction methods of Betz and of Jones^[24] may be employed in the early wake region, and have yielded valid results behind airfoil sections as close to the trailing edge as 0.05 chord lengths.

E. Turbulence

The complex nature of wake turbulence and turbulent (or even periodic) wake energy precludes any detailed discussion here. Reference [28] in particular and portions of references [29] through [31] are of interest for this investigation as are the results of Huval's experiments^[13].

Ambient turbulence background measurements were made for the water tunnel test section by Perkins^[32] and by Huval^[13] indicating relative mean turbulence levels of about 0.03 and 0.065 respectively. Assuming isotropic turbulence with a general power decay law, and ergodic process, Huval's measurements indicated that the free stream turbulence was largely in its initial stage. The character of the free stream turbulence spectrum obtained by Huval indicates anisotropy in the low frequency end; the high frequency range, however, indicates isotropic statistical equilibrium. Huval notes that the high frequency spectrum appears to follow von Karman's suggested energy variation with $n^{-5/3}$ [13]. This is in agreement with the Kolmogoroff spectrum law cited by Hinze^[28].

Hinze points out that in all cases where the mean velocity shows a gradient turbulence will be anisotropic. It should then be expected that in regions of a wake where such

gradients exist anisotropic turbulence will obtain. This condition is expected to exist in the early wake behind an object.

Roshko^[18] notes that the velocity fluctuation in the wake of a vortex-shedding cylinder displays a predominant frequency which is the shedding frequency; he points out further that this predominant frequency will have random irregularities imposed upon it.

Distributions of turbulence intensity, mean velocity, and pressure in a turbulent wake are discussed by Hinze. Theoretical treatments of these distributions are in general predicated upon similarity assumptions which are well known. Such assumptions, however, are not expected to be justified in the early wake behind a structure. Cooper and Lutzky^[21] found that certain predictions made on the basis of similarity hypotheses were not upheld by experimental evidence in a region relatively close behind bluff bodies. They note that this discrepancy was not resolved.

III. THEORETICAL CONSIDERATIONS

A. Analysis of the Vortex Street.

From consideration of complex potential theory, it can be shown^[25] that the complex potential function due to an infinite row of equally spaced vortices is given by

$$w = \frac{ik}{2\pi} \ln \sin \frac{\pi z}{a} \quad (5)$$

from which it can further be shown that for two such rows parallel to each other and separated by a distance b ,

$$w = \frac{ik}{2\pi} \left[\ln \sin \frac{\pi}{a} \left(z - \frac{b}{2} \right) - \ln \sin \frac{\pi}{a} \left(z - \frac{a}{2} + \frac{ib}{2} \right) \right] \quad (6)$$

where:

a = longitudinal vortex spacing
 b = transverse vortex spacing
 k = vortex strength

Since $u - iv = \frac{dw}{dz}$, differentiation and separation of components yields an expression for vortex velocity in the longitudinal direction:

$$u_v = \frac{k}{2a} \tanh \frac{\pi b}{a} \quad (7)$$

From stability considerations, von Karman showed^[25,26] that the street can be stable only when vortices in one row are opposite the interval center between vortices in the other row, and then only when the ratio $b/a = 0.281$.

Rosenhead (cited in 25) shows that rigid boundaries equidistant from the mean centerline of the vortex street may affect the stability ratio. If h = the distance between the rigid boundaries, then as the ratio a/h varies from 0 to 0.815, the stability ratio has a unique but continuously changing value, going from 0.281 to 0.256. For values of $a/h >$

0.815 stability exists for a certain range of values of b/a , and for values of $a/h > 1.419$, the configuration is stable for all values of b/a . Birkhoff (cited in 14) predicts a stability ratio of $b/a = 0.35$ from inertia considerations.

The test section of the water tunnel used in this present investigation is rectangular, measuring 9 inches high by 7-1/2 inches wide. The test plate is mounted vertically in the section. The dimension h between rigid boundaries in this case is then 7-1/2". Assuming that at the trailing edge b = plate thickness, t , and proceeding from the von Karman criterion $a/b = 0.281$ as a starting point, the ratio $a/h = 0.1185$. Following a reiterative procedure and assuming linear decrease of stability ratio with increase in a/h , the Rosenhead treatment indicates that the stability ratio for vortex streets in the current investigation would be $b/a = 0.271$. In actuality the transverse spacing is expected to be greater than the plate thickness due to wake spreading. The assumption of linear decrease in b/a is considered adequate in the region of a/h concerned. It appears, then, that a stability ratio for b/a may lie in the region from about 0.27 to about 0.28 for this investigation.

After the manner of Ippen^[14] and Birkhoff^[27] it can be shown that considerations of vorticity diffusion from the boundary layer can lead to an expression for the strength, k , of the vortices in the wake. If K_1 be the rate of shedding vorticity from each side of an obstacle, then as an approximation:

$$K_1 = \int \zeta u_1 dy = \int \frac{\partial u}{\partial y} u_1 dy = \frac{1}{2} u_1^2 \quad (8)$$

where u_1 is the velocity outside the boundary layer near the separation point. If $\beta = K/K_1$, where K is von Karman's rate of vorticity discharge from each side of an obstacle, then β is a measure of the annihilation of vorticity at the trailing edge. Both Prandtl and Roshko (cited in 14 and 27) have found experimentally that $\beta = 0.5$ for periodic wakes. Applying this value and assuming that $u_1 = U$, we obtain:

$$K = 0.25 U^2 \quad (9)$$

Introducing this into von Karman's expression for vortex strength, we obtain:

$$k = \frac{Ka}{U - u_v} = \frac{0.25 aU}{1 - u_v/U} \quad (10)$$

Introducing this into Eq. (7) we obtain:

$$\frac{u_v}{U} (1 - \frac{u_v}{U}) = 0.125 \tanh \pi b/a \quad (11)$$

from which:

$$\frac{u_v}{U} = 0.5(1 - \sqrt{1 - 0.5 \tanh \pi b/a}) \quad (12)$$

Taking as the stability ratio $b/a = 0.271$ and operating on Eqs. (10) and (11) we obtain:

$$u_v/U = 0.0955 \quad (13)$$

$$k = 0.277 aU$$

From von Karman's relationship between profile drag, D_p , and wake vorticity, where $D_p = k \rho \frac{b}{a} (U - 2u_v) + \frac{\rho k^2}{2\pi a}$, and from Eqs. (13) we obtain:

$$D_p = 0.0728 \rho a U^2 \quad (14)$$

from which:

$$C_{Dp} = \frac{D_p}{\frac{1}{2} \rho t U^2} = 0.1456 a/t \quad (15)$$

and reintroducing the stability ratio $b/a = 0.271$:

$$C_{Dp} = 0.537 \, b/t \quad (16)$$

It should be pointed out that Ippen et al. assumed a value of $K/U^2 \approx 0.4$ which is in consonance with empirical results cited by Birkhoff^[27]. If, however, the experimental result of $\beta = 0.5$ is accepted and Eq. (8) is considered valid, this would lead to a value of $u_1/U = 1.265$.

Birkhoff^[27] points out that it is a corollary consequence of the theorem of conservation of momentum that in viscous wakes vortex transverse spacing tends to increase; this is experimentally observed. For slightly viscous fluids it is further noted that transverse vortex spacing is essentially equal to the wake thickness a little behind the obstacle. Birkhoff notes that for circular cylinders the critical diameter Reynolds number above which the wake first becomes periodic is lowered by external turbulence. For flat plates parallel to the flow the critical wake-thickness Reynolds number is about $3.44\sqrt{Re_1}$ where $Re_1 = \frac{U_1}{\nu}$; this is the same order of magnitude as in the case of a circular cylinder.

Following Ippen's procedure, the plate thickness Strouhal number for vortex shedding can be estimated from Eqs. (13) and (15):

$$S_t = \frac{nt}{U} = \left(1 - \frac{u_v}{U}\right)(t/a) = \frac{0.1312}{C_{Dp}}$$

Introducing Eq. (16) we obtain:

$$S_t = 0.245 \frac{t}{b} \quad (17)$$

from which:

$$n_v = \frac{StU}{t} = \frac{0.245 U}{b} \quad (18)$$

If wake thickness and transverse vortex separation are taken as being approximately equal to plate thickness in the early wake, then for $t = 0.25"$ we obtain a predicted vortex shedding frequency of:

$$n_v = 11.76 U \text{ (cps)} \quad (19)$$

It should be pointed out that none of the foregoing takes into consideration trailing edge geometry. Furthermore, these developments do not consider any Reynolds number dependence upon either Strouhal number formulation or periodic wake structure.

IV. DESCRIPTION OF EQUIPMENT AND INSTRUMENTATION

A. The Variable Flow Water Tunnel.

A detailed description of the variable flow water tunnel is given in Reference [33]. Photographs of the tunnel test section are presented as Figs. Ia. and Ib.; Fig. Ic. is a schematic diagram of the tunnel and its associated flow circuit. The hydraulic characteristics of the water tunnel are presented in Appendix A of Reference [14]. Tunnel operation is possible with any one or a combination of three centrifugal pumps.

Considerations of minimum mean level of background turbulence and consistency of pump operation led the authors to conduct all measurements with Pump III providing the flow. Referring to Fig. Ic., the flow was routed from Pump III to the right through the 18" distribution circuit, back to the left past Pump I (which was isolated from the circuit), and up through the water tunnel inlet riser. It had initially been planned to operate with both Pumps II and III in operation simultaneously, with the stop valve between them shut, but flow reversal through Pump II and problems in velocity control led to the decision to isolate Pump II from the circuit.

From the expanding tunnel inlet riser the flow passes through four No. 16 mesh screens and a 33" long contraction into the test section. The plexiglass test section is 36" long and rectangular in section, measuring 9" high and 7-1/2" wide. From the test section, the flow returns to the



FIGURE 1a. Variable Flow Water Tunnel Test Section, Showing Location of Amplifier and Preamplifier.

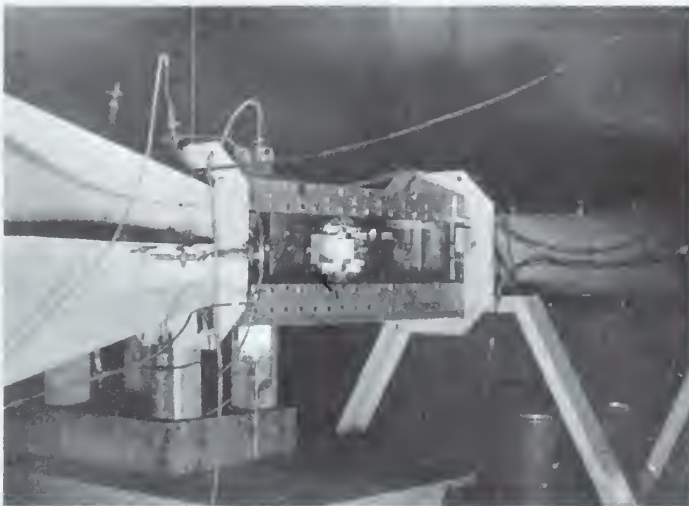
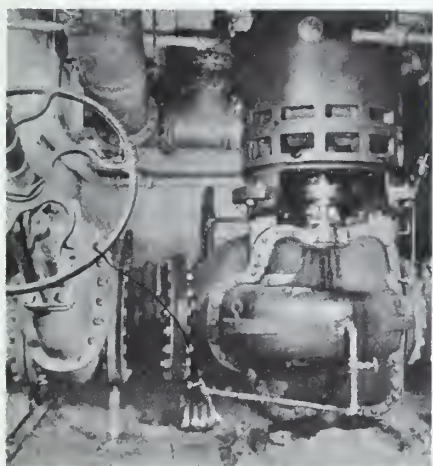
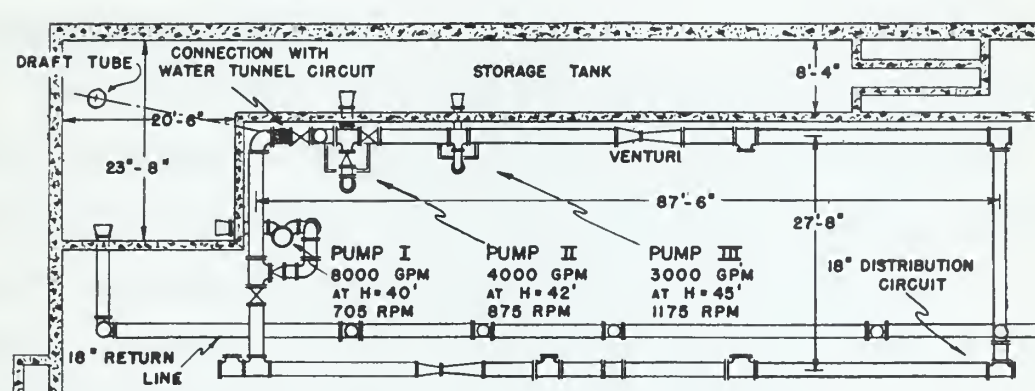
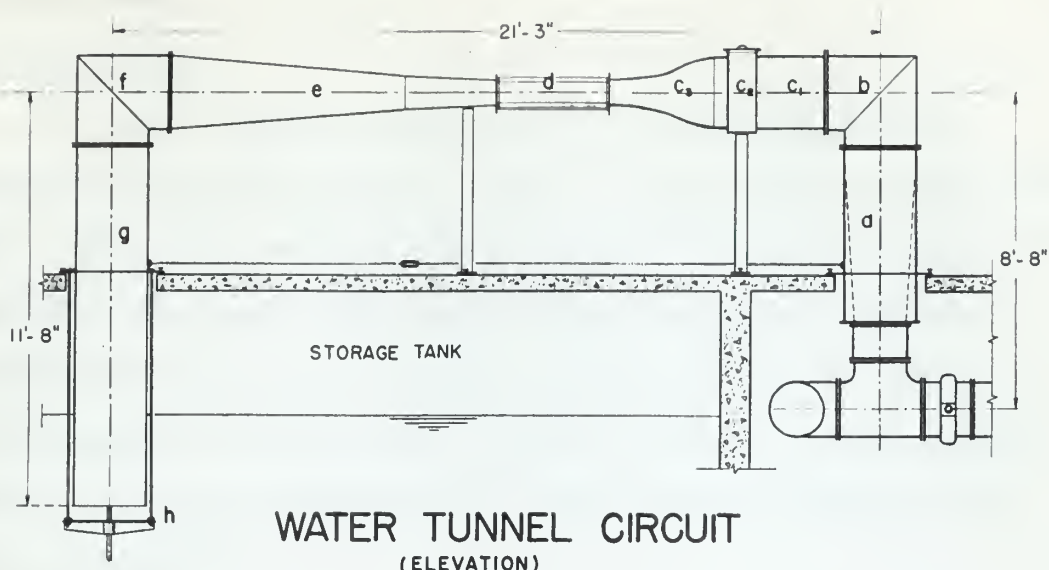
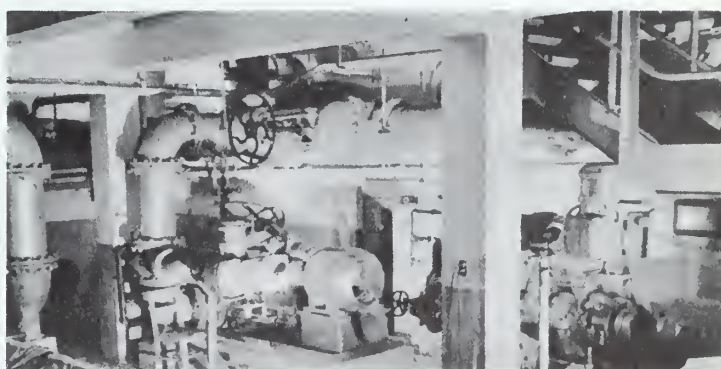


FIGURE 1b. Variable Flow Water Tunnel Test Section, Left Side.



Pump I



Pump II and III

FIGURE 1c. Water Tunnel and Flow Circuit.
(From Huval, "The Early Wake of a Fixed Flat Plate.")

storage tank.

B. Test Plates.

The test plates studied in this investigation are described briefly in Table I and in more detail in Reference [14]. They were manufactured from 1/4" aluminum stock and carefully machined. The plates spanned the 9" vertical dimension of the test section, and presented a 2" chord in the direction of the flow. The test plates were anodized to prevent corrosion and pitting; this process proved to be quite successful.

C. Test Plate Mounting.

The test plates were mounted using the spindles illustrated in Figure 6 of Reference [14]. The spindles were attached to the plates with set screws such that the center-line of the spindles was essentially in line with the center of radius of the semi-cylindrical plate leading edge. The spindles were clamped to prevent rotation.

Each of the spindles passed through a roughly rectangular 1" by 2-1/2" hole in the upper and lower test section walls. These holes opened further into larger cavities. The upper cavity was originally sealed with a solid cover plate; because of the tendency of air bubbles to accumulate in this cavity, a vent was subsequently installed in the cover plate. The lower spindle passed through a gasketed circular hole in the bottom cover plate and was again braced below the test section. This arrangement is due to the earlier investigation reported in Reference [14].

D. Traversing Mechanism.

In order to obtain data on transverse and longitudinal wake structures with the flow measurement devices to be described subsequently, it was necessary to provide for traversing in these directions. The traversing mechanism used by Huval^[13] was employed in this investigation. The instrumentation strut, located just downstream of the test plate, passes through the test section side walls through slotted blocks which permit a longitudinal traverse. These are shown installed in Figs. IIa and IIb. The instrumentation strut itself, illustrated in Fig. IIc, can be traversed in the transverse direction through the side plates and blocks.

Longitudinal positioning of the strut is accomplished by means of scales graduated in $1/64$ inch mounted on the slotted blocks. A transverse scale graduated in 0.002 inch permits transverse positioning.

E. Flow Measurement Devices.

The total and static head tubes and the turbulence pressure transducer employed in the wake surveys are described in detail in References [13] and [32]. These instruments permit measurement of the total and static pressures in the wake behind the test plate, and will be treated separately below. In addition to these devices, a contraction manometer provides for measurement of mean free stream velocity.

1. Turbulence Pressure Transducer.

A cylindrical disc-shaped barium titanate ceramic transducer, 0.125" in diameter and 0.100" thick, is mounted in a tapered water-filled probe tip illustrated in Fig. III.

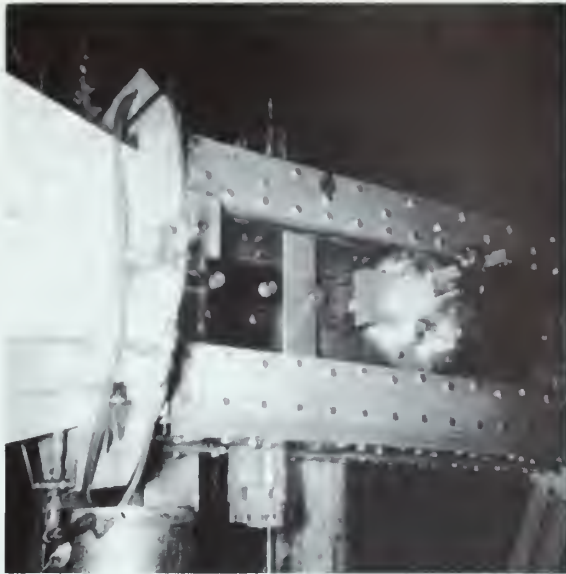


FIGURE IIa. Left Side View of Test Section, Showing Position of Test Plate and Transverse Strut Positioning Scale.

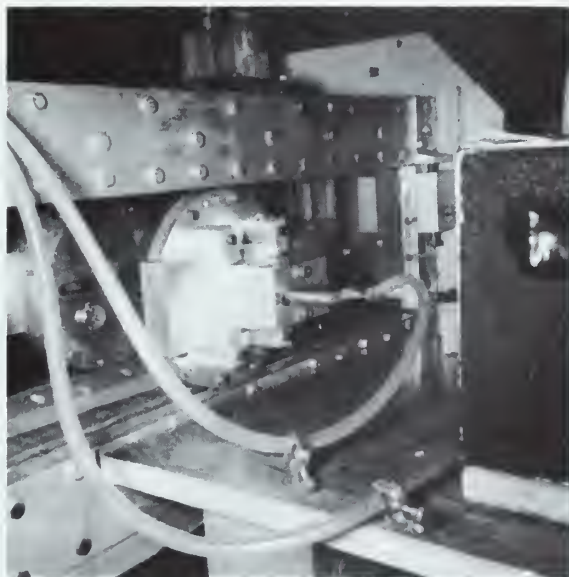


FIGURE IIb. Right Side View of Test Section, Showing Total and Static Head Leads and Transducer Cable to Preamplifier.

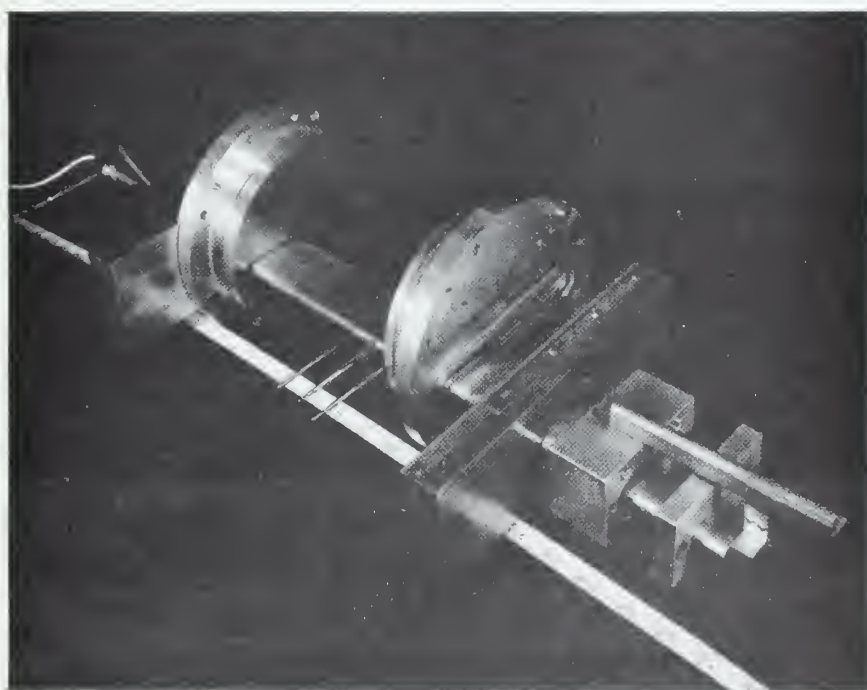
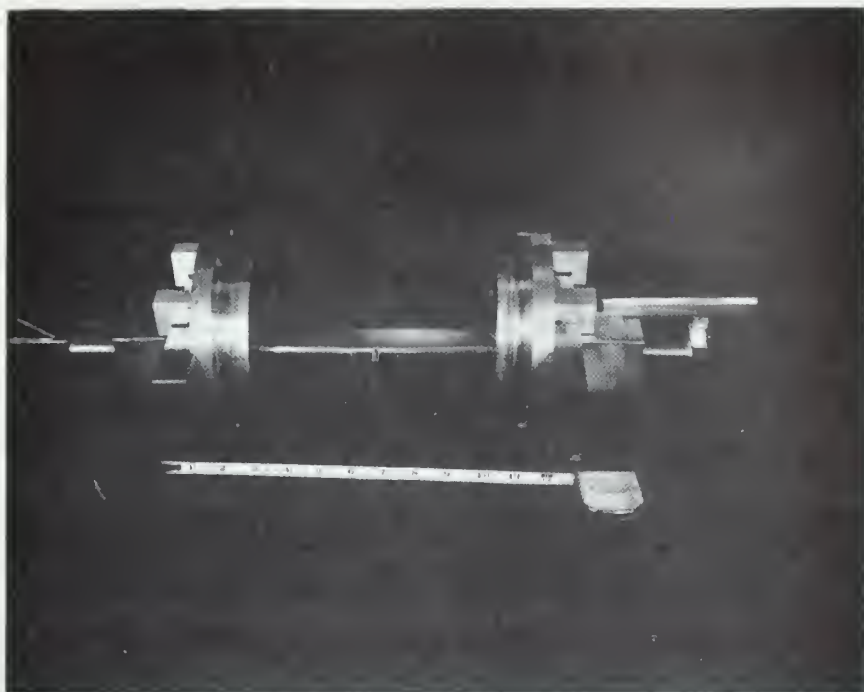


FIGURE IIc. Photographs of Traversing System.
(From Huval, "The Early Wake of a Fixed Flat
Plate.")

The ceramic is located behind a thin silver-plated brass diaphragm. The tapered probe tip ends in a 1/16" diameter with a 0.025" hole drilled in it to permit "point" pressure fluctuation measurements. Pressure variations are transmitted to the ceramic through a water column expanding from 0.025" diameter to approximately 0.221" diameter, and through the diaphragm.

Considerable care must be taken to insure that no air bubbles are present in the water column. Experience has shown that the presence of even minute air bubbles will materially affect the response of the system by altering the response of the water column. To this end, deaerated water is used for filling the probe tip. Reasonable success was experienced by pumping deaerated water through the probe tip for several minutes with a syringe.

It was found earlier that the transducer did not respond to static pressure changes [13]. Recent improvements, however, have improved the response of the transducer and made quasi-static calibration possible. This will be discussed further in Appendix A.

2. Transducer Response.

The instantaneous response of a total head tube aligned parallel to the direction of mean flow, in Huval's notation [13] is given by:

$$\begin{aligned} H_{tg} &= \frac{\bar{p}}{\gamma} + \frac{p'}{\gamma} + \frac{(\bar{u} + u')^2}{2g} \\ &= \frac{\bar{p}}{\gamma} + \frac{p'}{\gamma} + \frac{\bar{u}^2}{2g} + \frac{2\bar{u}u'}{2g} + \frac{u'^2}{2g} \end{aligned} \quad (20)$$

assuming that the terms involving v' and w' do not significantly

contribute to the total instantaneous head measured in the longitudinal direction.

Now let e_{tg} = the instantaneous output signal of the turbulence gage in millivolts, and

K_{tg} = turbulence gage sensitivity in millivolts per foot of water.

Then the turbulence gage output signal becomes:

$$e_{tg} = K_{tg}H_{tg} = K_{tg} \left(\frac{\bar{p}}{\gamma} + \frac{p'}{\gamma} + \frac{\bar{u}^2}{2g} + \frac{\bar{u}u'}{g} + \frac{u'^2}{2g} \right) \quad (21)$$

Now let G_p = preamplifier gain, and

e_p = voltage output of the preamplifier in millivolts,

Then:

$$e_p = G_p K_{tg} \left(\frac{\bar{p}}{\gamma} + \frac{p'}{\gamma} + \frac{\bar{u}^2}{2g} + \frac{\bar{u}u'}{g} + \frac{u'^2}{2g} \right) \quad (22)$$

Furthermore:

$$\begin{aligned} e_p &= \bar{e}_p + e_p' \\ \bar{e}_p &= G_p K_{tg} \left(\frac{\bar{p}}{\gamma} + \frac{\bar{u}^2}{2g} + \frac{\overline{u'^2}}{2g} \right) \end{aligned}$$

Referring to the electronics equipment block diagram (Fig. V) it is noted that a DC filter (i.e., a 1 MFD capacitor) is installed between the preamplifier and the amplifier, since only the fluctuating components of the turbulence gage signal are of interest at the measuring instruments. Therefore, the input signal to the amplifier becomes:

$$\begin{aligned} e_p' &= e_p - \bar{e}_p \\ &= G_p K_{tg} \left(\frac{p'}{\gamma} + \frac{\bar{u}u'}{g} + \frac{u'^2 - \overline{u'^2}}{2g} \right) \end{aligned} \quad (23)$$

Letting e_m = amplified turbulence signal input to the measuring instruments, and

G_a = amplifier gain, then

$$e_m = G_a G_p K_{tg} \left(\frac{p'}{\gamma} + \frac{\bar{u}u'}{g} + \frac{u'^2 - \overline{u'^2}}{2g} \right) \quad (23)$$

Here e_m represents the amplified turbulence gage signal in millivolts at the input to the measuring instruments (rms voltmeters and vibration analyzer).

The true rms voltmeter output (measured by the thermocouple voltmeter) becomes:

$$V_{rms} = \sqrt{e_m^2} = G_a G_p K_{tg} \left[\left(\frac{p'}{\gamma} + \frac{\bar{u}u'}{g} + \frac{u'^2 - \overline{u'^2}}{2g} \right)^2 \right]^{\frac{1}{2}} \quad (24)$$

Expansion of the terms within parentheses in Eq.(24) results in:

$$\begin{aligned} \left(\frac{p'}{\gamma} + \frac{\bar{u}u'}{g} + \frac{u'^2 - \overline{u'^2}}{2g} \right)^2 &= \frac{\bar{u}^2 u'^2}{g^2} + \frac{\bar{u}u'(u'^2 - \overline{u'^2})}{g^2} \\ &\quad + \frac{(u'^2 - \overline{u'^2})^2}{4g^2} + \frac{2\bar{u}u'p'}{\gamma g} \\ &\quad + \frac{(u'^2 - \overline{u'^2})p'}{\gamma g} + \frac{p'^2}{\gamma^2} \end{aligned}$$

The full expression for rms voltmeter output becomes:

$$\begin{aligned} V_{rms} = G_a G_p K_{tg} \left(\frac{\bar{u}^2 \overline{u'^2}}{g^2} + \frac{\bar{u} \overline{u'^3}}{g^2} + \frac{\overline{u'^4}}{2g^2} - \frac{\overline{u'^2 u'^2}}{2g^2} \right. \\ \left. + \frac{2\bar{u} \overline{u'p'}}{\gamma g} - \frac{\overline{u'^2 p'}}{\gamma g} - \frac{\overline{p'^2}}{\gamma^2} \right)^{\frac{1}{2}} \quad (25) \end{aligned}$$

Now if it may reasonably be assumed that $u' \ll \bar{u}$, say for example that $\sqrt{\overline{u'^2}} \leq 0.1 \bar{u}$, and that p'/γ is of the order of $\frac{u'^2}{2g}$, only the first term within the parentheses makes a significant contribution to the rms signal. Hence:

$$V_{rms} \approx G_a G_p K_{tg} \frac{\bar{u}}{g} \sqrt{\overline{u'^2}} \quad (26)$$

3. Total Head and Static Pressure Tubes.

The total head tube employed is in fact a standard Pitot-static tube, but only the dynamic tap is utilized. Because of the longitudinal pressure gradients present in the wake of the test plate and their effect upon measurements, the static taps of the total head tube could not be used, and a separate static head tube was employed. The pressure taps of the static head tube were in line with the tips of the total head tube and the transducer probe. See Fig. III. Huval^[13] gives a detailed description of these instruments. Both pressure tubes are connected to mercury manometers.

4. Contraction Manometer.

Connected to the upstream and downstream ends of the water tunnel contraction are a mercury manometer and a manometer filled with blue-colored Meriam No. D-8325 indicating fluid (specific gravity = 1.75). These manometers and their piezo-meter taps are described in Appendix A of Reference [14]. The contraction manometer was used to duplicate flow conditions in the water tunnel on separate days of operation. Calibration of this manometer was necessary for the particular flow conditions experienced, and is discussed subsequently.

F. Electronics Equipment.

Electronics equipment utilized in the measurements consisted of an electrometer preamplifier, a KinTel Model 111BF amplifier, a General Radio Type 762-B vibration analyzer, a Ballantine vacuum tube voltmeter and a Sensitive Research Instr. Corp. Model A thermocouple voltmeter, and a Dumont Type 333 dual-beam cathode ray oscillograph. A Hewlett-Packard Model 200C audio oscillator was employed in equipment calibration.

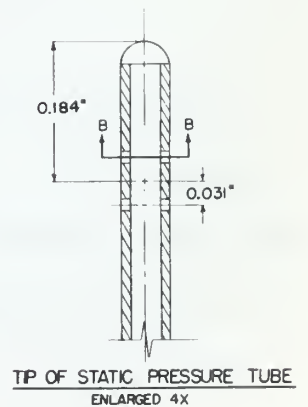
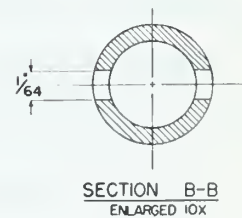
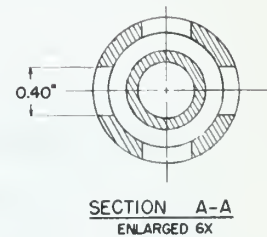
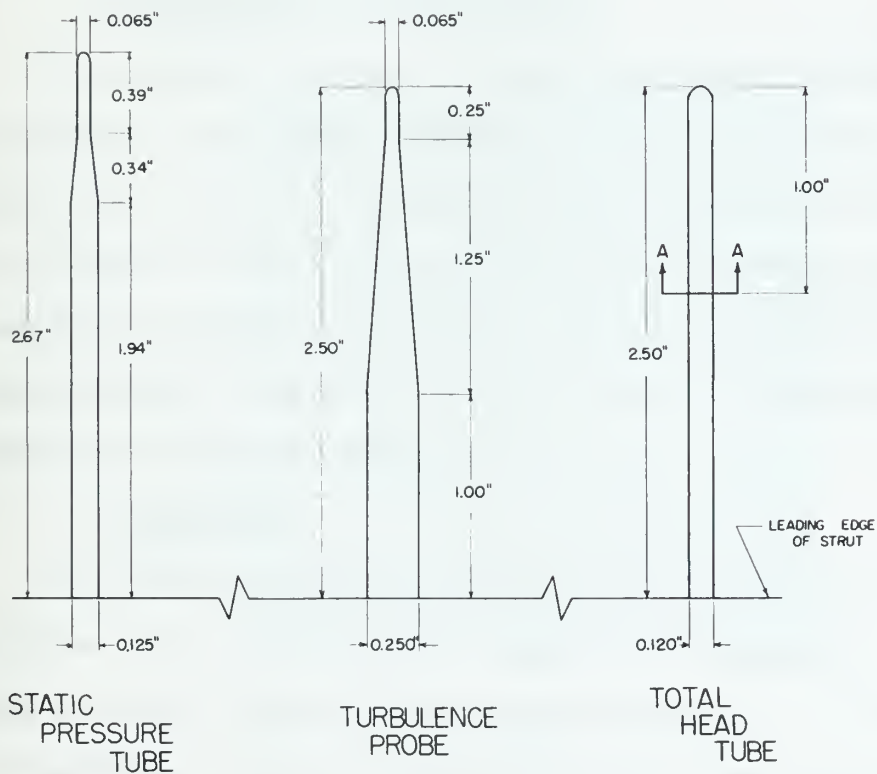
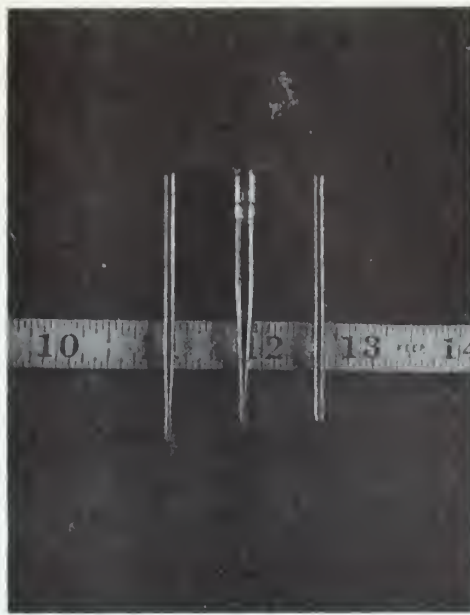


FIGURE III. Details of Turbulence Probe and Pressure Tubes. (From Huval, "The Early Wake of a Fixed Flat Plate.")

These components are illustrated in Figs. IVa and IVb.

(At the end of the investigation a General Radio Model 1445-A vibration analyzer became available; this instrument extended the frequency range of spectrum measurements and was used in one location in the wake of Plate C for comparison purposes.)

It had originally been intended to record the amplified signal from the pressure transducer on magnetic instrumentation tape for remote spectrum analysis on another wave analyzer. Recording difficulties made this impossible during the course of this investigation.

A block diagram of the electronics components is presented as Fig. V.

1. Electrometer Preamplifier.

The primary purpose of the electrometer preamplifier is to provide high input impedance to the first stage of amplification. Huval [13] describes the circuitry of this component, and points out that its addition to the system should permit response to frequencies below 1 cps. The measured gain of this component (see Appendix A) is 0.4 over the majority of the operating frequency range.

2. Amplifier.

The KinTel amplifier used in the system has a very flat response over the operating range of frequencies. The design gain accuracy with a fixed gain setting is $\pm 1\%$ from DC to 2 KCS. The measured response characteristics (see Appendix A) over the operating frequency range point this out further. A DC filter is connected to the input of the amplifier.

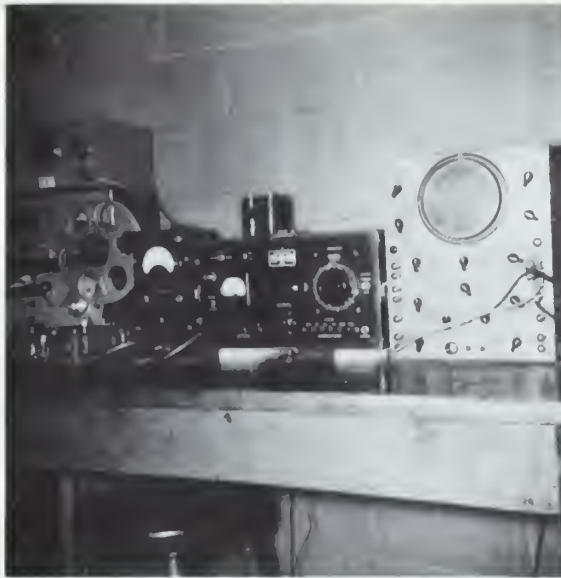


FIGURE IVa. Electronics Equipment: Analysis Components.



FIGURE IVb. Electronics Equipment: Preamplifier and Amplifier Installation.

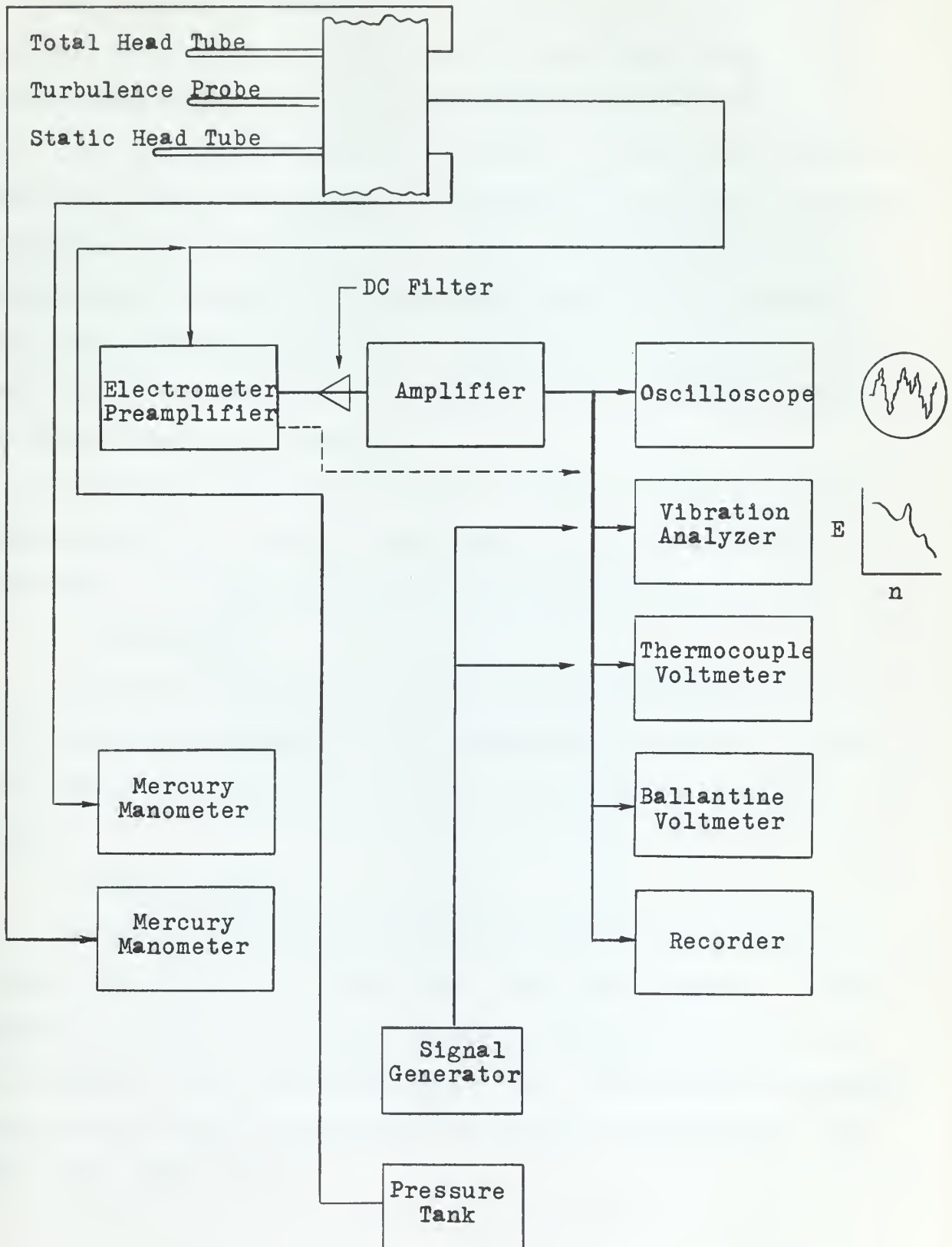


FIGURE V Electronics Equipment Component Block Diagram

3. Wave Analyzer.

The General Radio Type 762-B vibration analyzer is a constant percentage band width tunable voltmeter with a logarithmic scale. Its operating range is from 2.5 to 750 cps. For the sharp selectivity position (in which all measurements were made) the relative attenuation is 3 db at a frequency differing by 1% from tuned frequency. Calibration was performed using a signal from a Hewlett-Packard audio oscillator, and is discussed further in Appendix A. A damping capacitance was inserted in parallel with the analyzer meter to reduce needle fluctuations.

The Model 1554-A analyzer used briefly at the end of the investigation is a similar instrument, but has an extended high limit of 25,000 cps for its operating frequency range.

4. Voltmeters.

The Ballantine VTVM is a true rms-indicating meter only for sinusoidal waveforms. The thermocouple voltmeter, on the other hand, will indicate true rms voltages for any signal input.

5. Oscilloscope.

The Dumont dual-beam oscillograph was used primarily for visual monitoring of the amplified turbulence signal. In this respect it proved very useful in determining the presence of air bubbles in the turbulence probe tip. Such bubbles attenuate severely the higher frequencies of pressure fluctuation. See Figs. VIa, VIb, and VIc.



FIGURE VIa. Turbulence Signal Presentation in Wake of Plate C, $y/t=0.5$, Illustrating Predominant Vortex Frequency.



FIGURE VIb. Turbulence Signal Presentation on Wake Centerline, Illustrating Predominant Double Shedding Frequency.

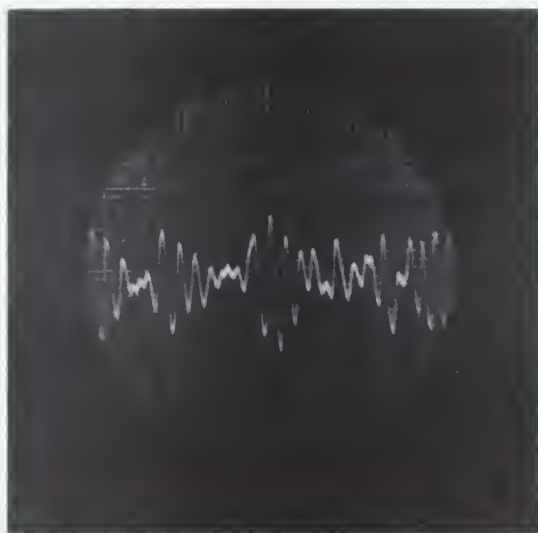


FIGURE VIc. Turbulence Signal Presentation with Air Bubble in Transducer Probe Tip, Same Location as Figure VIb above.

V. CONDUCT OF THE INVESTIGATION

A. Ambient Turbulence.

A study was made of the ambient mean level of turbulence as indicated by the amplified rms voltage from the pressure transducer for various modes of pump operation. As noted earlier, Pump III and the previously described flow circuit were used in the final investigation; this combination yielded one of the lowest mean levels of turbulence.

It had been decided to operate the tunnel at a flow velocity of approximately 10 fps to facilitate correlation with Huval's results^[13]. It subsequently developed after final calibration of the contraction manometer that measurements had been taken at a value of free stream velocity in the test section, U_0 , of about 9.5 fps.

Energy spectrum measurements were made for the empty test section at one longitudinal location on the tunnel centerline.

B. Wake Survey Measurements.

Pressure, mean local velocity, and turbulence intensity distributions across the wake were desired at representative locations in the wakes of the three test plates. A coordinate system was defined as follows: the x-axis was taken as the flow centerline, which was assumed to coincide with the plate and tunnel centerlines. The +x-direction was taken in the downstream direction, measured from an origin located in the transverse plane of the plate trailing edge. The origin of the y-axis was taken at the particular longitudinal station

where measurements were desired ($x/t = 1.50, 3.25, 6.50,$ and 9.75). The $+y$ -direction was taken in the transverse (horizontal) direction toward the right side of the test section (see Fig. 1a.). It was decided to measure total and static head and turbulence rms voltage across the wake in increments of 0.1 plate thickness. Full wake surveys were made from $y/t = -1.5$ to $y/t = +1.5$ in this manner at longitudinal stations $x/t = 3.25$ and 9.75 . Half-wake surveys (from the flow centerline to $y/t = +1.5$) were made at $x/t = 1.50$ and 6.50 .

C. Wake Energy Spectrum Measurements.

Turbulence rms voltage and vibration analyzer measurements were taken at $y/t = 0$ (flow centerline) and $y/t = +0.5$ (in line with the plate edge) at each of the longitudinal measuring stations mentioned above, for each of the three test plates. The empty test section background spectrum mentioned in Section V.A. above was taken at $y/t = 0$ and $x/t = 3.25$.

D. Longitudinal Variation Measurements.

In addition, it was desired to study the longitudinal variation of pressure, velocity, and turbulence intensity along the centerline and at $y/t = +1.5$. To this end the measurements described in Section V.B. were also conducted at these transverse locations at the following longitudinal locations: $x/t = 0.5, 0.75, 1.0, 1.5, 2.0, 2.75, 3.25, 4.0, 5.0, 6.5, 7.5, 8.5,$ and 9.75 .

E. Calibration of Equipment.

Calibration of equipment is discussed in Appendix A.

F. Flow Duplication.

With the foot valve at the discharge end of the water tunnel set and left in one position, it was found possible to adjust the pump discharge valve and the distribution circuit stop valve to duplicate very closely both velocity and pressure conditions within the test section. The Meriam fluid contraction manometer was used for this purpose. This procedure was followed in establishing flow during the measurements made for Plates B and C; minor changes were made in the foot valve setting during the Plate A measurements.

VI. REDUCTION OF DATA

A. Mean Flow Velocity, U_0 .

The contraction manometer was used to measure free stream velocity. The Meriam blue fluid manometer lent itself to more precise reading and was thus used primarily rather than the mercury manometer. The contraction manometer was calibrated against a Prandtl-pitot tube inserted through the upper tunnel wall at the upstream end of the test section. Velocity of the free stream was obtained from the expression:

$$U_0 = 2.06\sqrt{\Delta h_M} \quad (27)$$

where Δh_M = Meriam blue fluid manometer difference reading in inches.

B. Local Mean Velocity, \bar{u} .

Local mean velocity was computed from the total and static head tube manometer readings using the expression:

$$\bar{u} = \sqrt{2g \frac{\gamma_m}{\gamma_w} (\Delta h_t - \Delta h_s) + \Delta z} \quad (28)$$

where: Δh_t = total head manometer difference in feet
 Δh_s = static head manometer difference in feet
 Δz = difference between total and static pressure-side manometer readings, in feet

Because of small variations in values of U_0 for different sets of data, it was decided to normalize \bar{u} with respect to the value of \bar{u} at $y/t = +1.5$ in every case.

C. Turbulence Intensity, $\sqrt{u'^2}$

Following the development set forth in Section IV, the turbulence intensity, $\sqrt{u'^2}$, was calculated from the rms turbulence voltage measurements using the expression:

$$\sqrt{\overline{u'^2}} = \frac{V_{rms}}{\bar{u}} \cdot \frac{g}{GaGpKtg} \quad (29)$$

Turbulence intensity was normalized with respect to the value of \bar{u} obtaining at the point of observation.

D. Static Pressure, \bar{p} .

Static pressure was calculated from the static head tube manometer reading for each measurement location. It was normalized in terms of a pressure coefficient $\frac{\bar{p} - p_0}{\frac{1}{2}\rho U_0^2}$ where p_0 is the free stream pressure and U_0 is the free stream velocity.

E. Normalized Turbulence Energy Density, $E(n)/\overline{u'^2}$.

Normalized turbulence energy distribution density was calculated directly from the thermocouple voltmeter reading and the reading of the vibration analyzer at each observation frequency from the expression:

$$\frac{E(n)}{\overline{u'^2}} = \frac{1}{V_{rms}^2 C_v} \left[\frac{Rd^2(n)}{n} \right] \quad (30)$$

This normalization process eliminates variations in absolute magnitude of energy density due to variations in \bar{u} existing over the entire investigation.

F. Profile Drag Coefficient, C_{Dp} .

The profile drag coefficient was calculated at longitudinal stations $x/t = 3.25$ and $x/t = 9.75$, using the expression:

$$C_{Dp} = \int \left[\frac{2\bar{u}}{\bar{U}_0} \left(1 - \frac{\bar{u}}{\bar{U}_0} \right) - \left(\frac{\bar{p} - p_0}{\frac{1}{2}\rho U_0^2} \right) \right] d\left(\frac{y}{t}\right) \quad (31)$$

where the integration was performed numerically by the trapezoidal rule between the limits $y/t = -1.5$ and $y/t = +1.5$.

Applicability of this expression to the early wake was checked using the Jones Method^[23] where:

$$C_{Dp} = 2 \int \sqrt{\frac{g_2 - p_2}{q_{\infty}}} \left(1 - \sqrt{\frac{g_2 - p_{\infty}}{q_{\infty}}} \right) d \left(\frac{y}{t} \right) \quad (32)$$

where: g_2 = total pressure at the measuring station
 p_2 = static pressure at the measuring station
 p_{∞} = static free stream pressure
 q_{∞} = total pressure minus static pressure in
the free stream.

Integration was performed numerically as above.

It should be noted that the drag coefficient in terms of wetted surface is given by:

$$C_{Dp} = 16 C_{Dws}$$

for a chord-to-thickness ratio of 16 as is the case for these test plates^[13].

VII. RESULTS OF THE INVESTIGATION

A. Wake Structure.

The results of the study of the wake structure of the three test plates are presented graphically as Appendix B to this report. The salient points evidenced by these plots will be discussed in this section.

Figs. B-1 through B-3 are summary plots, showing for each of the three test plates all of the quantities investigated in the wake surveys. Necessarily drawn to a reduced scale, these plots are intended merely to indicate in one location the general pattern of the normalized mean velocity profiles and longitudinal distributions, the transverse and longitudinal distributions of normalized turbulence intensity, and the transverse and longitudinal distributions of normalized static pressure.

Figs. B-4 through B-6 show for each individual plate the development of the dimensionless velocity profile. Values of \bar{u} are normalized in each case with the faired value of \bar{u} obtaining at station $y/t = +1.5$. Profiles are shown for positive values of y/t only. (This is the case for all remaining wake plots with the exception of the wake symmetry plots.) None of the plates show any distinct indication of rapid wake spreading. If the limits of the wake are arbitrarily supposed to be the value of y/t for which $\frac{d(\bar{u}/U)}{d(y/t)} = 0$, it is seen that for Plate A the limits of the wake gradually increase from about $y/t = 1.0$ to $y/t = 1.2$ between the four longitudinal stations. For Plate B the wake spreads from about $y/t = 0.8$ to $y/t = 1.2$; while for Plate C

the wake spreads from about $y/t = 1.0$ to $y/t = 1.4$. The velocity defects for Plates A and C at $x/t = 3.25$ are seen to be markedly greater than for Plate B, and the decay of the velocity defect is more rapid for these two plates. The transverse distributions of velocity defect are essentially Gaussian.

The increased velocity defect at the early stations for Plates A and C is illustrated further in Figs. B-7 through B-10, which present a comparison of the dimensionless velocity profiles at each of the longitudinal measuring stations. Close to the trailing edge both of these plates, which have relatively sharp separation points, have large defects, although at $x/t = 9.75$ all three profiles are essentially the same. Plate A, with its 90° reentrant angle trailing edge, is seen to be intermediate between the other two plates.

Figs. B-11 through B-14 present the transverse distribution of the normalized turbulence intensity for all three plates at each of the longitudinal stations. The wake behind Plate C is seen to be the most turbulent in the centerline area; that of Plate B is the least turbulent. Again Plate A is intermediate. Turbulence intensity decays rapidly downstream and at $x/t = 9.75$ the intensity levels are essentially equal and approaching a constant value across the wake, indicating a decay to isotropic turbulence. Turbulence intensities appear to approach the free stream level by $y/t = 1.5$ at each station for each plate, and the free stream level of turbulence intensity is seen gradually to increase as energy is diffused from the wake into the stream.

Fig. B-15 through B-18 illustrate the transverse distributions of static pressure coefficient in the wake of the three plates at each of the longitudinal stations. Plates A and C with their more sharply defined separation points are seen to have extensive underpressure regions at $x/t = 1.5$; Plate B with its rounded trailing edge does not. As we move downstream the Plate B distribution becomes partially negative, and all three plots move together. At $x/t = 9.75$ (see Fig. B-18) the distribution plot for Plate A is seen to become markedly negative again. This particular presentation is not substantiated by the investigation of longitudinal pressure coefficient distribution illustrated in Figs. B-21 and B-22, and may be due to data error or computation error. However, the possibility that this plot is correct must not be entirely discounted in view of the unusual trailing edge configuration of this plate. The Plate A plot in Fig. B-15 shows sharp excursions which may be not entirely due to scatter. That the sharp drop in pressure coefficient at $y/t = 0.5$ may not be due to data scatter is suggested by the fact that Plate B also indicates a smooth decrease in this region. It will be seen later that Plate A exhibits a very sharp longitudinal pressure coefficient gradient in this region and that reverse flow is also observed.

Fig. B-19 presents longitudinal distributions of normalized mean local velocity at the centerline and at $y/t = 1.5$. In these plots \bar{u} is normalized with respect to free stream velocity, U_0 . Reverse flow was observed for Plate A in the region from $x/t = 0.75$ to about $x/t = 1.25$, and a sharp

longitudinal velocity gradient exists. Reverse flow was also observed for Plate C close to the trailing edge.

Fig. B-20 shows longitudinal distributions of turbulence intensity for the three plates at the wake centerline and at $y/t = 1.5$. Again Plate C indicates the highest level of wake turbulence and Plate B the lowest; Plate A is intermediate.

Figs. B-21 and B-22 illustrate the longitudinal static pressure distributions for the wake centerline and at $y/t = 1.5$ respectively. Fig. B-21 clearly shows the large underpressure in the wake close to the trailing edge of Plate A. Plate C also demonstrates considerable early underpressure, while Plate B underpressure is relatively minor and very rapidly becomes an overpressure for a short period, as does the plot for Plate A. The centerline pressure for Plate C is seen to remain negative throughout the longitudinal range.

Figs. B-23 through B-25 illustrate the essential symmetry of the wakes behind the three plates. Although some data scatter is seen, it appears that the exact centerline of the flow was slightly on the positive side of the established axis, fortuitously insuring that the flow centerline was actually observed during the half-wake surveys as well as in the full-wake surveys.

B. Profile Drag Coefficients.

Profile drag coefficients were calculated for the three test plates at longitudinal stations $x/t = 3.25$ and $x/t = 9.75$. Calculations were initially made using Eq. (31), and then using the Jones method as indicated in Eq. (32). Results of these calculations are listed as follows in Table II.

Profile Drag Coefficients

<u>PLATE</u>	<u>x/t</u>	<u>C_{Dp} [Eq. (31)]</u>	<u>C_{Dp} [Eq. (32)]</u>
A	3.25	0.443	0.141
A	9.75	0.378	0.171
B	3.25	0.519	0.351
B	9.75	0.318	0.195
C	3.25	0.528	0.196
C	9.75	0.393	0.308

The above values of C_{Dp} computed from Eq. (31) are corrected for the longitudinal pressure gradient by algebraically subtracting from the momentum term a pressure coefficient defect term. This term was obtained by numerically integrating the defect of the pressure coefficient plot where the defect was taken as zero at $y/t = +1.5$. The results compare reasonably with the value of $C_{Dp} = 0.537$ predicted by Eq. (16). The results yielded by Eq. (32) are considered incorrect.

C. Vortex Shedding Frequency.

Vortex shedding frequencies were measured by observing the peak responses in the normalized energy density spectra for the three test plates (see Appendix C). These shedding frequencies were observed most strongly at $y/t = 0.5$, in line with the edge of the test plate. The double shedding frequency is more clearly noticeable in the spectra taken at $y/t = 0$, on the centerline. In some cases the triple shedding frequency is also noticeable.

Plate thickness Strouhal numbers were calculated for

each of the three plates, based upon averaged flow velocities and observed shedding frequencies; the results of these calculations are presented in Table III.

In order to compare the results of these calculations, it was decided to normalize the Strouhal numbers with respect to Plate C. It was reasoned that for a small Reynolds number range the Strouhal number might be expected to remain essentially a constant. Since variations in Strouhal number must be due to variations in the transverse separation between vortices, Plate C was selected as a basis for comparison since the square trailing edge provides distinct separation points in comparison with either of the other two test plates. It was then assumed for the sake of comparison that the transverse separation between vortices is indeed equal to plate thickness for Plate C. The Plate C Strouhal number was then taken as being the constant value for all three plates, neglecting small variations due to slightly different plate thickness Reynolds numbers, and this Strouhal number was considered a vortex-separation Strouhal number, $S_b = nb/U$. From this, the relative values of vortex separation were calculated for Plates A and B. These results are also listed in Table III, and their physical significance is illustrated in Fig. VII.

TABLE III

Strouhal Numbers and Relative Transverse Vortex Spacing

<u>PLATE</u>	$S_t = \frac{nt}{U}$	<u>n</u>	<u>U</u>	$S_b = \frac{nb}{U}$	<u>b</u>
A	0.237	109.87	9.66	0.223	0.236"
B	0.251	114.87	9.53	0.223	0.222"
C	0.223	103.00	9.63	0.223	0.250"

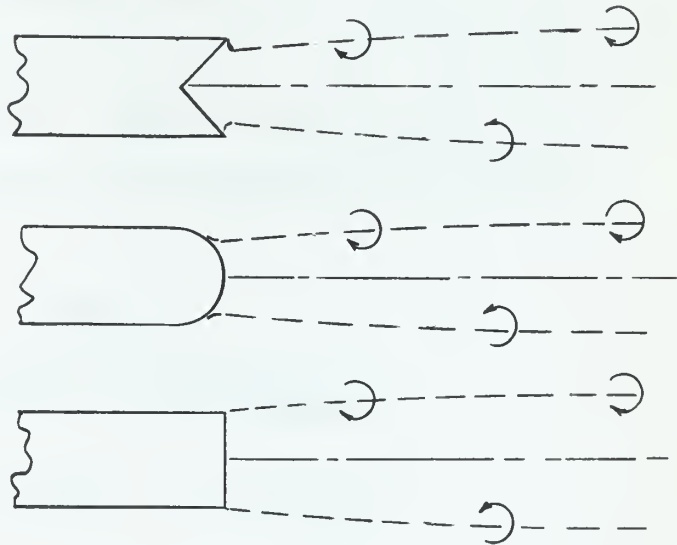


FIGURE VII. Relative Transverse Vortex Spacing

The qualitative representation of vortex spacing in Fig. VII illustrates expected behavior in the wake of Plate B; the separation points move toward the centerline of the plate for a semi-cylindrical trailing edge. When it is realized that vortices do not appear at the separation points as discrete entities, but are gradually formed from vorticity

which diffuses out of the boundary layer, even the behavior of the vortex locus of Plate A appears plausible. A "cavity" of relatively large under-pressure exists immediately behind the reentrant wedge, as was pointed out in Section VII.A. and illustrated in Appendix B, and the flow would be expected to be drawn toward the centerline of the wake. The loci of vortices are illustrated as gradually diverging from the wake centerline in all three cases in conformance with the indication of wake spreading seen in Appendix B.

Observed shedding frequencies were compared with the frequencies predicted from Eq. (19). This comparison is presented below in Table IV. Again, exact agreement is not realized, but a reasonable approximation is indicated.

TABLE IV

Comparison of Actual and
Predicted Shedding Frequencies

PLATE	$n_{v_{\text{actual}}}$	$n_{v_{\text{predicted}}}$
		Eq. (19)
A	110	113.6
B	115	112.0
C	103	113.1

D. Turbulence Energy.

The results of the investigation of the turbulence energy contained at various stations in the early wake behind the three test plates are presented graphically in Appendix C.

Since minor variations existed in the flow conditions obtaining for the individual locations, it was felt that no precise comparison could be made of absolute magnitudes of energy density. To this end, the spectra were normalized as indicated earlier. The data presented on these plots is independent of the local velocity at the point of measurement.

The area under these spectrum curves is dimensionless and is a measure of the total energy present at a particular location in the wake. Integration of the energy density spectrum from zero to infinity should properly result in a value of unity; this is not the case for any of the spectra obtained. This indicates that a certain percentage of the total energy present is either not measured or not accounted for in some manner. Possible explanations for this fact are:

(1) The limits of integration are the finite limits of the wave analyzer. Clearly some energy must be present below 2.5 cps and above 750 cps. Subsequent measurement of one of the spectra with a General Radio Type 1554-A vibration analyzer indicates a considerable amount of energy present at about 1400 cps, which is possibly attributable to Helmholtz resonance effects. (See Appendix D.) It is not believed that any significant amount of energy is present below the low frequency limit of the wave analyzer because of the small frequency increment under consideration.

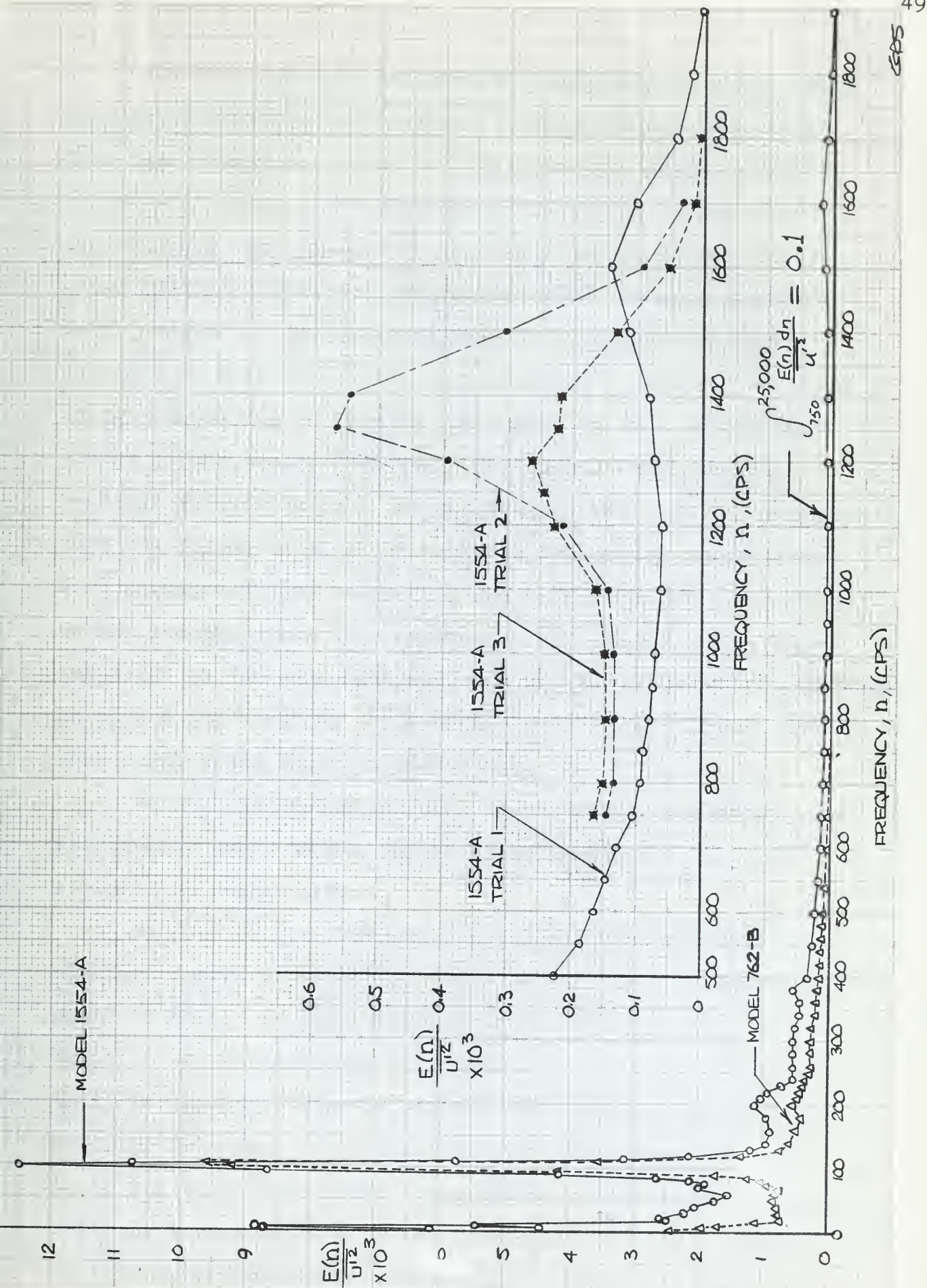


FIGURE VIII Comparison of Wave Analyzer Energy Density Spectra

(2) The spectral measurements made with the wave analyzer are normalized with respect to measurements made with a true rms voltmeter. It is possible that the thermocouple voltmeter, being an all-pass energy measuring device and indicating a true picture of the total energy present at a given location, measures components which the wave analyzer meter does not. The wave analyzer is a tunable voltmeter designed to measure Fourier components of vibration, and some energy components may not be recognized by it. During the course of the energy spectrum measurements, simultaneous readings were taken with the Ballantine VTVM. On the assumption that the foregoing might be correct, the energy spectra were also normalized with respect to the Ballantine voltage, since it was reasoned that this instrument is similar to the meter installed in the wave analyzer. The results of these calculations, which are not plotted, still indicate an energy defect, but a much smaller and more reasonable one.

Further investigation will be necessary to explain this discrepancy fully before any absolute magnitudes can be assigned to energy data.

Because of the foregoing, no magnitude comparison of discrete energy represented by the vortex shedding frequencies could be made. In order to examine the vortex energy as a function of trailing edge configuration then, the ratio A_p/A_s was studied, where A_p is the area under a discrete shedding frequency (or double shedding frequency) peak and A_s is the total area under the spectral plot obtained. This ratio is then a measure of the percentage of energy present in the vortex shedding phenomenon for each of the spectra.

The ratio A_p/A_s is greatest at any given location for Plate B and least for Plate C; Plate A is again intermediate. This fact was noted for both the fundamental and double shedding frequencies. The ratio A_p/A_s shows a linear decay downstream for both Plates B and C. The value for Plate A increases to a maximum in the vicinity of $x/t = 3.25$ and then exhibits essentially a linear decay with x/t .

Two independent investigations of the ambient level of turbulence in the empty test section (with no test plate installed) were conducted. The normalized energy density spectra for these investigations are presented in Fig. C-15. Both spectra were taken at the tunnel location corresponding to $x/t = 3.25$ and $y/t = 0$. For each investigation the value of \bar{u} measured by the total and static head tubes was found to be 9.52 fps. Turbulence intensities for these measurements were 0.0352 and 0.0366, considerably lower than the value of 0.068 found by Huval when operating at $\bar{u} = 10.2$ fps.

Also presented in Fig. C-15 are the theoretical functions suggested respectively by Dryden and von Karman:

$$\phi(n) = \frac{A_1}{1 + B_1^2 n^2} \quad \text{and} \quad \phi(n) = \frac{A_2}{(1 + B_2^2 n^2)^{5/6}}$$

While reasonable agreement is obtained with either function it appears that the experimental data are better represented by the Dryden expression in this case. The individual plate wake spectra are also well represented by this expression in the high frequency region. This is an indication of an approach to isotropic turbulence in this region, while anisotropy is indicated in the low frequency plate spectra regions.

Figs. C-1 through C-3 illustrate the downstream development of the turbulence spectra for the individual plates along the centerline. Figs. C-4 through C-6 present the longitudinal development for the individual plate spectra in line with the edge of the plate. Figs. C-7 through C-10 compare the centerline spectra for the three test plates at each of the four longitudinal stations, and Figs. C-11 through C-14 make a similar comparison for the spectra obtained at $y/t = 0.5$. Inspection of these Figures shows the following trends which are worthy of note:

Between about 400 cps and 750 cps the slope of all the spectra is essentially -2 on the log-log plot. At frequencies between the double vortex shedding frequency and about 400 cps the slope is well represented by $-5/3$.

Discrete energy density spikes associated with vortex shedding are very pronounced at $x/t = 1.50$ and at $x/t = 3.25$ for both $y/t = 0$ and $y/t = 0.5$. Spikes associated with the double shedding frequency are pronounced only at the centerline.

Considerable scatter exists in the spectra in the frequency range from 2.5 cps to about 20 cps.

The discrete frequency energy appears to diffuse initially to the random components immediately adjacent in frequency. These components in turn transfer part of their energy to their neighboring components. Thus, as the flow moves downstream the discrete energy spikes are rapidly reduced by diffusion of their energy to the random components in a sort of "relaxation" process.

As the flow moves downstream from $x/t = 1.50$, the

turbulence spectra indicate transition from very pronounced anisotropic turbulence superposed upon strong discrete components of vorticity toward a more isotropic condition of statistical equilibrium. Apparently the high frequency components achieve equilibrium early in the wake, since the portions of the spectra beyond 300 cps do not appear to undergo much change as the flow moves downstream. Hinze suggests a plausible reason for this early achievement of stability in the high frequency end of the spectrum. He points out that the flow within the smallest eddies is no longer turbulent, but viscous, and that the lower limit on turbulent eddy size is determined by dominance of molecular effects (28). In general, the severity of velocity gradients increases with decreasing eddy size. The rate of viscous dissipation of energy associated with large velocity gradients then sets the lower limit on eddy size in accordance with the principles of conservation of energy.

Numerical integration of the first four energy density spectra taken for Plate C resulted in very large energy defects compared to all the other spectra taken. Applying the correction suggested above as a possible means of adjusting for differences in measuring instruments (i.e., normalizing with respect to the Ballantine voltage recorded instead of the voltage reading of the thermocouple voltmeter) only slightly improved the situation. For these spectra A_s still remained less than 50% .

Possible explanations for this large discrepancy are:

- (1) Incorrect wave analyzer calibration constant. This is discussed further in Appendix A.

(2) Abnormally large amounts of energy associated with frequencies above 750 cps. As shown in Fig. VIII, an extended spectrum analysis taken with the Type 1554-A analyzer indicates about 10% of the spectral energy above 750 cps. However, the energy above 750 cps would have to be considerably larger than this to account for the discrepancy.

(3) Presence of an air bubble in the probe tip. If the natural response of the gage-water-column-probe-tip system is located at a frequency just above the range of the wave analyzer, a large amount of energy will exist at this point and will not be measured by the analyzer. It will, however, be measured by the rms voltmeter. This is considered unlikely, however, since two separate probe tip filling operations were involved.

Fig. VIII indicates that the relative magnitude of the four Plate C spectra in question are probably correct, since the pattern is essentially duplicated by the spectrum obtained with the Type 1554-A analyzer.

In order to determine whether the probe tip itself was subject to vibrations in the highly fluctuating flow field, the probe tip opening was plugged with candle wax. The turbulence probe was then located at $x/t = 3.25$ and $y/t = 0.5$ in the wake of Plate C. With a flow of $U_0 = 9.55$ fps, a turbulence intensity of 0.0019 was obtained. With the KinTel amplifier gain increased to 100, the entire spectrum was scanned; response was negligible at all frequencies. With the flow secured a voltage was still measured with the thermocouple voltmeter; this background signal, referred to a flow rate of 9.55 fps, corresponded to an intensity of turbulence of 0.0006.

A graphical presentation of the decay of discrete vortex energy is given below in Fig. IX:

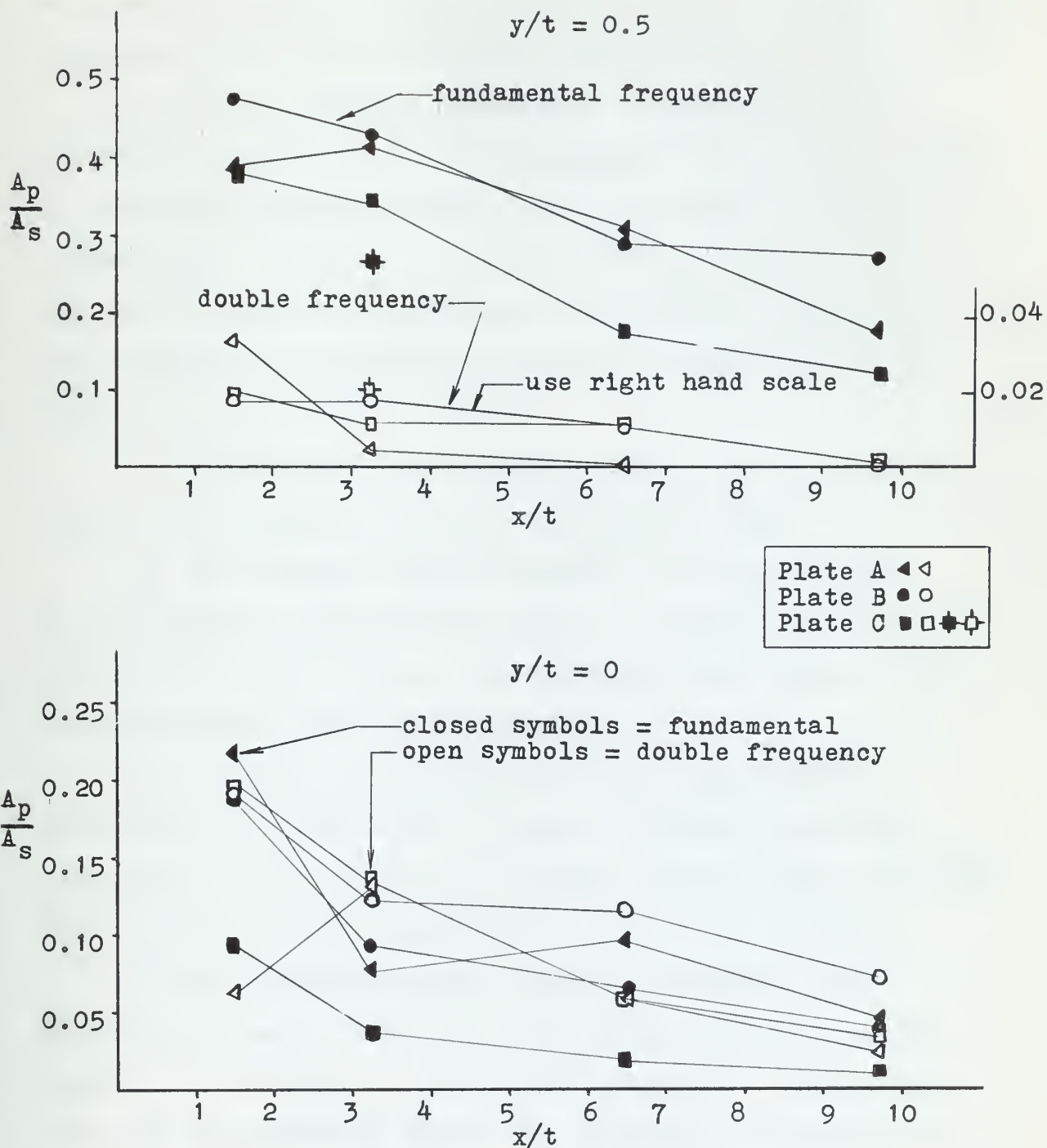


FIGURE IX Decay of Vortex Energy Downstream.

VIII. CONCLUSIONS

A study of the graphical presentation of results included as Appendices B and C indicates the following trends for these test plates at a plate-thickness Reynolds number of 1.9×10^4 :

(1) Sharp geometry transitions (well defined flow separation points) in the trailing edge create a higher level of turbulence intensity in the early wake than do gradual transitions. Turbulence intensity diffuses rapidly out of the wake at a rate proportional to the initial magnitude of the intensity and gradually approaches a decay law proportional approximately to $(x/t)^{-\frac{1}{2}}$.

(2) Strong wake underpressures exist in the early wake behind sharp geometry transition trailing edges.

(3) The energy density spectrum in the early wake is anisotropic, particularly close to the trailing edge where longitudinal and transverse pressure gradients are greatest, and particularly for low frequencies.

(4) The high frequency end of the energy density spectrum in the early wake is seen to approach isotropic conditions. This is also true of the ambient tunnel spectrum. $E(n)$ is seen to vary essentially as n^{-2} in this region.

(5) The discrete energy represented by the vortex shedding frequency is seen to decay downstream in a manner similar to the decay of turbulence intensity. The rounded trailing edge geometry favors the formation of vortices of higher energy content.

(6) The magnitudes of the turbulence intensity found in the early wake close to the trailing edge are in excess of the order of magnitude originally assumed in the

development of the expression for turbulence gage response. These magnitudes must, therefore, be viewed in a qualitative sense only.

(7) A significant percentage (as much as 50%) of the total kinetic energy of a mixed periodic-turbulent wake is associated with discrete vortex shedding frequencies.

(8) Energy associated with vortex shedding frequencies increases initially in the case of the plate with a 90° reentrant angle trailing edge (Plate A), and then decays approximately linearly downstream. Huval⁽¹³⁾ found similar behavior in the early wake behind a 60° included angle trailing edge geometry.

(9) Taking the amount of energy associated with the discrete shedding frequencies in the immediate vicinity of the trailing edge as a measure of the energy available to excite plate vibrations, extrapolation of the trends indicated in Fig. IX indicate that Plate B would tend to vibrate most and Plate A would vibrate least. This is in agreement with results reported by Ippen et al⁽¹⁴⁾.

While centerline vortex energy close to the trailing edge is greatest for Plate A, wake centerline forces exerted on the trailing edge will act equally on either side of the reentrant angle; response to such forces would thus inherently be damped.

IX. RECOMMENDATIONS

The following recommendations are made for the conduct of further investigation of the early wake behind flat plate structures:

(1) The predictability of vortex shedding frequency and the behavior of plate-thickness and vortex-spacing Strouhal number should be investigated as a function of Reynolds number. Vortex spacing should be investigated by traversing the early wake with the turbulence transducer and obtaining transverse distributions of discrete spectral energy.

(2) The behavior of profile drag coefficient with variations in trailing edge geometry should be the subject of a separate investigation. Techniques and instrumentation in this investigation were inadequate for any conclusive understanding of such behavior.

(3) Particular care should be taken to duplicate both flow velocity and tunnel test section pressures for absolute comparison of successive runs.

(4) Tunnel wall spindle cavities should be plugged with plates drilled to accept plate mounting spindles in order to eliminate the possibilities of Helmholtz or stub tube resonance effects. (See Appendix D.) Any other cavities in the tunnel walls in the vicinity of the test plate or transducer should be similarly plugged or faired.

(5) Frequent periodic calibration of measurement equipment and components, particularly when they are battery powered, is mandatory when accurate data is to be obtained over a period of time.

(6) Accurate analysis of energy density spectra requires accurate calibration of analysis equipment. True rms indication of both total energy level and energy density as a function of frequency is desirable. The same instrument or accurately cross-calibrated instruments should be used to measure these quantities.

(7) Consideration should be given to utilizing frequency modulated tape recording equipment to permit determination of autocorrelation functions for the energy density spectra.

APPENDIX A
CALIBRATION PROCEDURE

1. Turbulence Pressure Transducer.

a. General.

The turbulence gage used in this investigation was the same as that employed by Huval^[13]. A quasi-static calibration procedure similar to that used by Huval was used. However, the procedure was simplified as a result of repairs to the transducer made by Hydrodynamics Laboratory personnel which resulted in a greatly increased gage voltage decay time constant.

Huval found the turbulence gage sensitivity to be 63 millivolts per psi, a value substantially lower than the theoretically predicted sensitivity of 100 millivolts per psi. Furthermore, his calibration^[13] showed the gage time constant to be in the vicinity of 0.6 second, considerably lower than that to be expected. Subsequent to Huval's investigation the sensitivity of the gage decreased markedly. Hydrodynamics Laboratory personnel then disassembled the gage and found a small amount of foreign matter on the ceramic face. The ceramic was carefully cleaned and re-assembled. Tests performed prior to the present investigation disclosed that the sensitivity of the gage was increased and the gage time constant was greatly improved.

b. Description of Calibration Procedure.

Fig. A-1 shows schematically the turbulence gage calibration equipment used in this investigation.

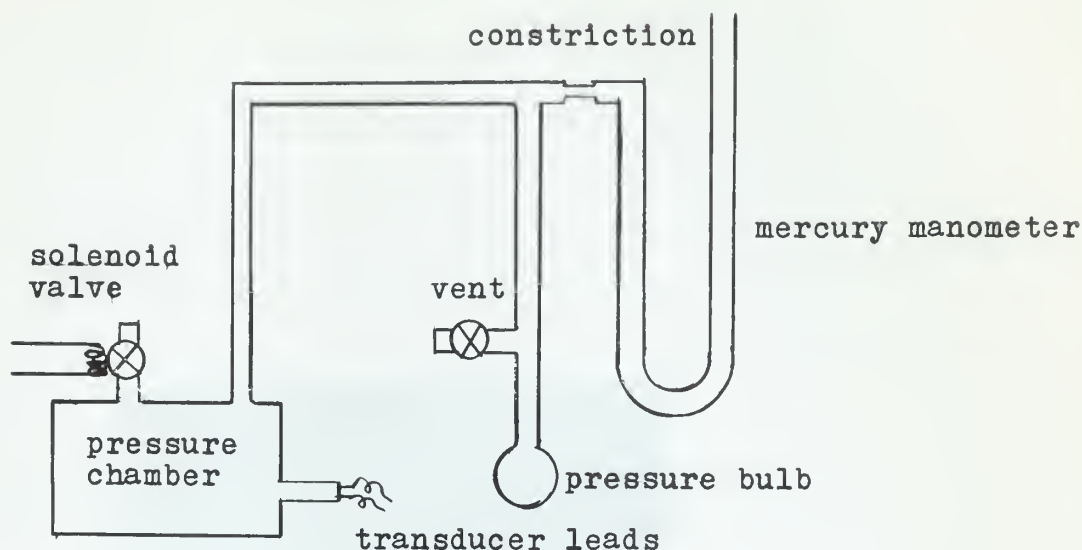


FIGURE A-1 Gage Calibration Schematic

The turbulence gage with probe tip installed was inserted in the tube connected to the side of the cylindrical pressure tank as shown. A differential pressure was built up in the mercury manometer by means of the hand-operated pressure bulb. The clamp in the manometer pressure tube was set to give sufficient damping constriction to reduce pressure oscillations. The solenoid valve at the top of the pressure chamber was opened by means of a trigger circuit which simultaneously triggered the horizontal sweep on the oscilloscope. An oscilloscope camera was used to record the indicated gage response voltage. See Fig. A-2.

A simpler method of calibration, eliminating the use of the oscilloscope camera, was employed for the majority of the

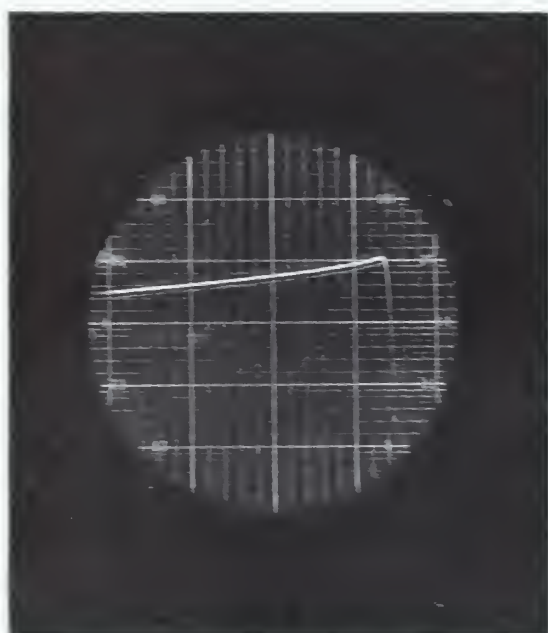


FIGURE A-2 Example of Transducer-Preamplifier Calibration Photograph. (Photograph is reversed; sweep origin is at the right and moves to the left.)

turbulence gage sensitivity calibrations in this investigation. In this alternative method, the oscilloscope sweep rate was increased and the horizontal sweep selector set to "recurring sweep." The vertical deflection of the horizontal sweep at time of pressure release was measured directly on the face of the oscilloscope, manually recording on a strip of paper. One series of photographic calibration runs was made immediately after a series of runs using the simplified procedure. Reproducibility between the two methods was excellent, both yielding the same value for gage sensitivity.

c. Development of the Expression for Turbulence Gage Sensitivity and Time Constants.

The following definitions will be used in this development:

K_{tg} = turbulence gage sensitivity

K_{tp} = transducer-preamplifier system sensitivity

G_p = preamplifier gain

T_v = voltage time constant

T_p = pressure time constant

C_v = $1/T_v$

C_p = $1/T_p$

p = instantaneous pressure at transducer

p_o = initial calibration pressure

V = instantaneous voltage at oscilloscope

As indicated by Huval^[13], the sudden release of pressure from the tank, assuming a suitably damped system, may be represented by the following expressions:

$$\begin{aligned}
 p &= p_0 e^{-C_p t} & , \text{ for } t \geq 0 \\
 p &= p_0 & , \text{ for } t < 0
 \end{aligned}
 \tag{A-1}$$

The incremental change in voltage generated by the turbulence gage is the sum of two components:

$$\Delta V_1 = -K_{tp} \Delta p \quad (\text{pressure-generated component})$$

$$\Delta V_2 = -C_v V \Delta t \quad (\text{voltage decay component})$$

$$\text{Hence: } \Delta V = \Delta V_1 + \Delta V_2 = -K_{tp} \Delta p - C_v V \Delta t \tag{A-2}$$

Rewriting Eq. (A-2) as:

$$\left(\frac{\Delta V}{\Delta t}\right) \Delta t = -K_{tp} \left(\frac{\Delta p}{\Delta t}\right) \Delta t - C_v V \Delta t$$

and taking the limit as $\Delta t \rightarrow 0$, we obtain:

$$\frac{dV}{dt} = -K_{tp} \frac{dp}{dt} - C_v V \tag{A-3}$$

Substituting $p = p_0 e^{-C_p t}$ into Eq. (A-3) we obtain

$$\frac{dV}{dt} = K_{tp} p_0 C_p e^{-C_p t} - C_v V \tag{A-4}$$

Defining $V_0 = K_{tp} p_0$, we see that:

$$\frac{dV}{dt} = V_0 C_p e^{-C_p t} - C_v V \tag{A-5}$$

Multiplying both sides of Eq. (A-5) by $e^{C_v t}$:

$$e^{C_v t} \frac{dV}{dt} + C_v V e^{C_v t} = V_0 C_p e^{(C_v - C_p)t} \tag{A-6}$$

Then:

$$\frac{d}{dt} \left(V e^{C_v t} \right) = V_0 C_p e^{-C_p t} \tag{A-7}$$

Integrating:

$$V e^{C_v t} = \frac{V_0 C_p}{C_v - C_p} e^{(C_v - C_p)t} + C_2 \tag{A-8}$$

where C_2 is the constant of integration, From the initial condition that $V = 0$ at $t = 0$, we find that:

$$C_2 = - \frac{V_0 C_p}{C_v - C_p} \quad (A-9)$$

Then:

$$V = \frac{V_0 C_p}{C_v - C_p} \left(e^{-C_p t} - e^{-C_v t} \right) \quad (A-10)$$

In analysis of the oscilloscope calibration photographs, it is convenient to express V in terms of V_m , the maximum voltage occurring at time t_m . (See Fig. A-2).

From:

$$\left(\frac{dV}{dt} \right) \Big|_{t = t_m} = 0$$

we obtain:

$$e^{-C_p t_m} = \frac{C_v}{C_p} e^{-C_v t_m} \quad (A-11)$$

Also:

$$V_m = \frac{V_0 C_p}{C_v - C_p} \left(e^{-C_p t_m} - e^{-C_v t_m} \right) \quad (A-12)$$

Substituting Eq. (A-11) into Eq. (A-12) and simplifying:

$$V_m = V_0 e^{-C_v t_m} = K_{tp} p_0 e^{-t_m/T_v} \quad (A-13)$$

Solving for K_{tp} in terms of V_m , we obtain:

$$K_{tp} = \frac{V_m}{p_0} e^{t_m/T_v} \quad (A-14)$$

Before going on to the development of expressions for the time constants T_v and T_p , it should be noted from the foregoing expression that if $t_m \ll T_v$, then:

$$K_{tp} \approx \frac{V_m}{p_0} \quad (A-15)$$

This yields a means of obtaining an adequate approximation for K_{tp} without accurate knowledge of either T_v or T_p .

Substituting Eq. (A-13) into Eq. (A-10), the following expression for V may be found:

$$V = \frac{V_m}{1 - T_p/T_v} e^{-(\frac{t-t_m}{T_v})} - e^{-(\frac{t}{T_p} - \frac{t_m}{T_v})} \quad (A-16)$$

If it can be assumed that $T_p \ll T_v$ and $t_m \ll T_v$, the second term within brackets in Eq. (A-16) becomes negligible with respect to the first term for $t \gg t_m$.

Then:

$$V = V_m e^{-\frac{t-t_m}{T_v}} ; \text{ for } t \gg t_m \quad (A-17)$$

Hence:

$$T_v = \frac{t-t_m}{\ln(V_m/V)} ; \text{ evaluated at } t \gg t_m \quad (A-18)$$

To obtain a means of evaluating T_p , evaluating dV/dt from Eq. (A-16) above at $t = 0$ results in:

$$\left(\frac{dV}{dt} \right) \Big|_{t=0} = \frac{V_m}{T_p}$$

and:

$$T_p = \frac{V_m}{[dV/dt]} ; \text{ evaluated at } t = 0 \quad (A-19)$$

This allows evaluation of T_p from knowledge of the initial slope of the V versus t plot.

d. Results of Pressure Transducer Calibration.

A series of seven photographic calibration runs were

made using various values of initial pressure p_0 and using an oscilloscope horizontal sweep rate, calibrated, of 500 milliseconds per inch. A DuMont Oscillograph-Record camera Type 297, using an f-stop of $f/5.6$ with a 5-second exposure, the sweep being triggered 2 seconds after the shutter was opened. Polapan 3000 Type 47 film was used. The time to reach maximum voltage, t_m , was about 30 milliseconds on each run, as compared with a value of about 50 milliseconds reported by Huval.

(1) Pressure Decay Time Constant, T_p .

Eq. (A-19) was used to determine T_p . Values ranged from 11 to 18 milliseconds, with five of the seven values being in the range of 12.5 to 14 milliseconds. An average value of $T_p = 13.7$ milliseconds was obtained.

(2) Voltage Decay Time Constant, T_v .

A plot of $\ln(V_m/V)$ versus $(t-t_m)$ was used to evaluate T_p . See Eq. (A-18). A range of values from 2.4 seconds to 11.4 seconds was obtained, with five of the seven runs in the range 4.4 to 9.0 seconds.

Much of this scatter was due to inability to obtain an absolutely stable reference voltage on the oscilloscope prior to triggering the pressure release. Also, extreme sensitivity of the gage and preamplifier to small unavoidable disturbances during the 2-second period of the horizontal sweep may have contributed to the scatter.

The two extreme values were disregarded, resulting in an average from the remaining five runs of $T_p = 6.4$ seconds.

However, even using the smallest value of T_v and the largest value of T_p , it is seen that:

$$\frac{T_p}{T_v} = 0.0075 \quad \text{and} \quad \frac{t_m}{T_v} = 0.0125$$

This shows that the approximation of Eq. (A-15) is valid for determining K_{tp} and justifies using the simplified procedure described in Section A.1.b above.

(3) Turbulence Gage Sensitivity.

Turbulence gage sensitivity was determined from Eq. (A-15) and the relationship:

$$K_{tg} = K_{tp}/G_p$$

Seven separate series of calibration runs were performed during the course of this investigation between 22 February and 11 April 1961. The dates of the runs are presented in the legend of Fig. A-3.

During the observations made on 6 April, the KinTel amplifier was introduced into the calibration circuit to provide higher output voltage levels. Amplifier gain setting was 30. It was felt that this procedure would serve as a further check on the sensitivity of the entire measuring system. Due to the quasi-static nature of the calibration procedure, the DC filter between the preamplifier and the amplifier was bypassed. The average value of K_{tp} determined for these runs was about 20% lower than the February calibration.

As a check on possible time-deterioration of sensitivity the February procedure was duplicated on 11 April; these runs produced a value of K_{tp} about 4% lower than the original February value. It was concluded that the amplifier must have attenuated the quasi-steady gage response.

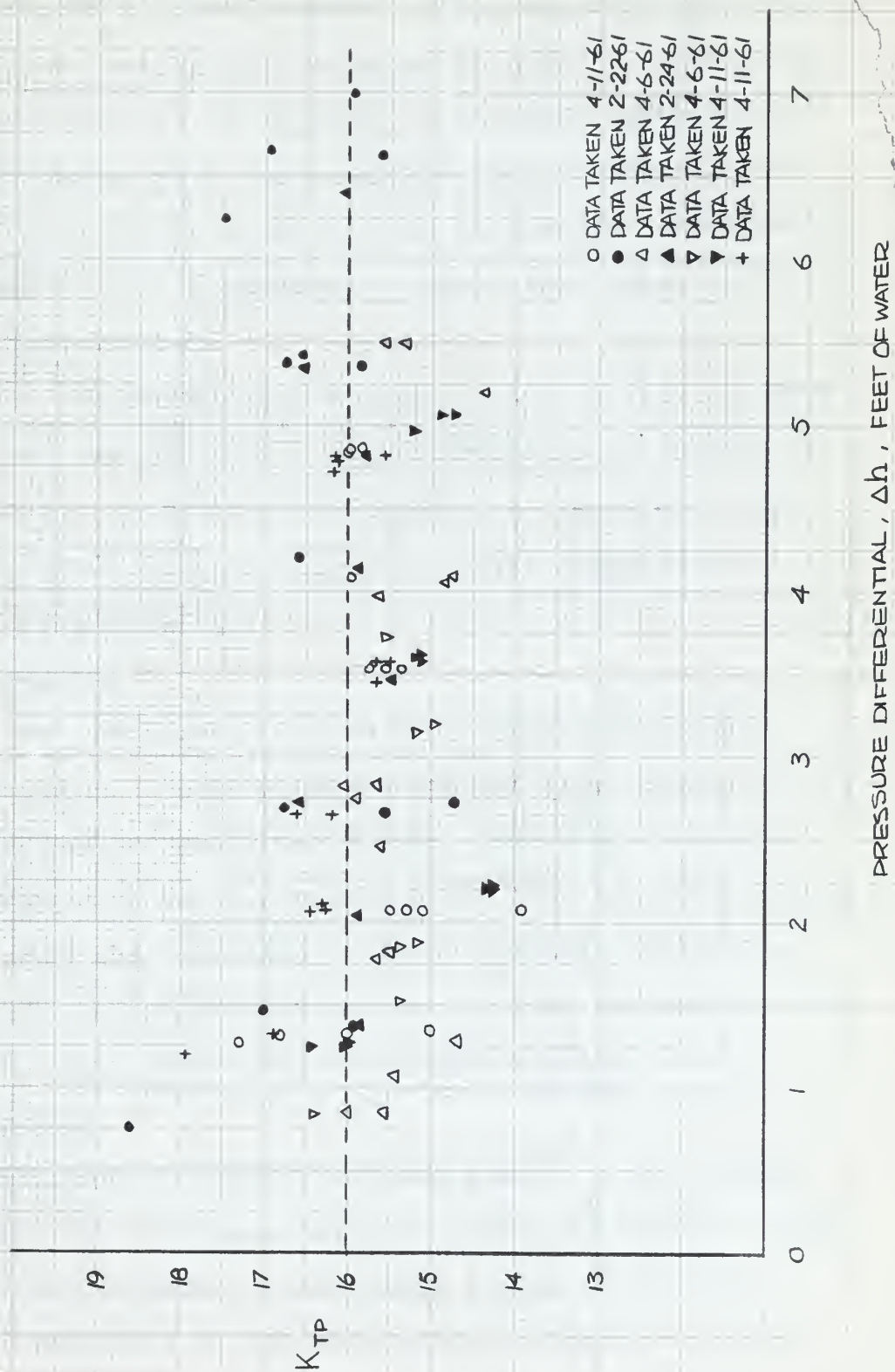


FIGURE A-3 Transducer-Preamplifier Sensitivity Calibration

The amplifier had already been calibrated using an AC signal source and found to have excellent gain response. The amplifier was now calibrated using a DC dry cell through a potentiometer as a signal source. With gain setting of 30, actual gain was measured to be equal to about 27. When the ratio of gain factors was applied to the gage calibration constants obtained with the amplifier in the circuit, the same 40% variation from the initial calibration sensitivity was obtained. It is considered probable that this variation is due to data scatter.

Finally, an average value of $K_{tp} = 16.0$ mv/ft. of water = 36.9 mv/psi was obtained. This corresponds to a value of $K_{tg} = 40$ mv/ft. of water = 92.4 mv/psi, as compared to the theoretical prediction of $K_{tg} = 100$ mv/psi reported by Perkins and Eagleson^[32].

2. Wave Analyzer.

Both wave analyzers used in the investigation were calibrated using a "pure tone" sinusoidal input signal from the Hewlett-Packard audio oscillator. Rms input voltages were measured with the Ballantine VTVM. All calibrations were performed with the vibration analyzer selectivity in the "sharp" position and with vibration analyzer sensitivity set at 10. (All data were taken with these settings also.)

a. General.

As indicated by Perkins and Eagleson^[32], the General Radio Type 762-B Vibration Analyzer output voltmeter reading squared is proportional to the total energy level of the frequency components of the input signal within the narrow

band to which the analyzer is tuned.

b. Wave Analyzer Response.

$$E_{bw} = \int_{n_c - \frac{\Delta n}{2}}^{n_c + \frac{\Delta n}{2}} E(n) dn \quad (A-20)$$

For an input signal with a continuous spectrum of frequencies, if $E(n)$ may be considered constant over the narrow bandwidth of the wave analyzer, (A-20) becomes:

$$E_{bw} = E(n_c) \Delta n = C_1 E(n_c) n_c \quad (A-21)$$

From the statement made in paragraph (a) above, there results:

$$E_{bw} = C_2 R d^2 \quad (A-22)$$

Therefore, combining (A-21) and (A-22) :

$$E(n_c) = \frac{1}{C_v} \cdot \frac{R d^2}{n_c} \quad (A-23)$$

$$\text{where } C_v = \frac{C_1}{C_2}$$

c. Wave Analyzer Calibration Procedure.

The purpose of the wave analyzer calibration is to determine the constant C_v in (A-23) .

One means of obtaining this constant is to set the wave analyzer at a given frequency n_1 , then to apply an input sinusoidal signal from a sine-wave generator. The input signal frequency is increased in small increments from a value (well below n_1) where negligible wave analyzer response is noted, to a value well above n_1 where again negligible

analyzer response results. The input rms voltage e_1 , as measured by an A.C. rms voltmeter, should be kept constant throughout this procedure at a value predetermined to give nearly full scale deflection at maximum wave analyzer response. e_1 is recorded and constantly monitored. At each input frequency n , n and R_d are recorded. Then C_v may be determined from the relationship:

$$C_v = \frac{1}{e_1^2} \int_0^{\infty} \frac{R_d^2}{n_c} dn \quad (A-24)$$

The foregoing procedure should be repeated for several values of n_c over the range of frequencies which are of interest. By this means, any frequency dependency of C_v may be detected.

An alternative procedure (introducing a small error) is to set the input frequency at a constant value n_1 , then shift the wave analyzer frequency in small increments from the point of negligible response on the lower side of n_1 to the point of negligible response on the upper side of n_1 . Then C_v may be approximated from the relationship:

$$C_v = \frac{1}{e_1^2} \int_0^{\infty} \frac{R_d^2}{n_c} dn_c \quad (A-25)$$

The latter method was used throughout this investigation, due to instability of the sine wave generator output voltage introduced by shifting frequencies. Numerical integration was used to approximate the value of the integral.

d. Results of Wave Analyzer Calibrations.

It was noted during this investigation that the wave analyzer calibration constant was dependent upon plate voltage (supplied by two 45 volt batteries).

This was true even when a check of plate battery voltages showed the plate voltage to be within the satisfactory operating range. Therefore, frequent wave analyzer calibration is necessary in order to obtain accurate results. Particularly, the wave analyzer must be recalibrated whenever the plate supply batteries are changed.

It is possible that large discrepancies in the areas of four energy spectra for Plate C may be attributed to failure to calibrate the wave analyzer immediately after a change of plate supply batteries.

On March 28, 1961, wave analyzer plate supply batteries were replaced. The turbulence spectrum measurements were commenced and all eight energy spectra for Plate C were taken between March 28 and March 31, when the wave analyzer was calibrated. The wave analyzer constant was found to be in good agreement with the two previous values determined. However, it was later discovered that the integrals of the energy density spectra were very low for the four spectra measured on March 28 and March 29 compared to those taken on March 30, and, in fact, compared to all the spectra taken for the other two plates. At present, lacking a better reason for this discrepancy, it is conceivable that the wave analyzer constant was very low immediately after the battery replacement

for some unexplainable reason. In evaluation of this possibility, it must be noted that a very low value compared to any previously obtained would have been necessary to explain the discrepancy, and the constant would have increased with analyzer operating time, contrary to the trend previously experienced.

The following values of C_v were obtained during this investigation. Only average values are listed, since each calibration showed little frequency dependence of the constant.

<u>PERIOD</u>	<u>$C_v \left(\frac{1}{\text{volt}^2\text{-cps}} \right)$</u>
3-6-61 to 3-10-61	5.12×10^5
3-10-61 to 3-28-61	5.51×10^5
3-28-61 to 3-31-61	5.31×10^5

3. Amplifier and Preamplifier.

The electrometer preamplifier and the KinTel amplifier were both calibrated using a sinusoidal input signal from a Hewlett-Packard Model 200C audio oscillator.

Calibration of these components was conducted before and after data taking; no time variation of response was observed. The initial calibration was performed for both instruments by measuring both input and output signals with the Ballantine VTVM. This necessitated removing the voltmeter from the input circuit to measure output voltages from the component being calibrated. While this procedure is not considered sound practice, the results of the initial calibration were corroborated by subsequent calibrations. The low frequency limit of the audio oscillator used as a signal generator is 16 cps. Hence, the equipment could not be

calibrated for frequencies below this limit. The initial calibrations were conducted from 16 cps in harmonic increments of 60 cps to an upper limit of 720 cps with continuous oscilloscope monitoring. Gain factors were computed for the preamplifier, and for the amplifier at gain settings of 20, 30, 50, 70, and 100.

The final calibrations were conducted using the Ballantine VTVM for input measurements and the thermocouple voltmeter for output measurements. Simultaneous measurements were taken without disturbing the calibration circuitry. The two meters were previously calibrated against each other with a sinusoidal input signal over the entire frequency range. Finally, the preamplifier and amplifier were calibrated together as a system from 16 cps to 5000 cps with amplifier gain settings of 20 and 30 (i.e., the gain settings actually used during data taking).

The results of these calibrations are presented in Fig. A-4 as a plot of relative attenuation or loss in gain in db versus frequency.

The measured gain of the preamplifier is seen to exhibit some attenuation above 350 cps; the response of the amplifier is essentially flat up to 750 cps, which is the upper limit of the Type 762-B Vibration Analyzer. The preamplifier gain was taken as constant over the operating range of the investigation at a value $G_p = 0.40$, which was the arithmetic mean value. The amplifier gain was $G_a = 20$ with a gain setting of 20 and $G_a = 30$ with a gain setting of 30.

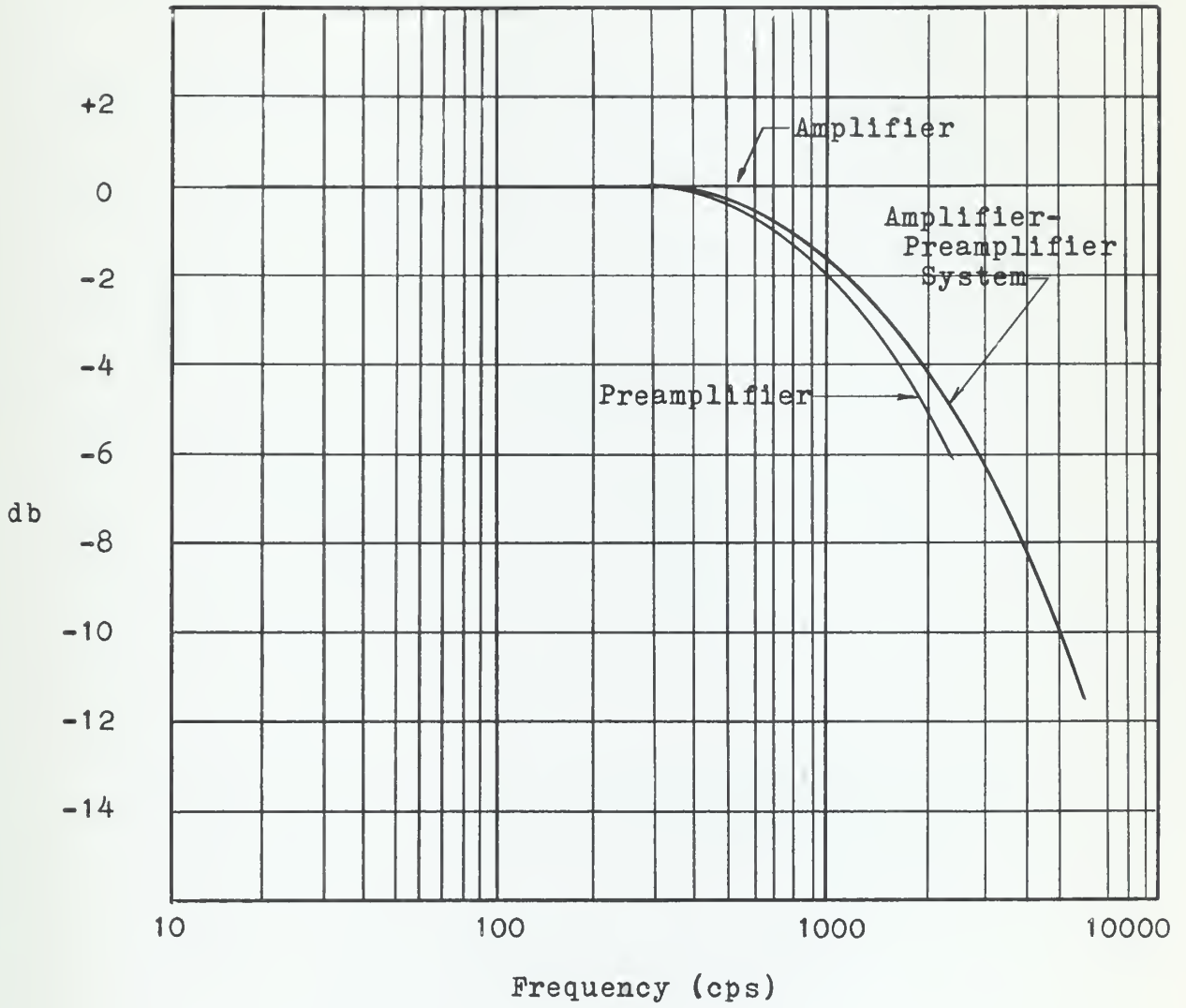


FIGURE A-4 Component and System Gain Response

The electrometer preamplifier was calibrated and operated throughout with a screen grid bias of +2.0 volts. A circuit diagram of the electrometer preamplifier is presented in Fig. A-5.

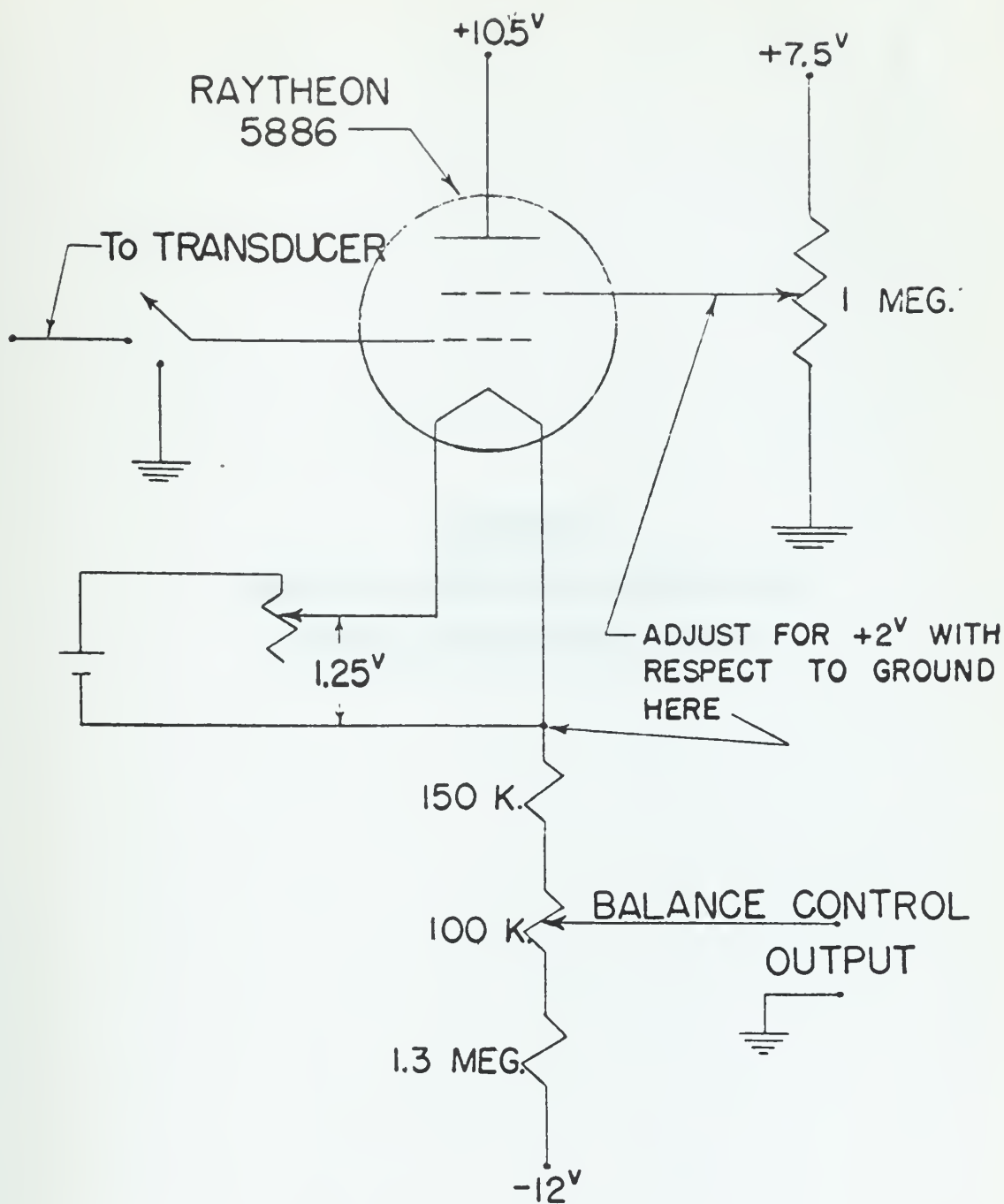


FIGURE A-5 Electrometer Preamplifier Circuit Diagram
(From Huval, "The Early Wake of a Fixed, Flat Plate.")

APPENDIX B
VELOCITY, TURBULENCE INTENSITY AND
PRESSURE DISTRIBUTION PROFILES

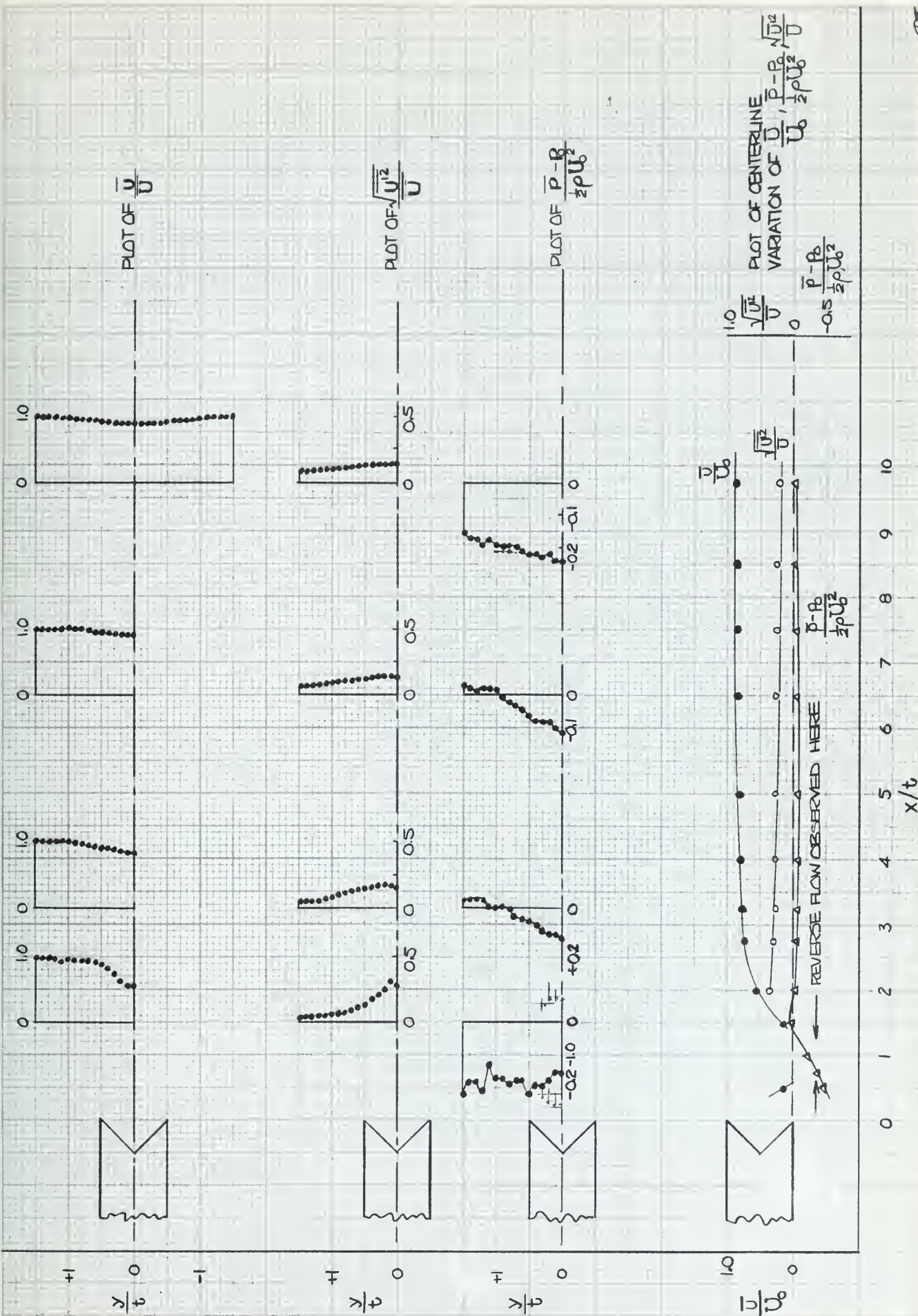


FIGURE B-1 Wake Structure Summary Plot, Plate A

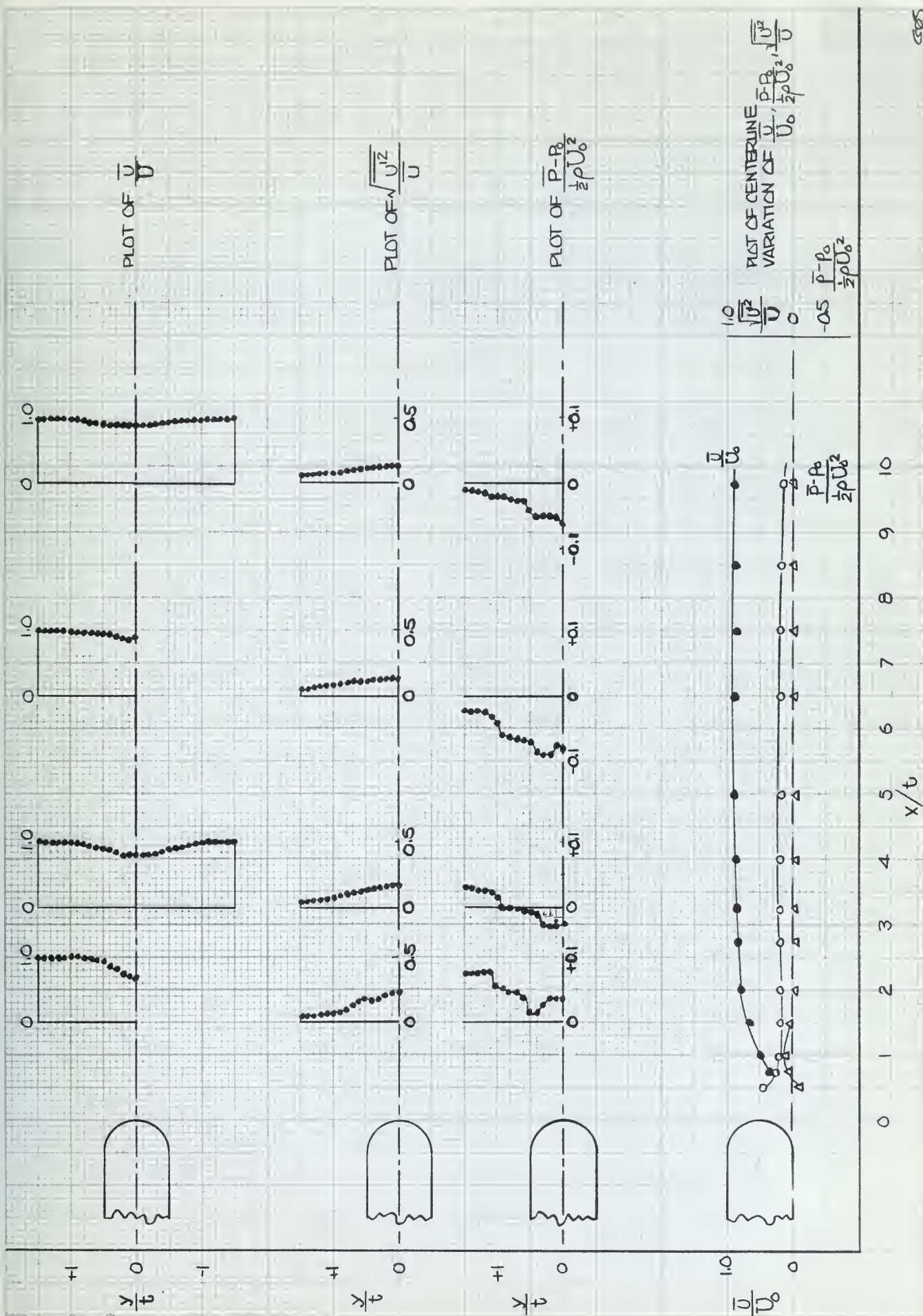


FIGURE B-2 Wake Structure Summary Plot, Plate B

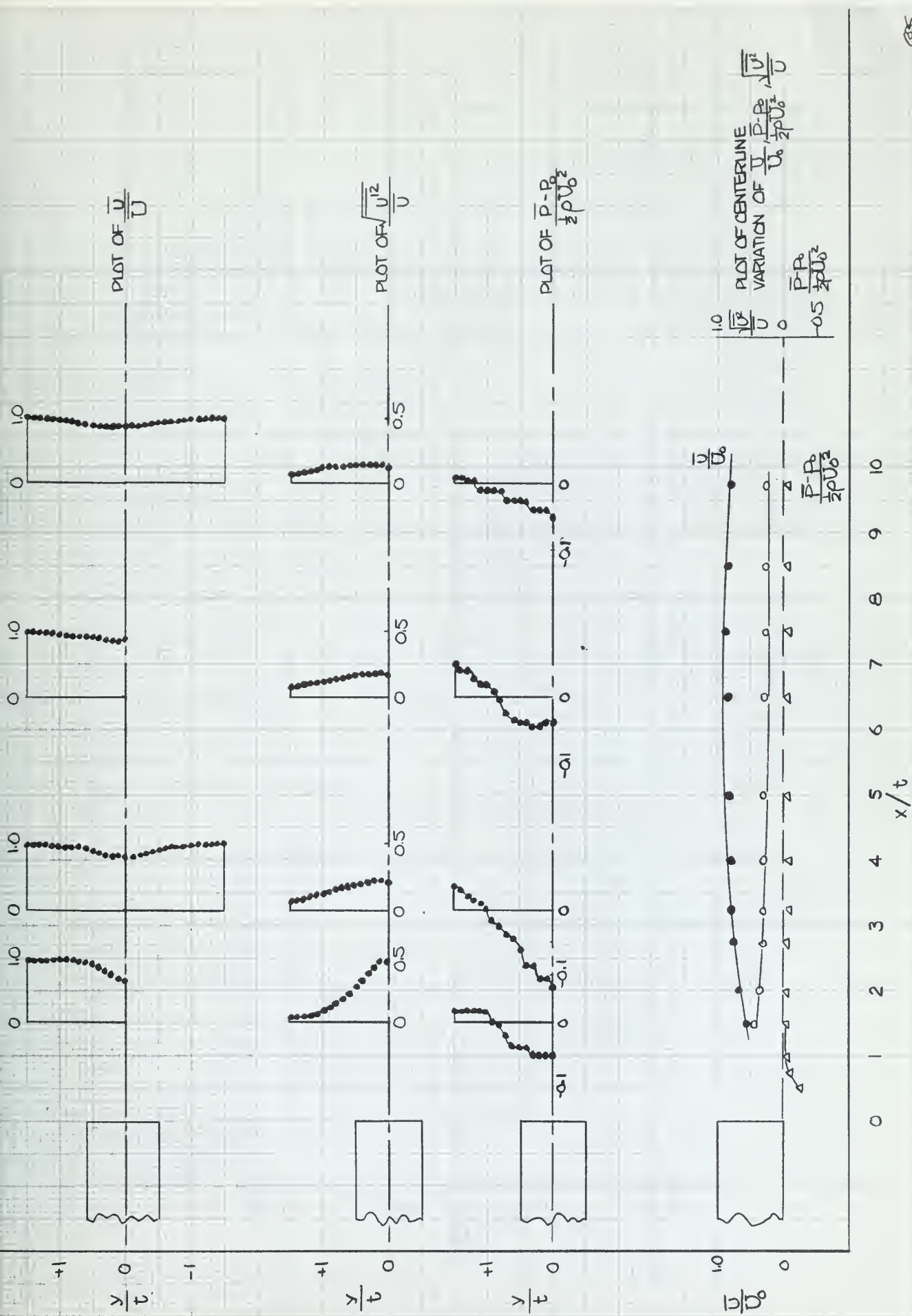


FIGURE B-3 Wake Structure Summary Plot, Plate C

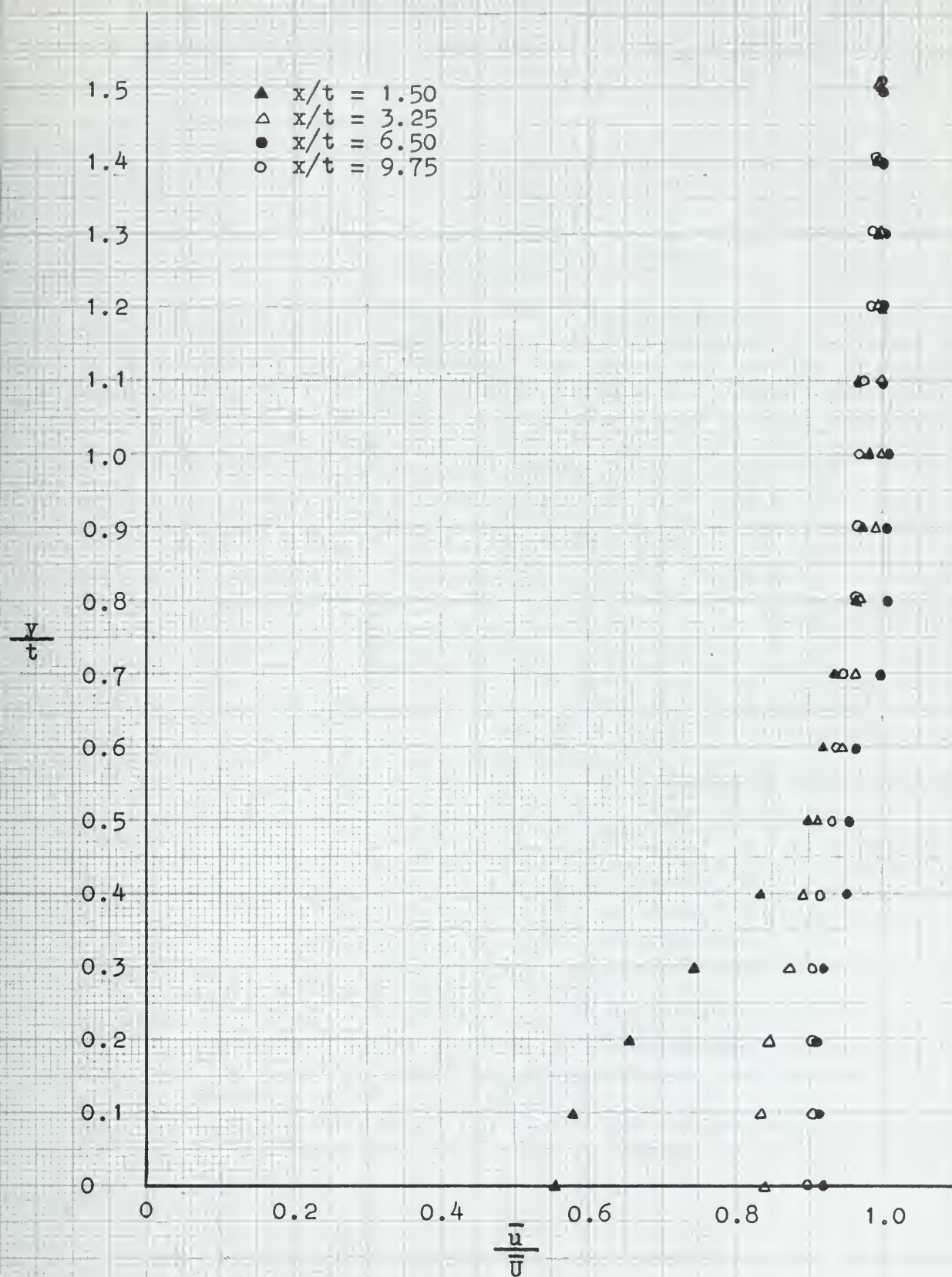


FIGURE B-4 Transverse Velocity Profile, Plate A

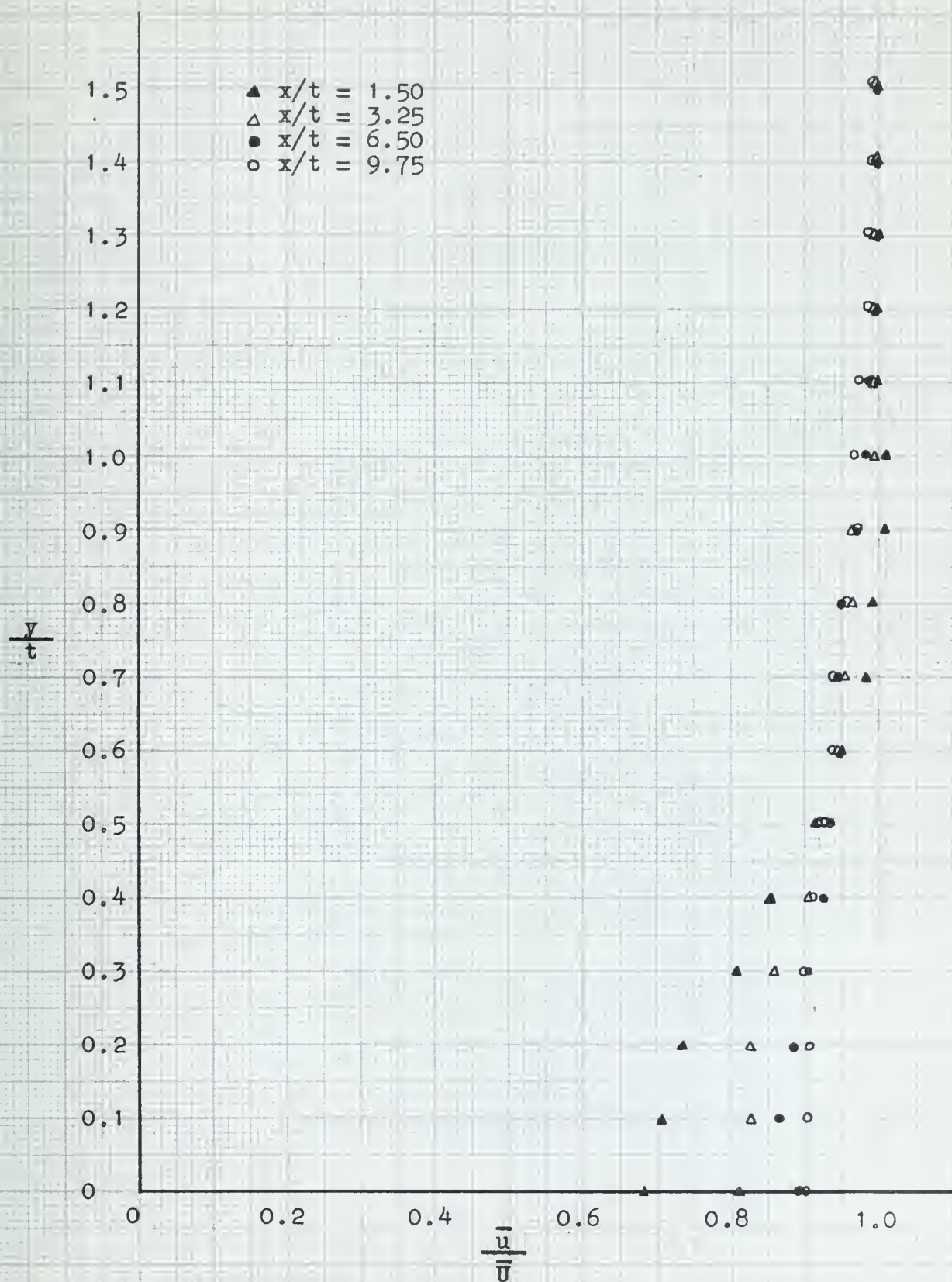


FIGURE B-5 Transverse Velocity Profile, Plate B

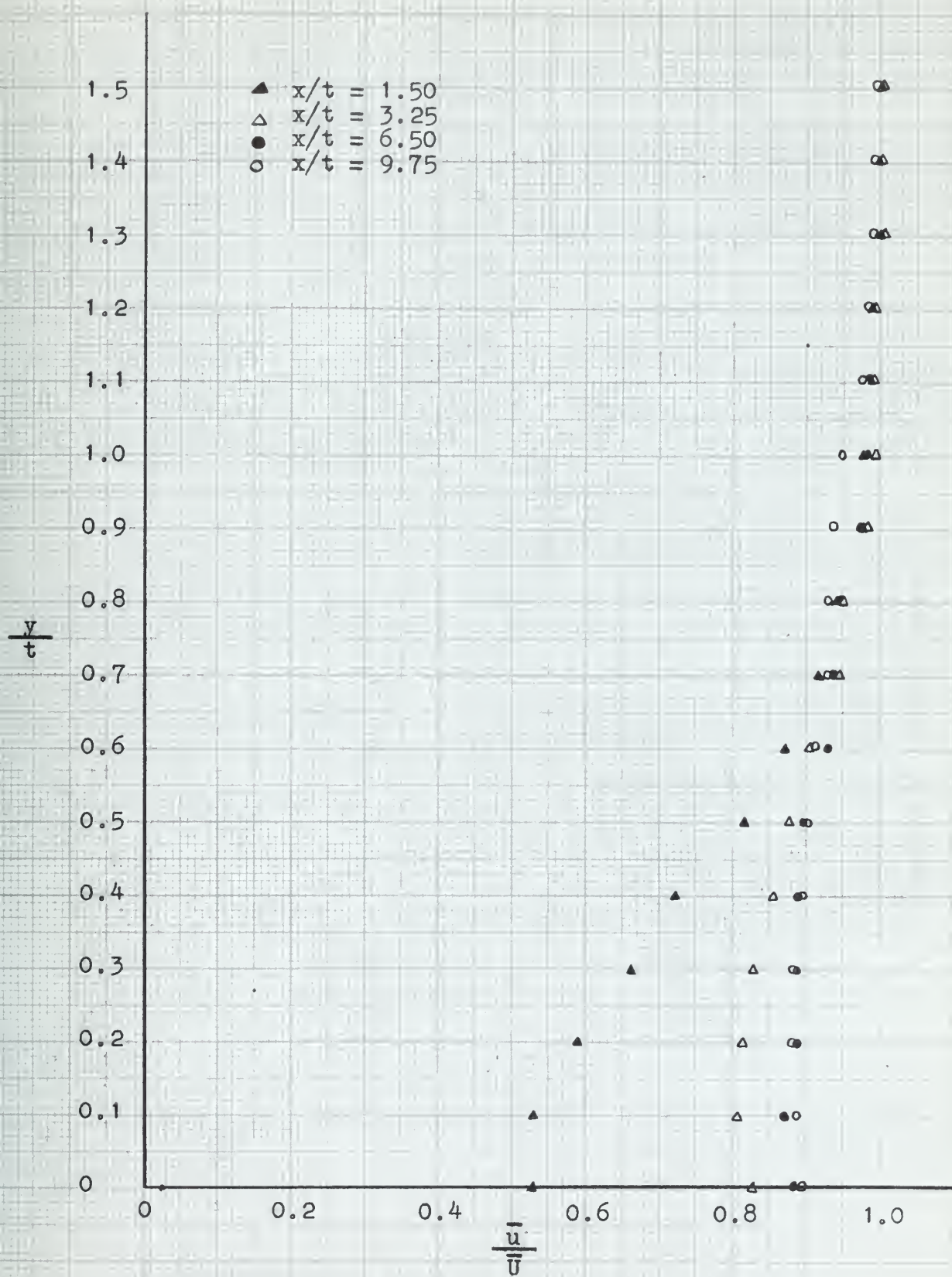


FIGURE B-6 Transverse Velocity Profile, Plate C

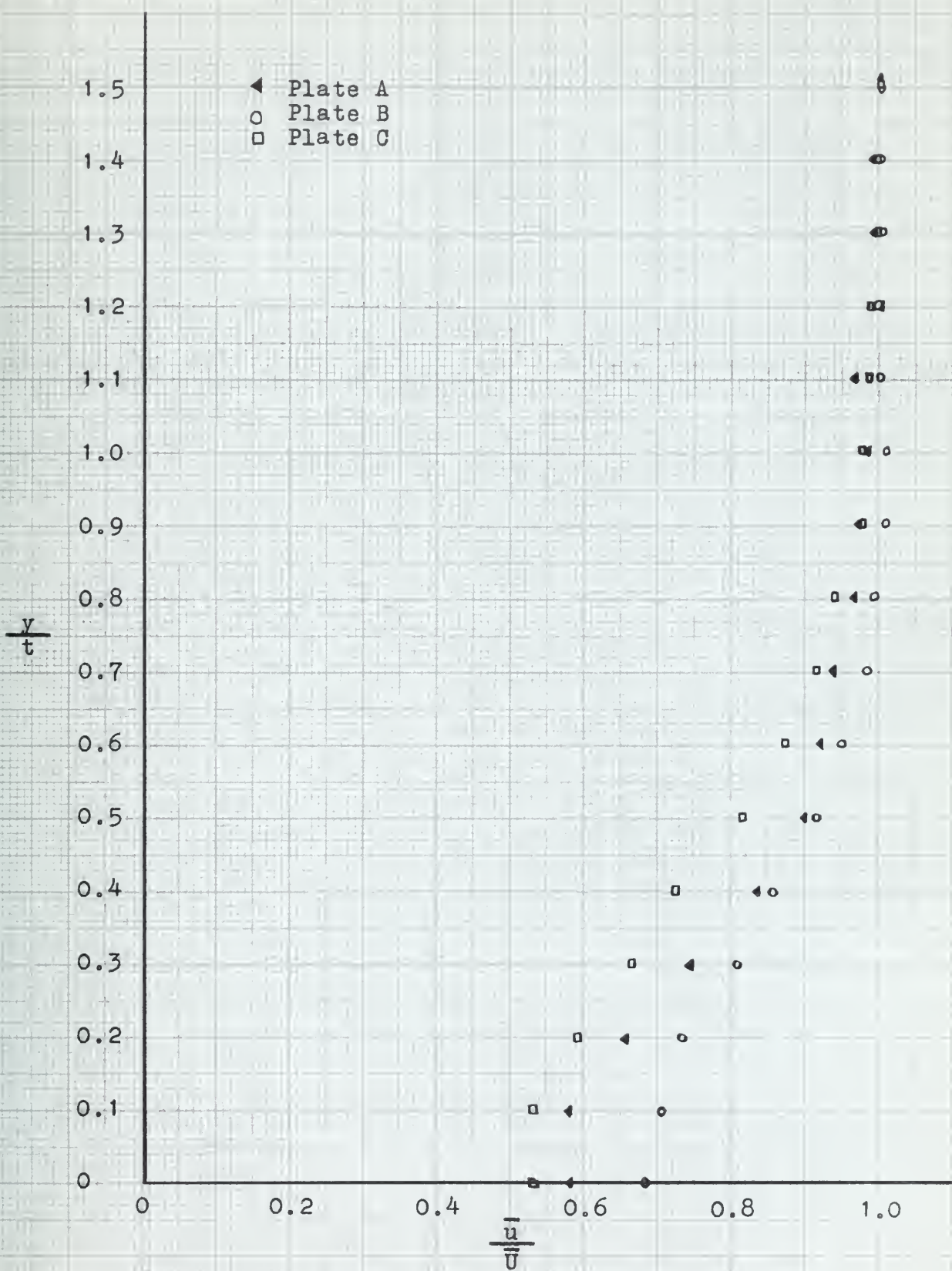
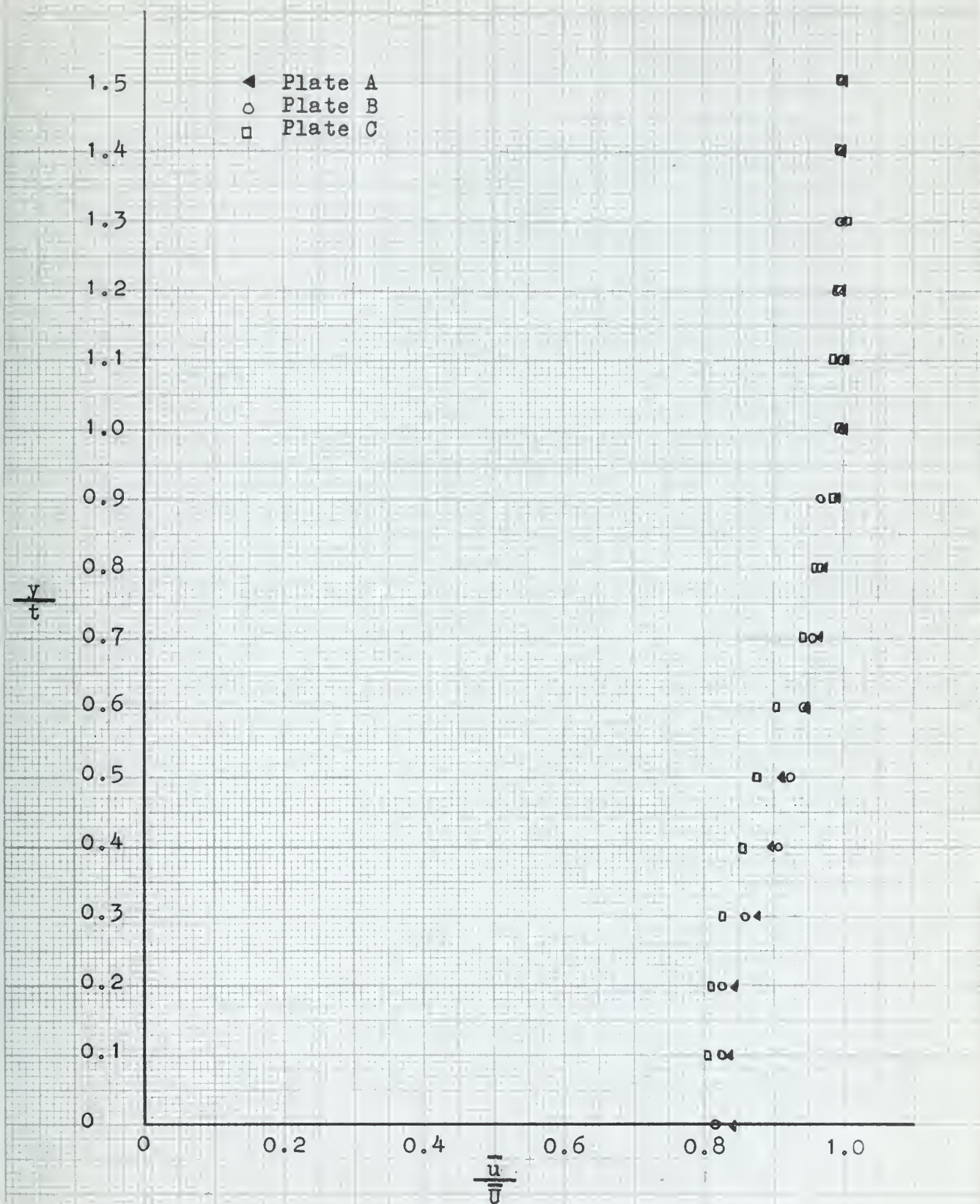


FIGURE B-7 Comparison of Velocity Profiles at $x/t = 1.50$

FIGURE B-8 Comparison of Velocity Profiles at $x/t = 3.25$

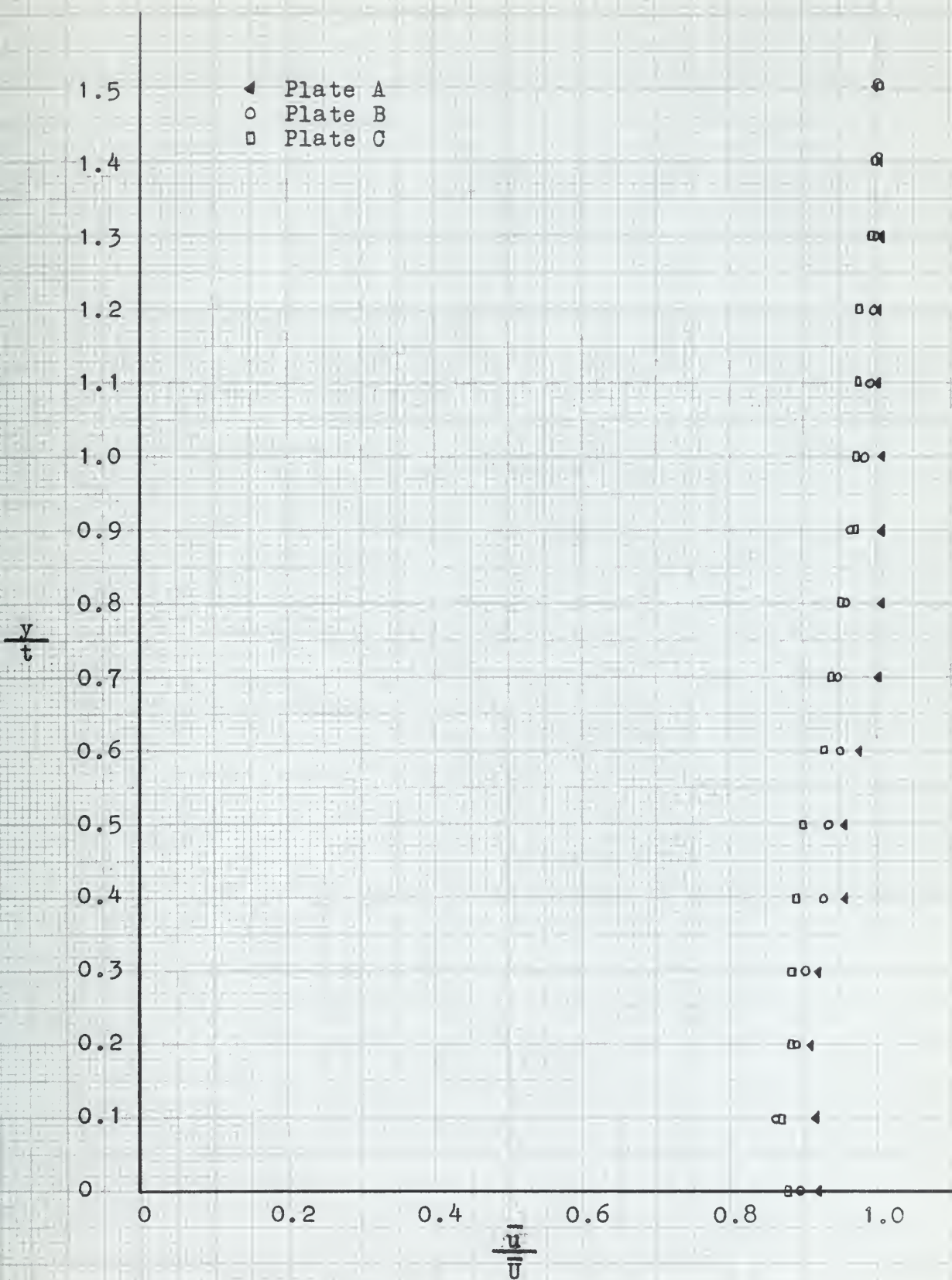


FIGURE B-9 Comparison of Velocity Profiles at $x/t = 6.50$

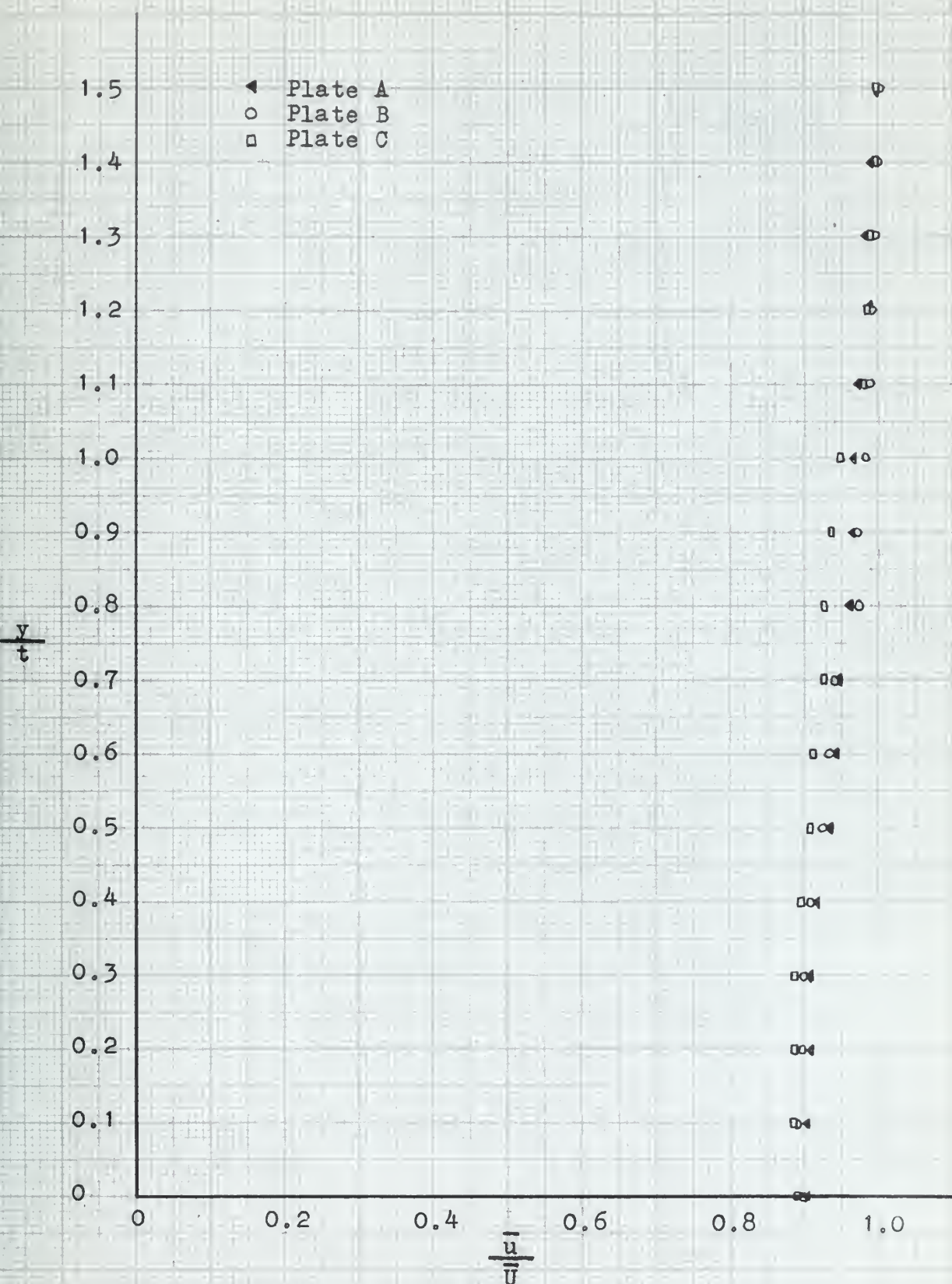


FIGURE B-10 Comparison of Velocity Profiles at $x/t = 9.75$

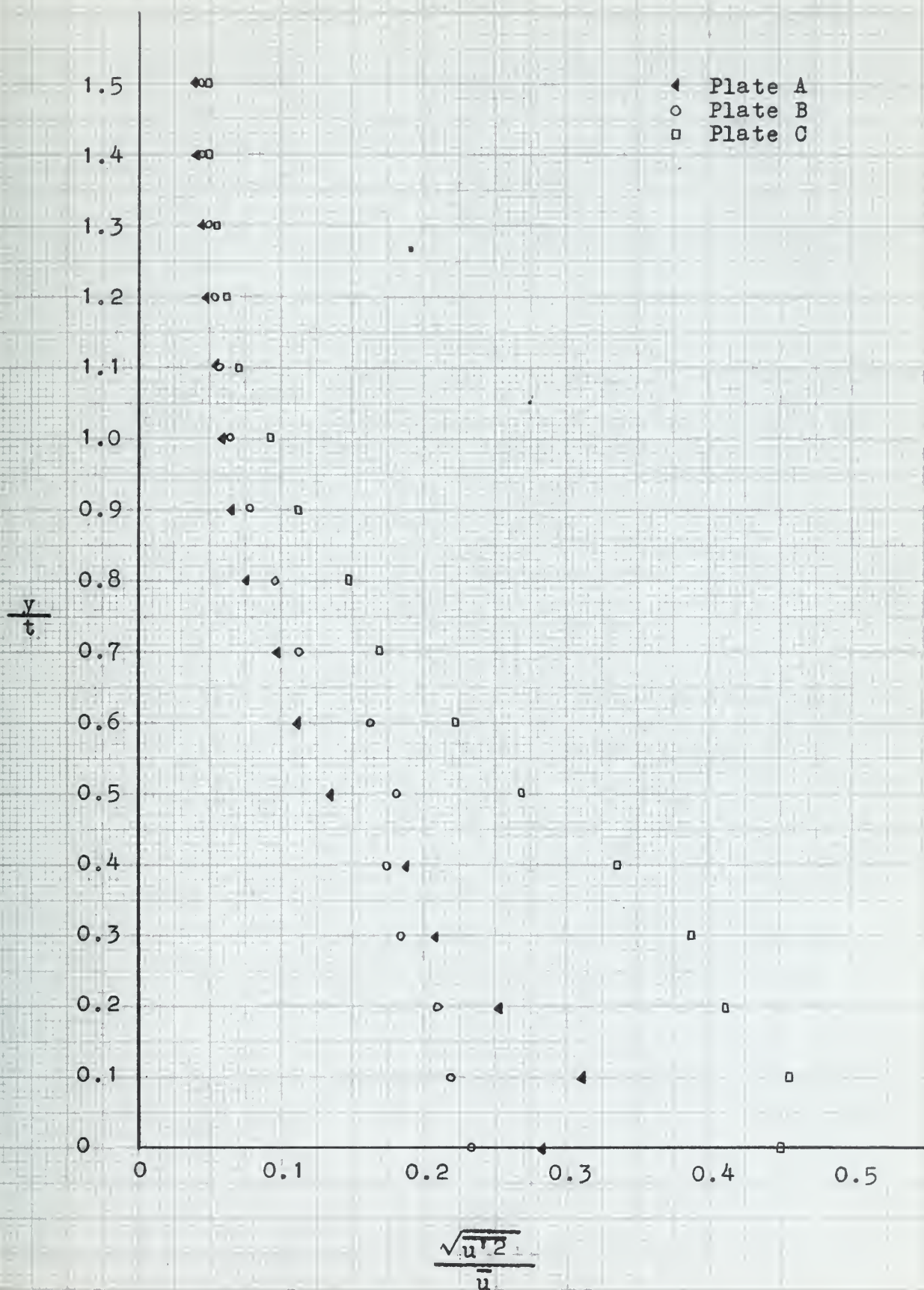


FIGURE B-11 Turbulence Intensity Distribution at $x/t = 1.50$

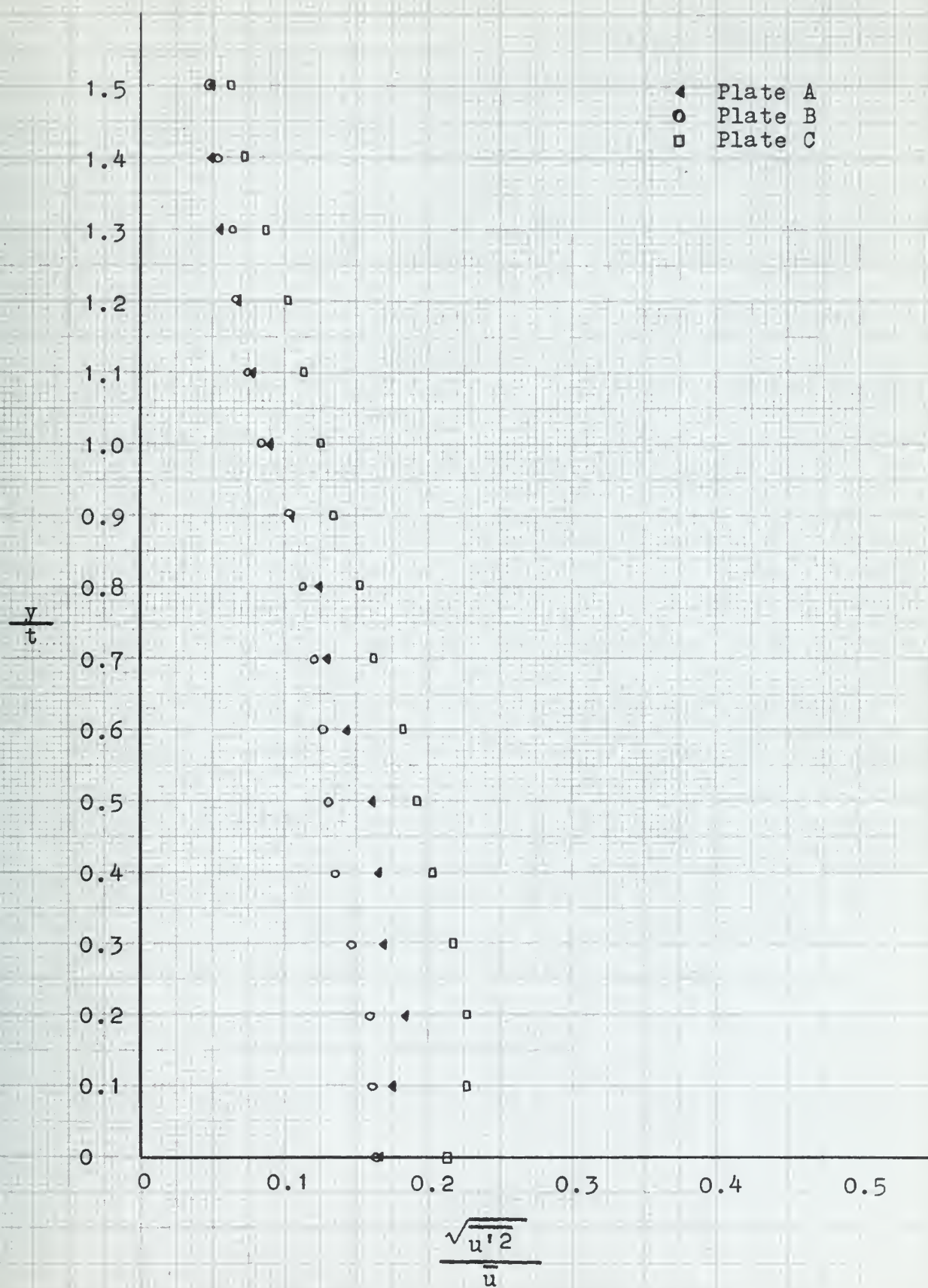


FIGURE B-12 Turbulence Intensity Distribution at $x/t = 3.25$

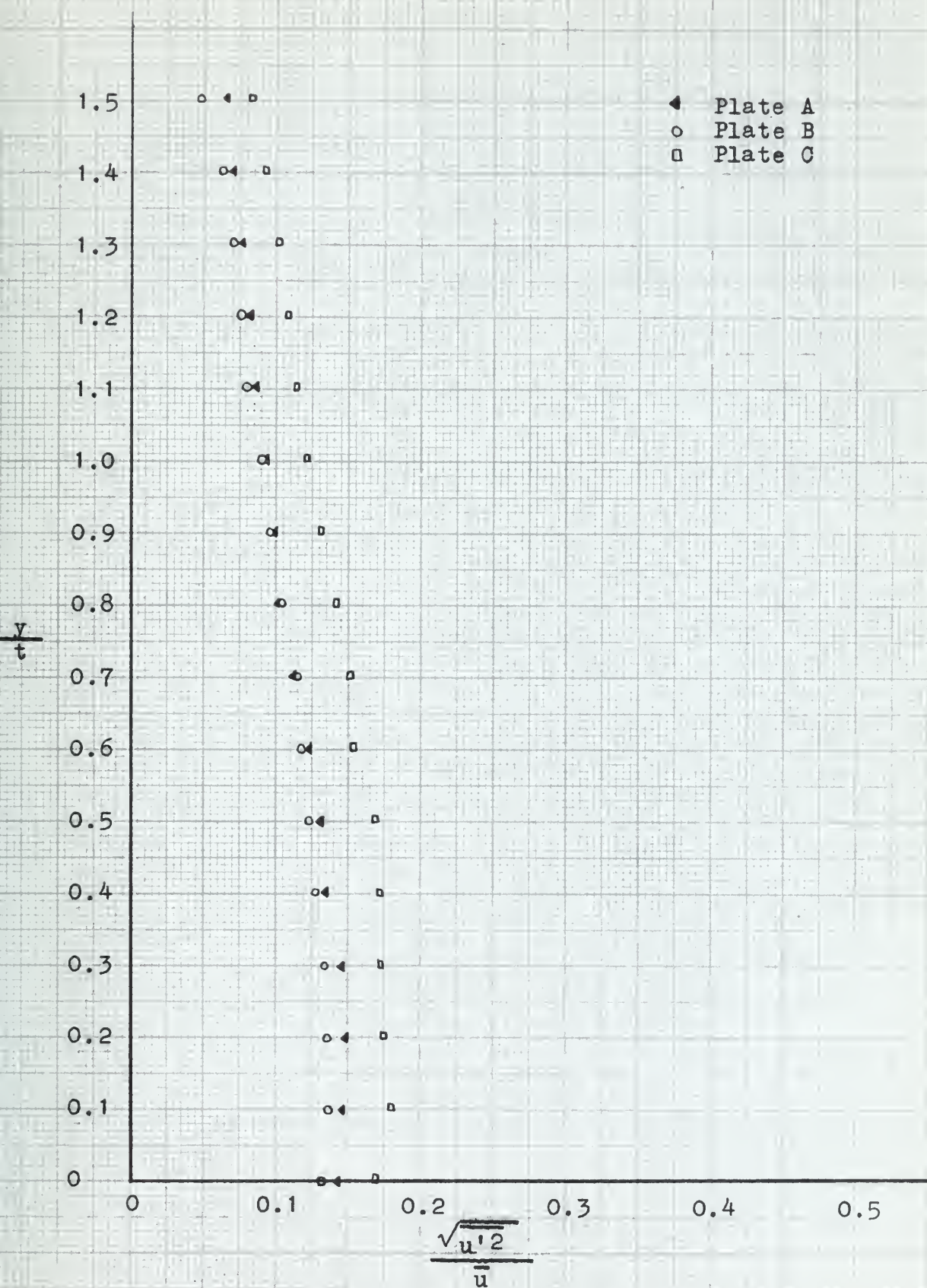


FIGURE B-13 Turbulence Intensity Distribution at $x/t = 6.50$

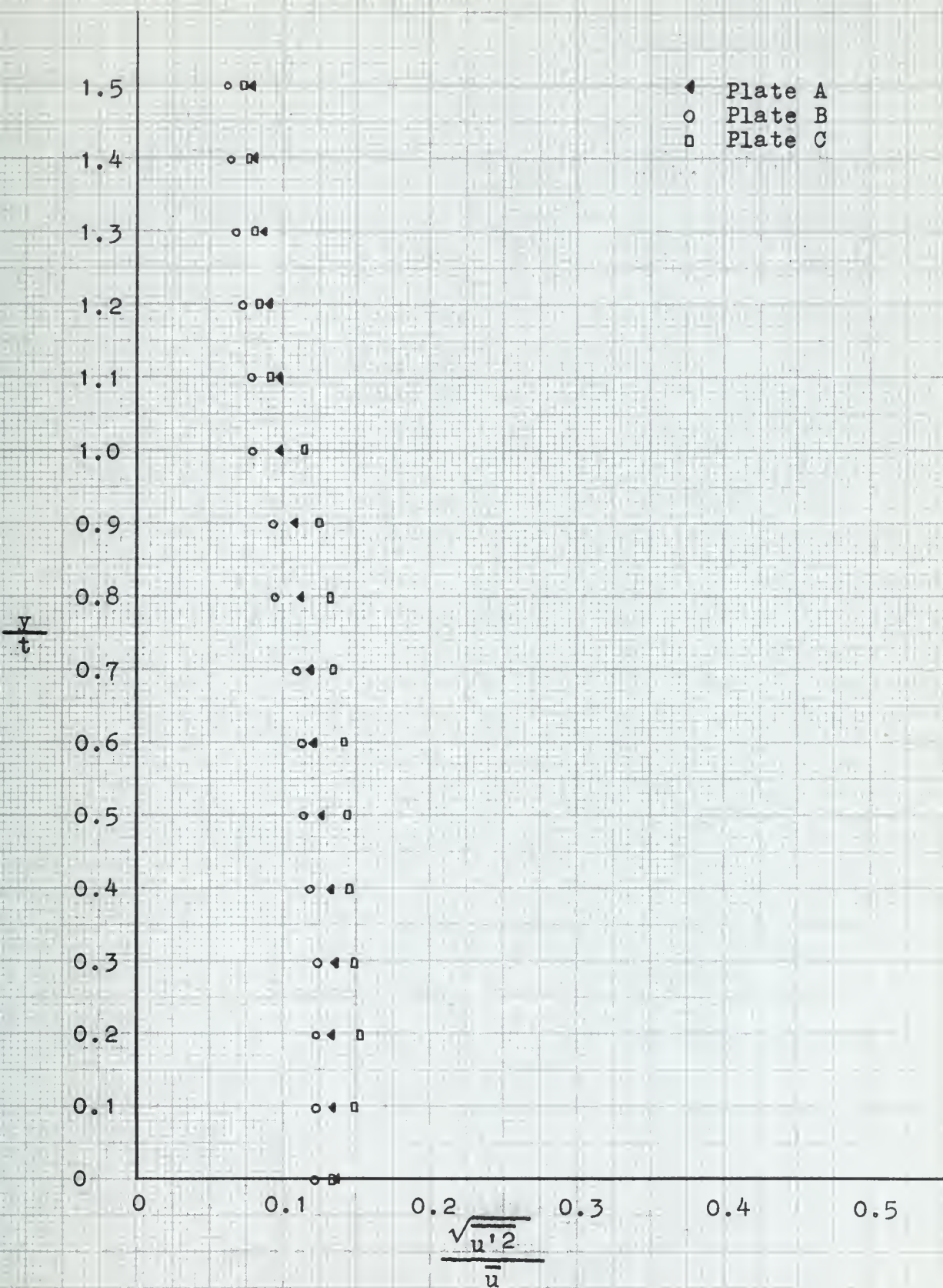
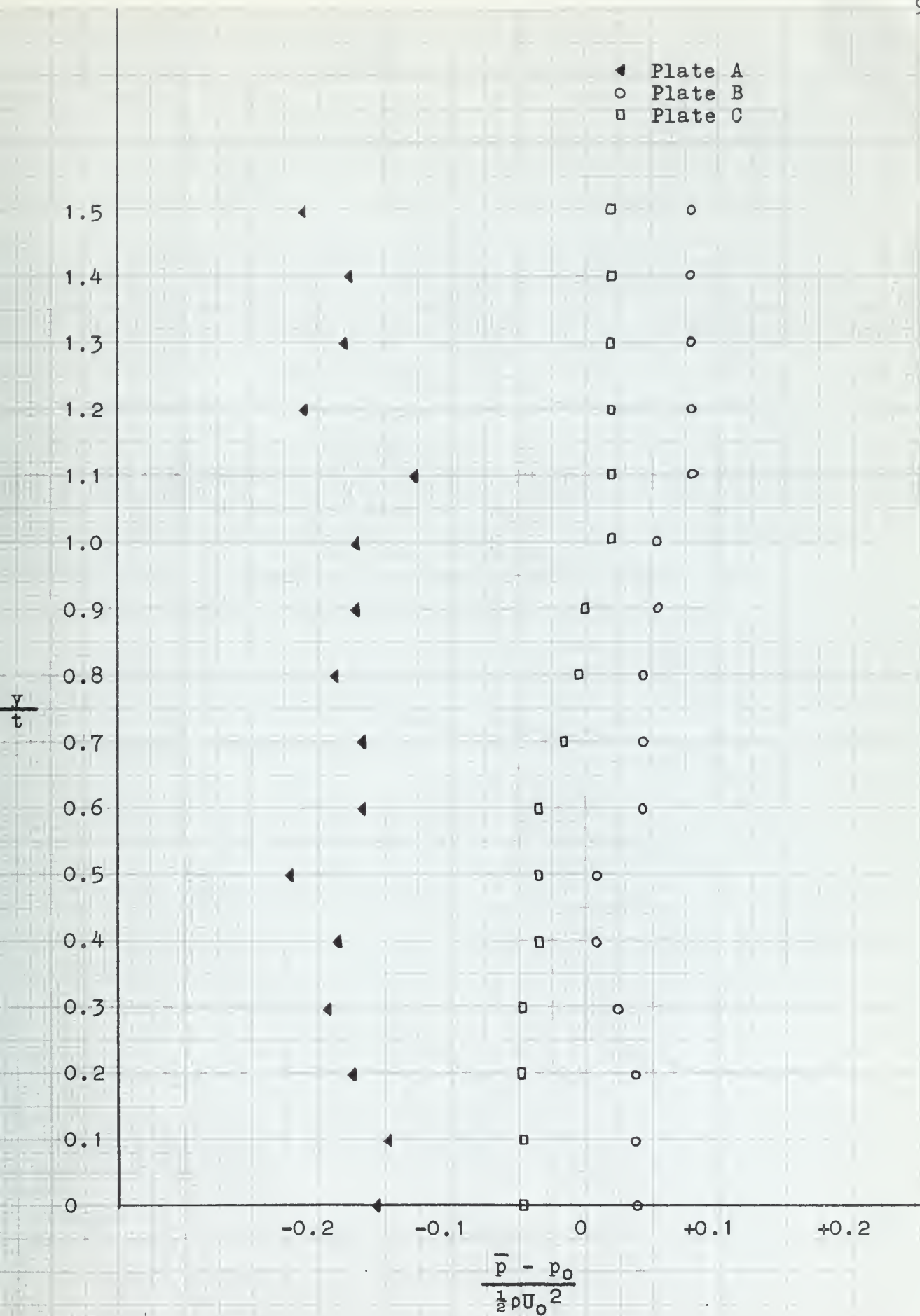
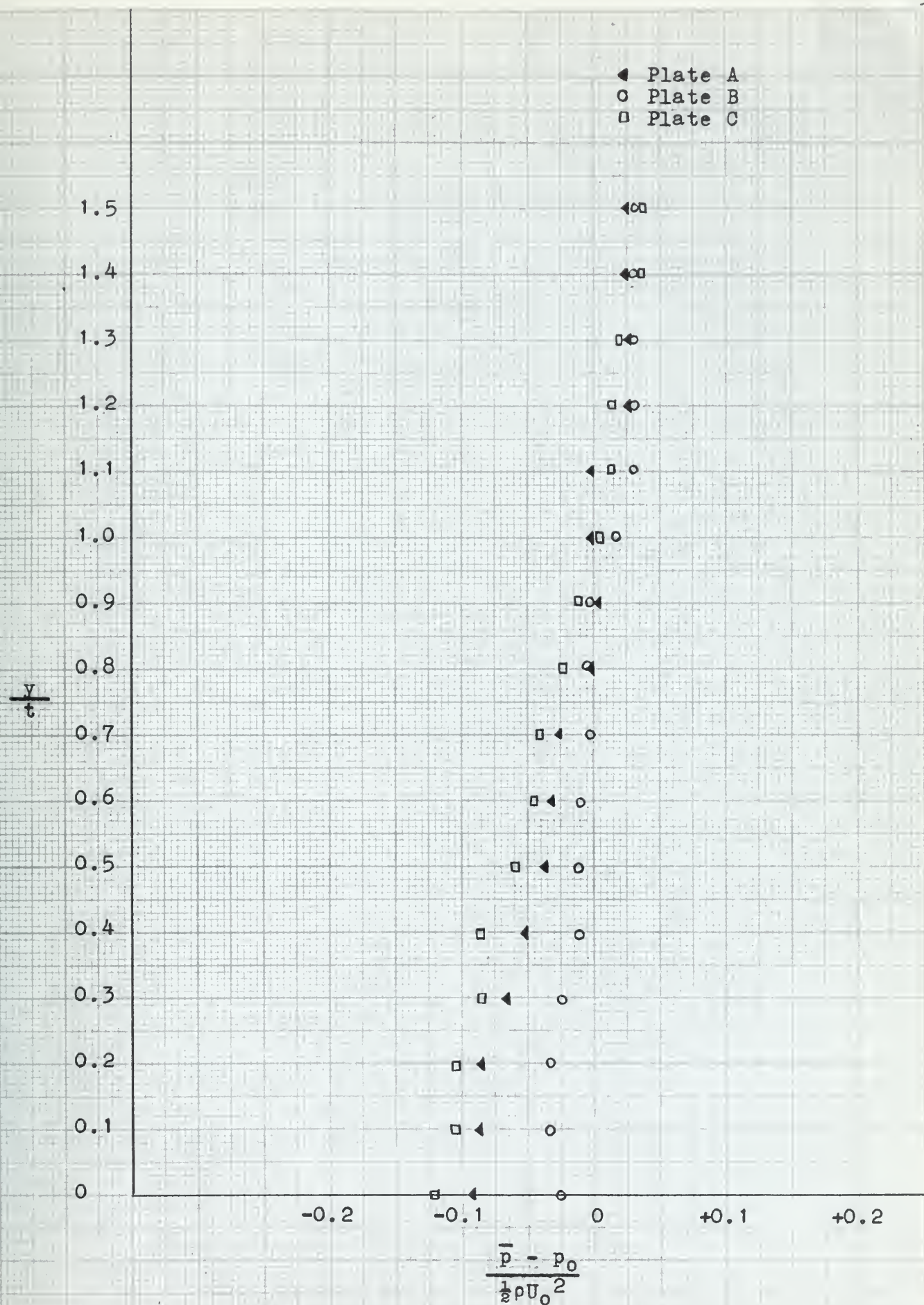
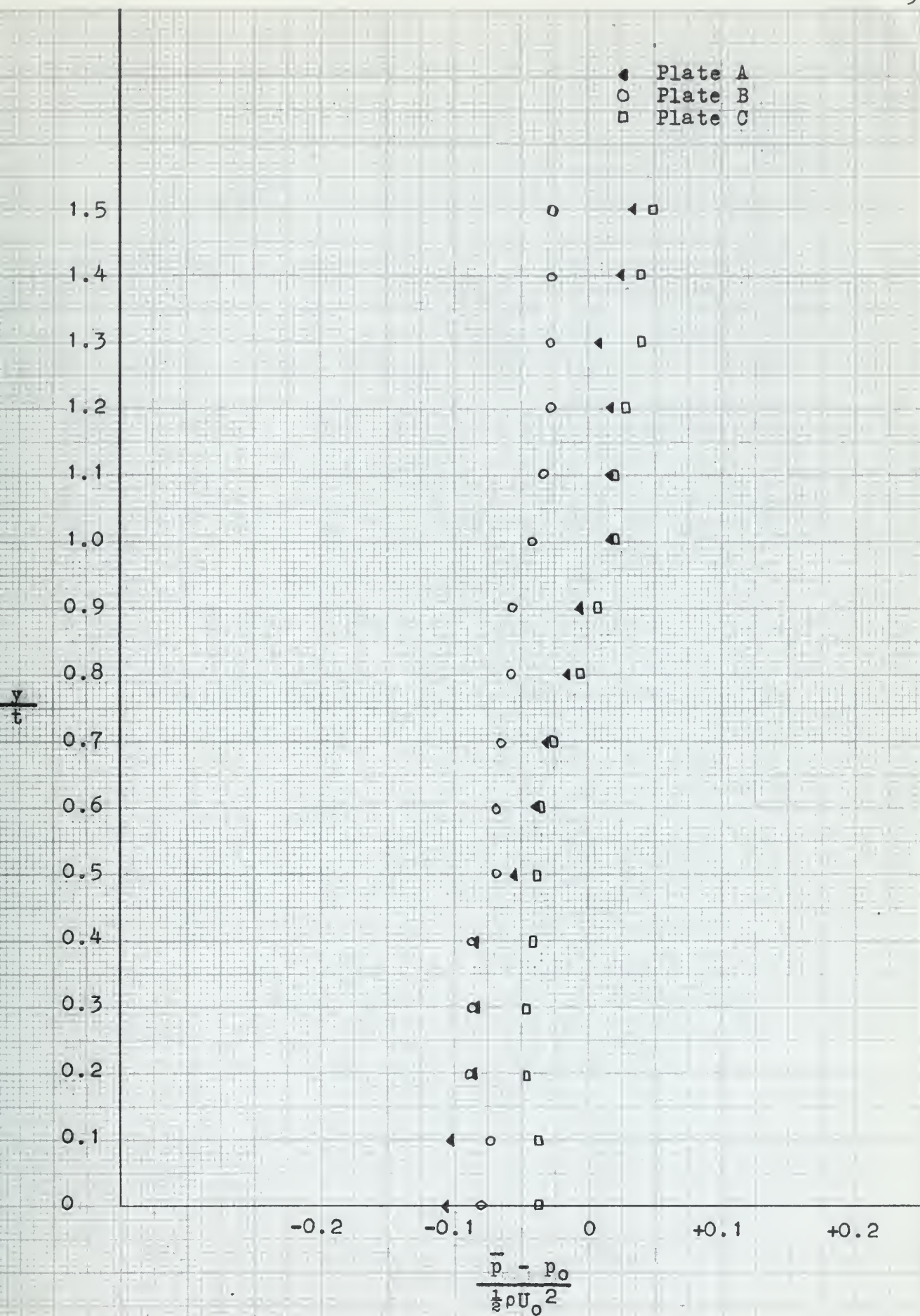
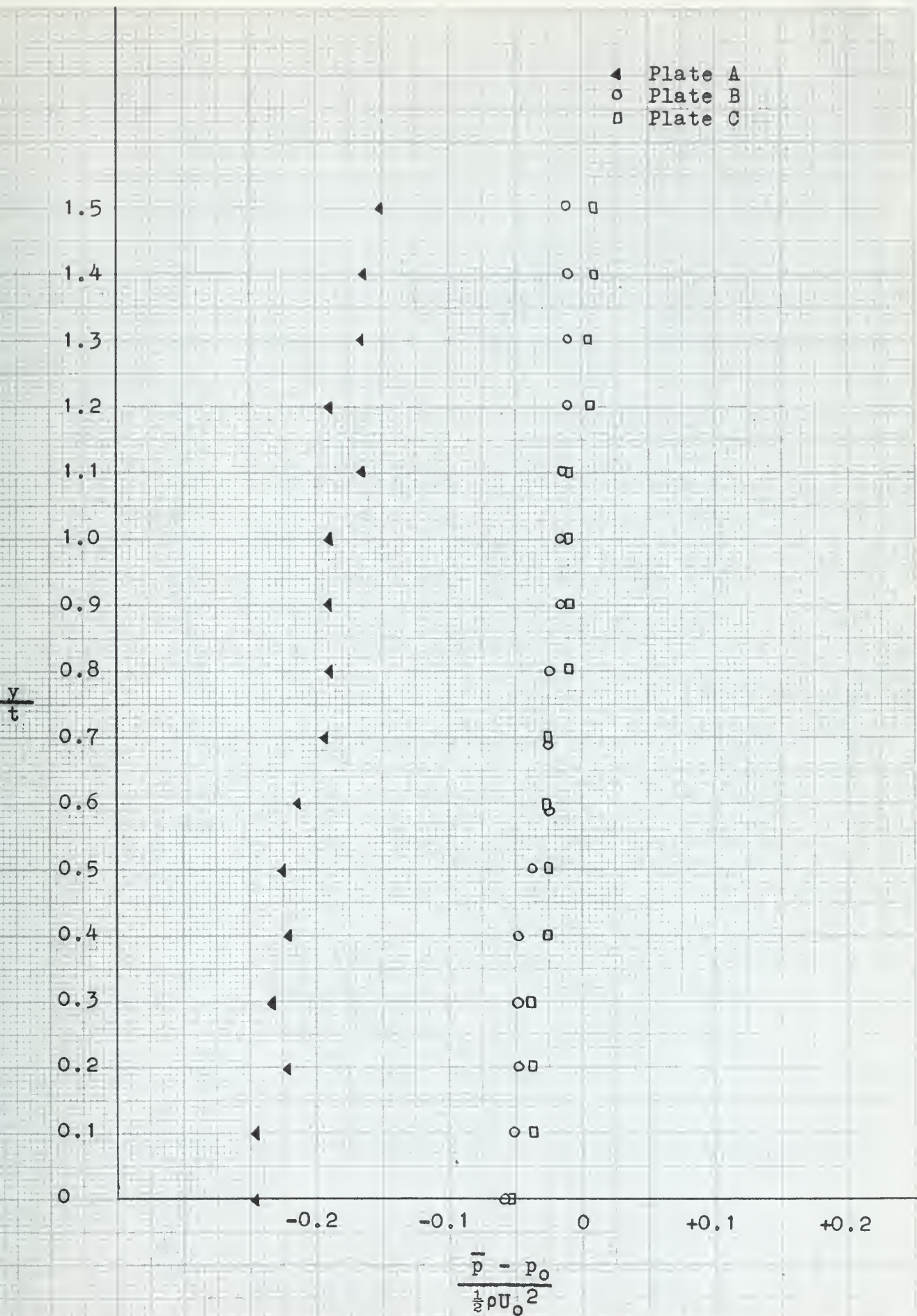


FIGURE B-14 Turbulence Intensity Distribution at $x/t = 9.75$


 FIGURE B-15 Pressure Coefficient Distribution at $x/t = 1.50$

FIGURE B-16 Pressure Coefficient Distribution at $x/t = 3.25$

FIGURE B-17 Pressure Coefficient Distribution at $x/t = 6.50$


 FIGURE B-18 Pressure Coefficient Distribution at $x/t = 9.75$

▲ PLATE A
 ○ PLATE B
 □ PLATE C

$y/t = 1.50$

$y/t = 0$

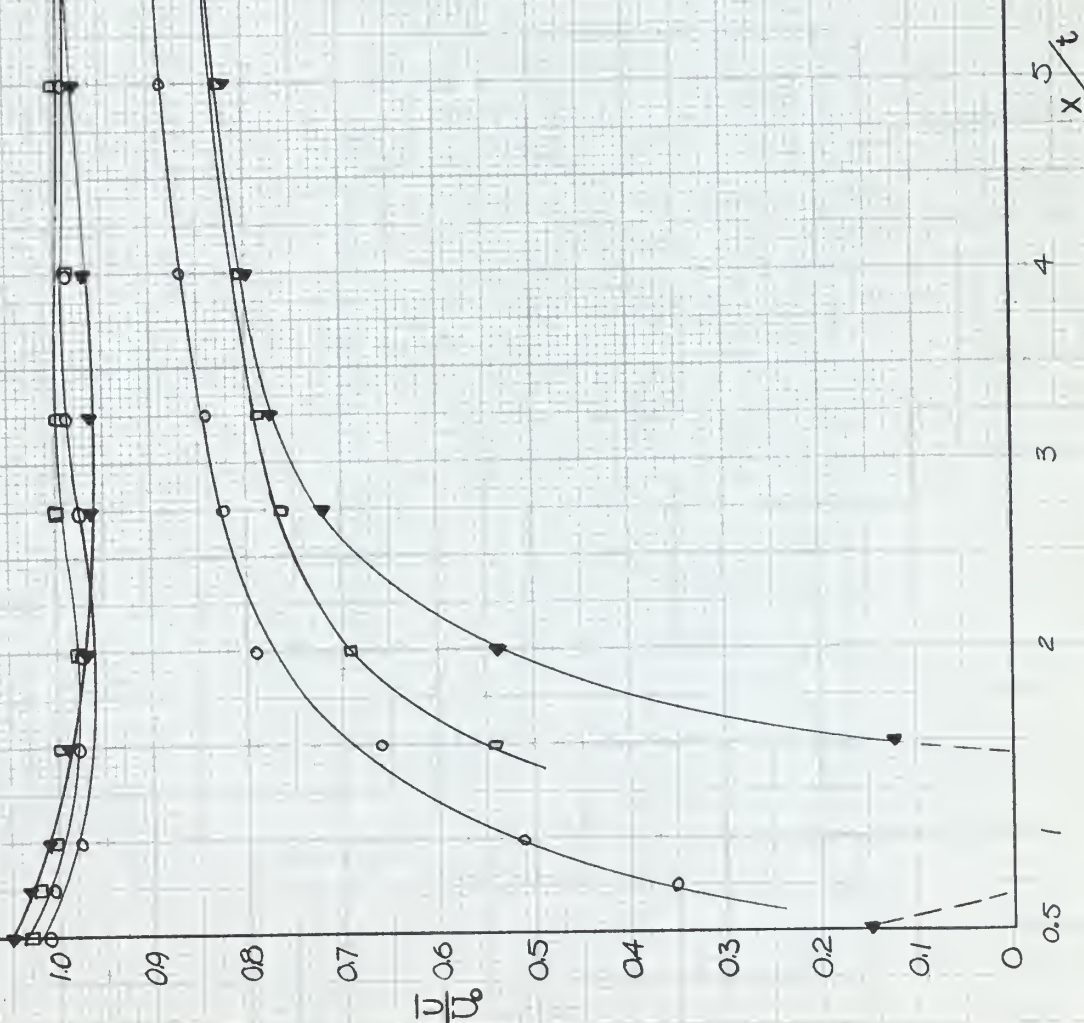


FIGURE B-19 Longitudinal Dimensionless Velocity Distribution

▼ PLATE A
 ○ PLATE B
 □ PLATE C

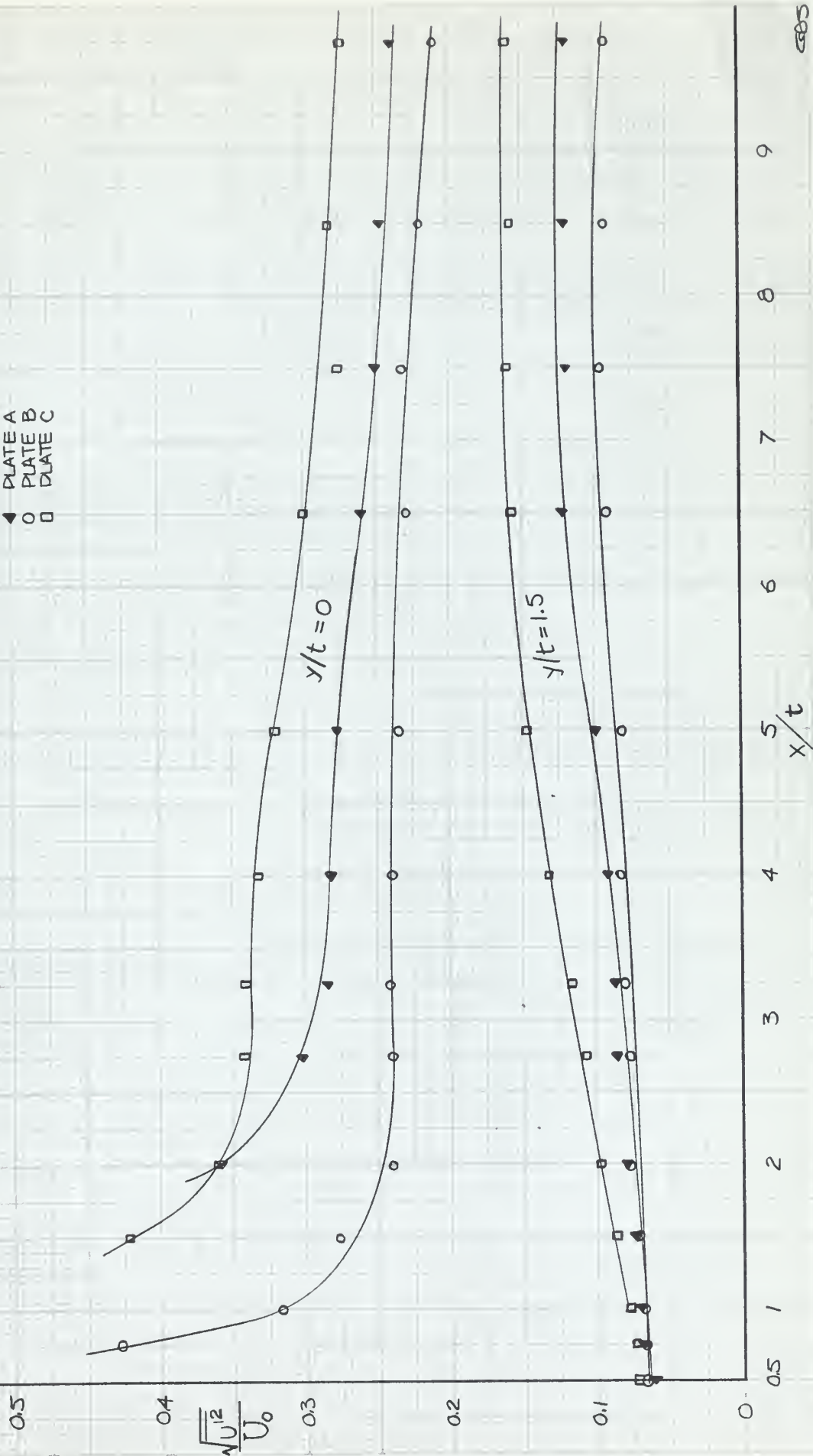
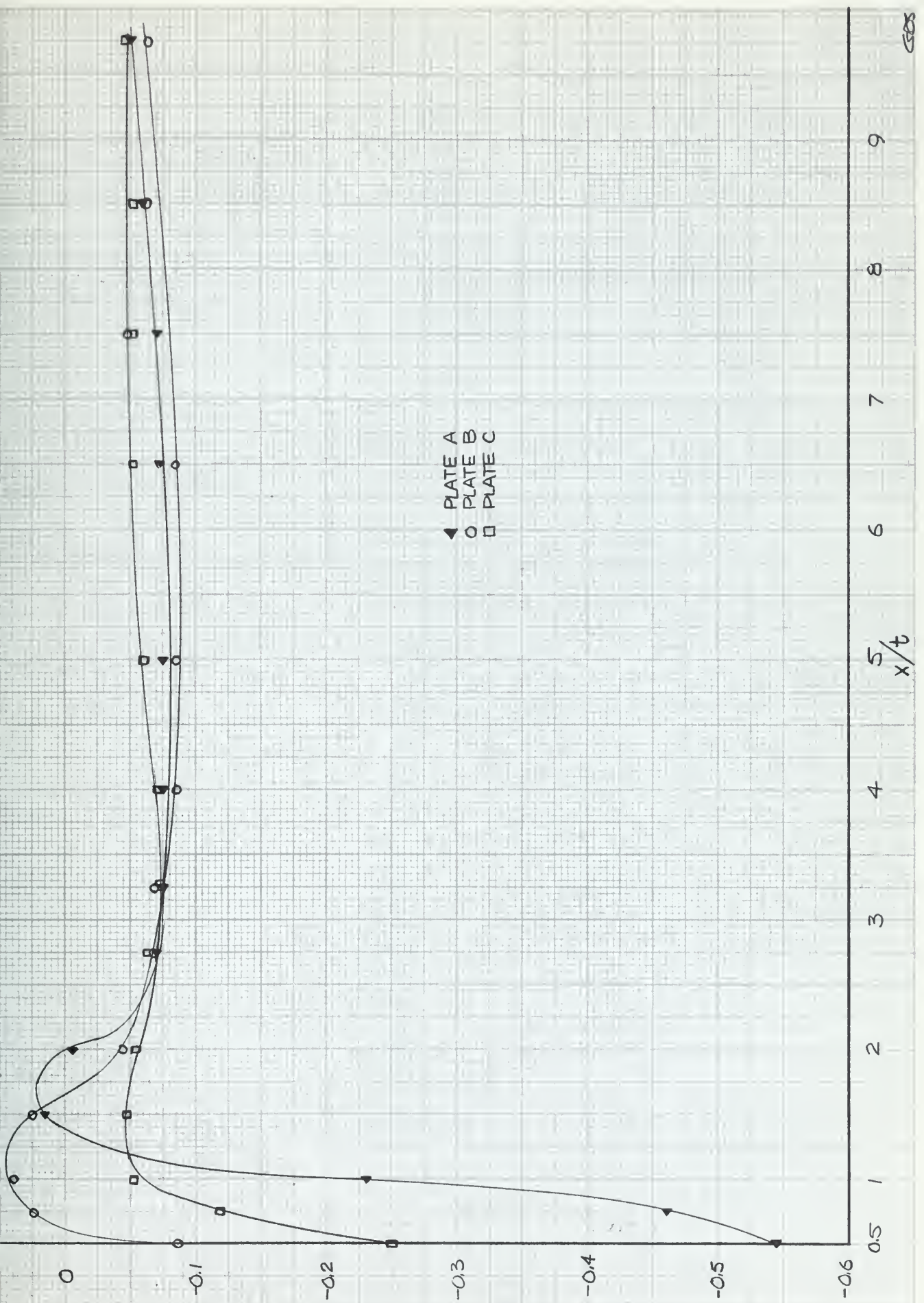
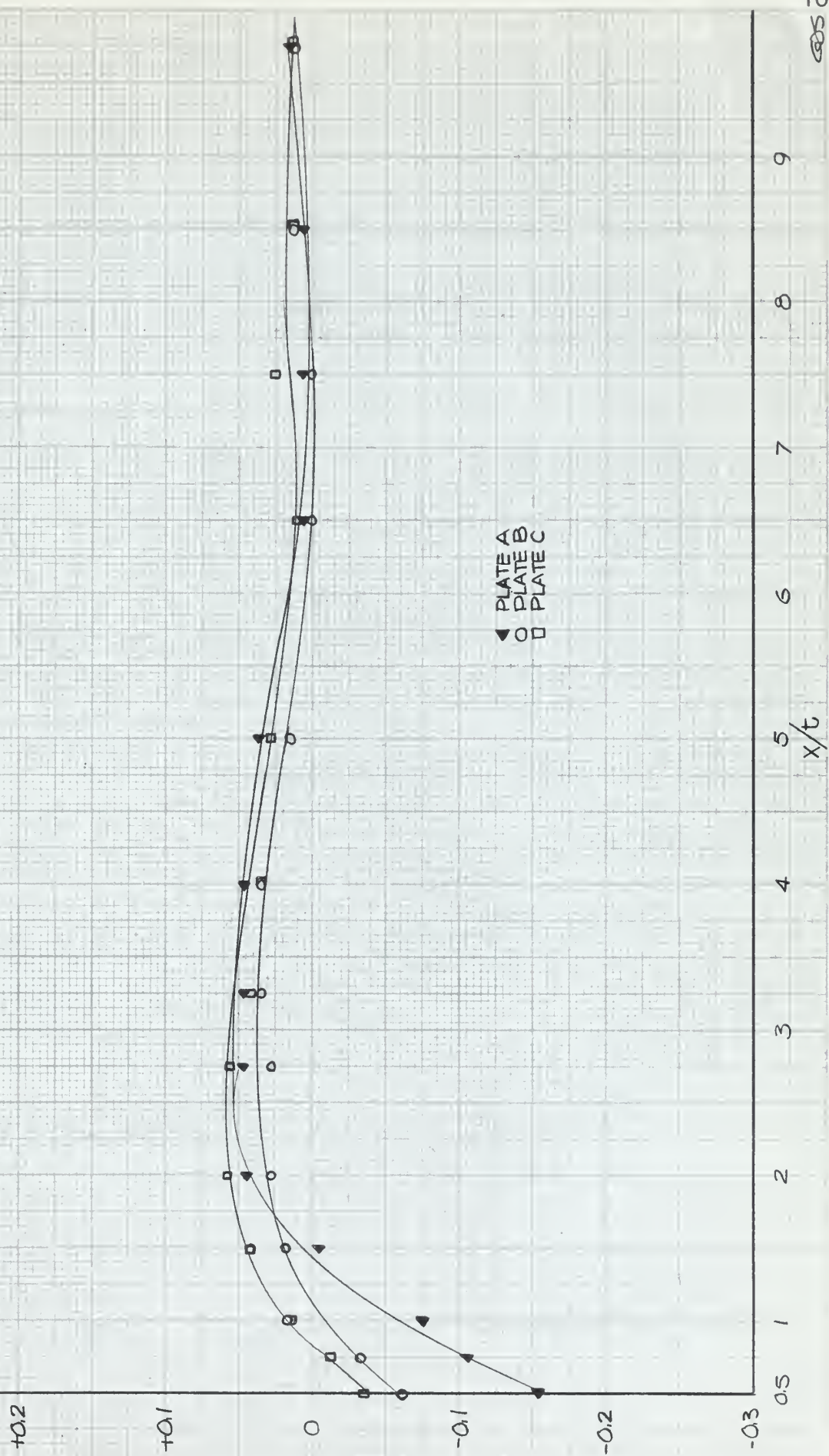


FIGURE B-20 Longitudinal Turbulence Intensity Distribution

FIGURE B-21 Pressure Coefficient Distribution at $y/t = 0$



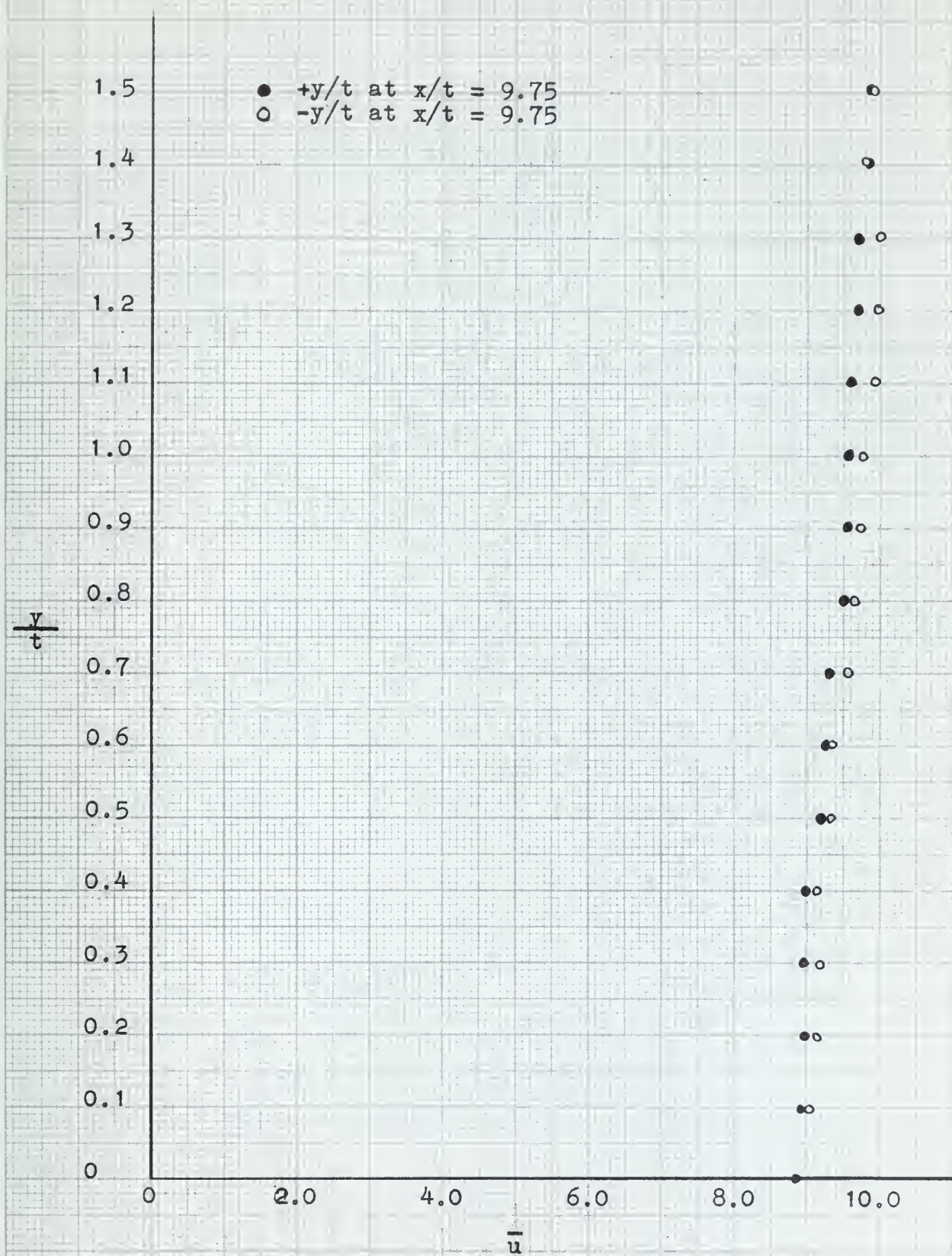


FIGURE B-23 Wake Symmetry Plot, Plate A

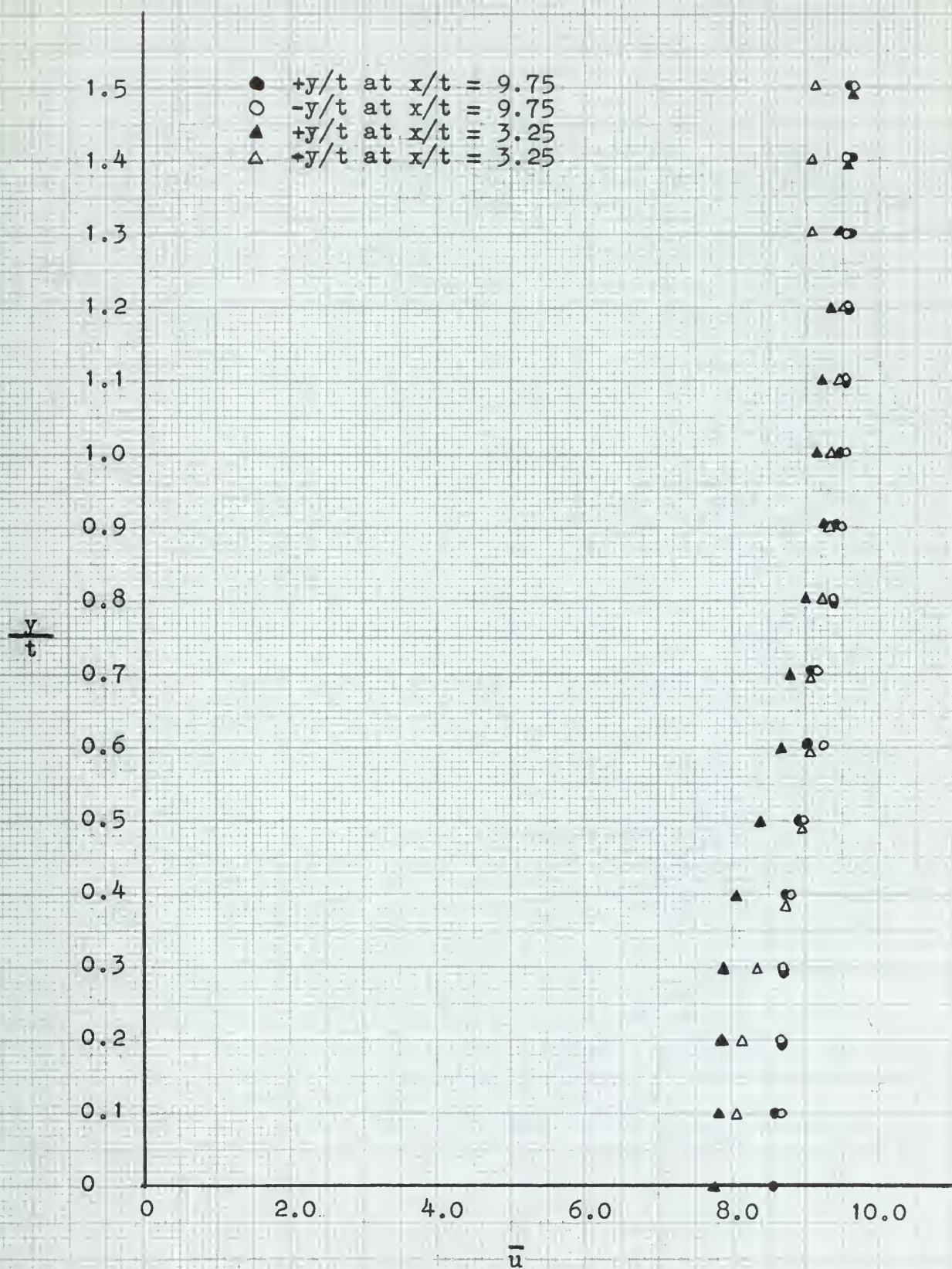


FIGURE B-24 Wake Symmetry Plot, Plate B

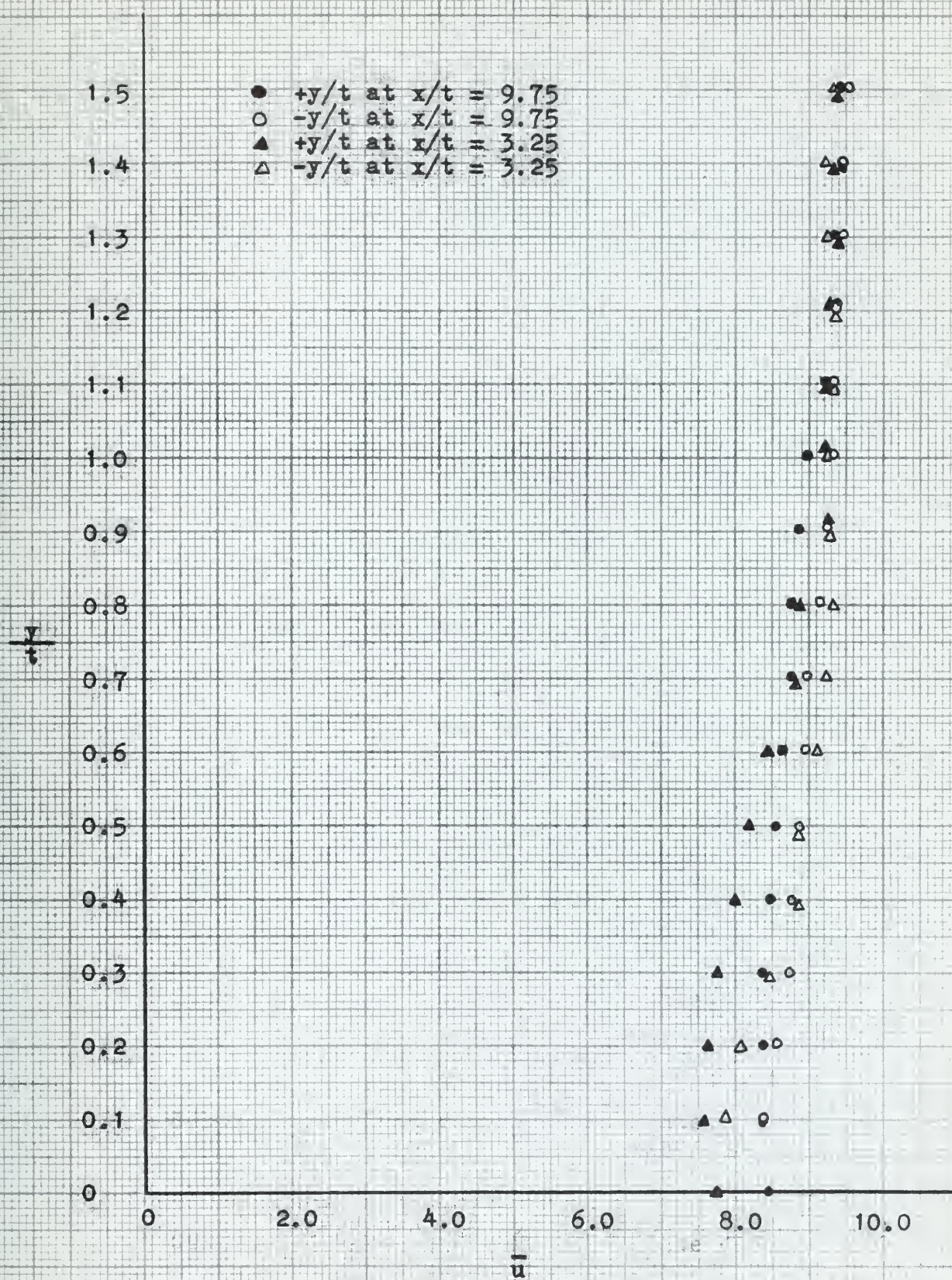


FIGURE B-25 Wake Symmetry Plot, Plate C

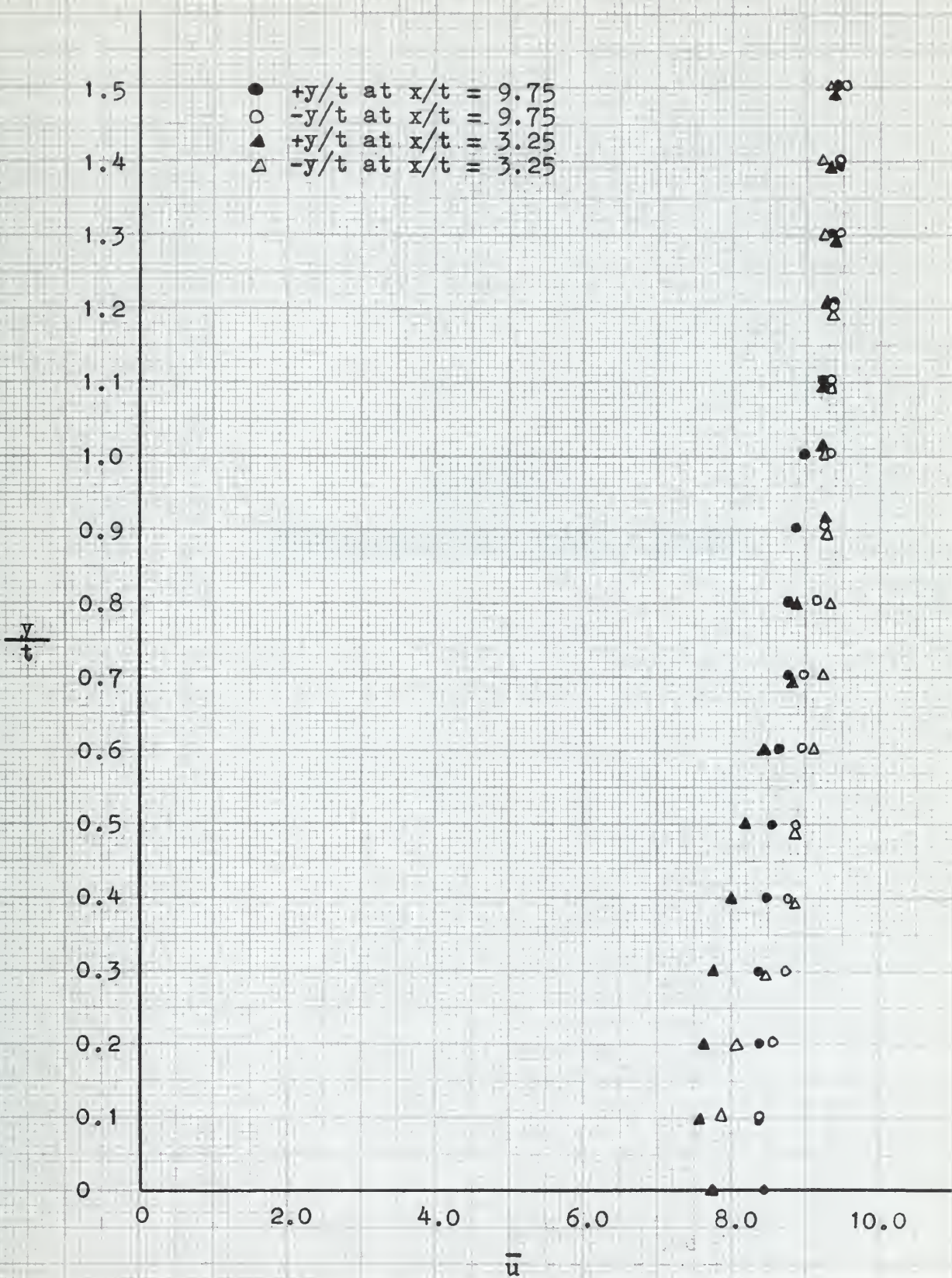


FIGURE B-25 Wake Symmetry Plot, Plate C

APPENDIX C

NORMALIZED ENERGY DENSITY SPECTRA

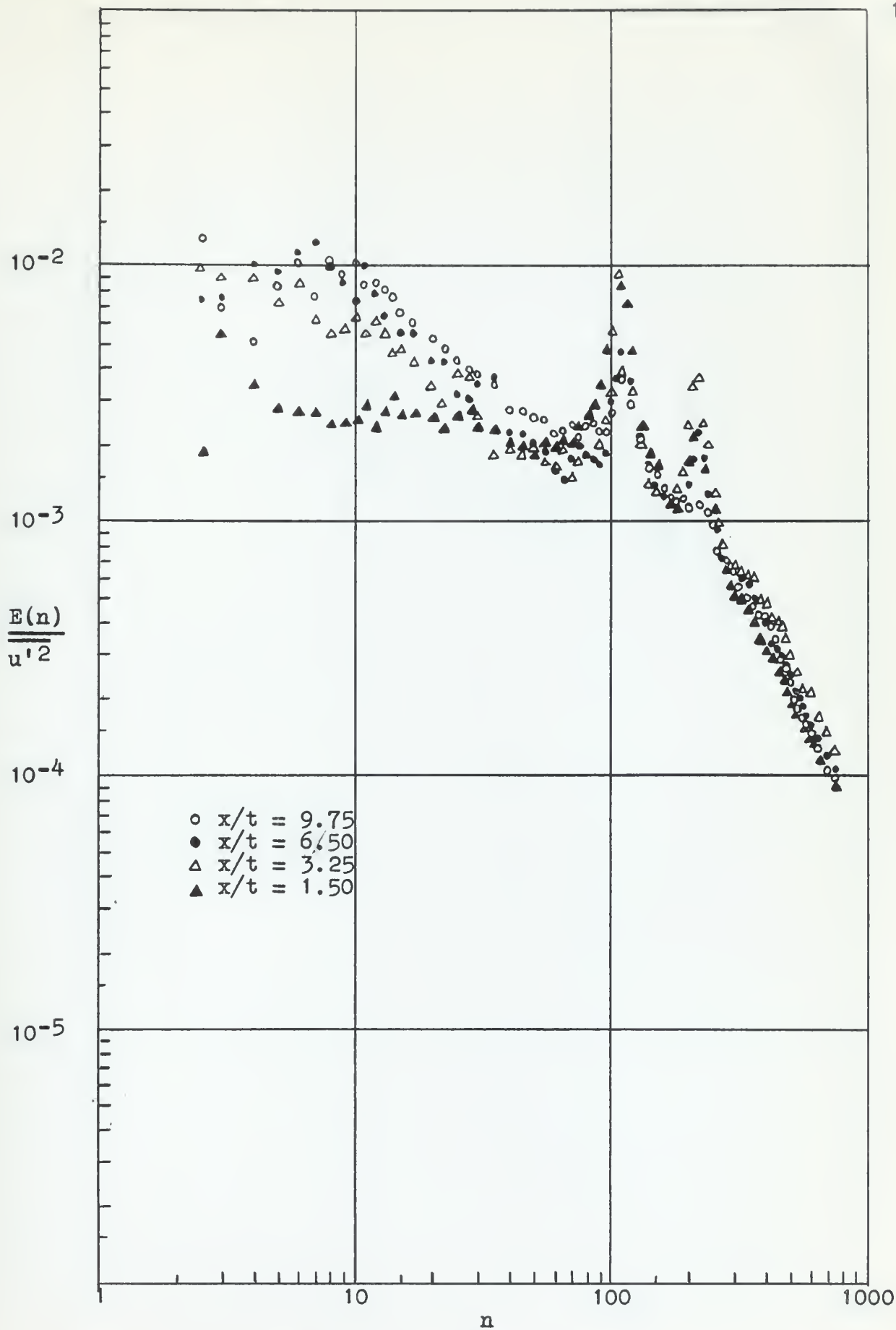
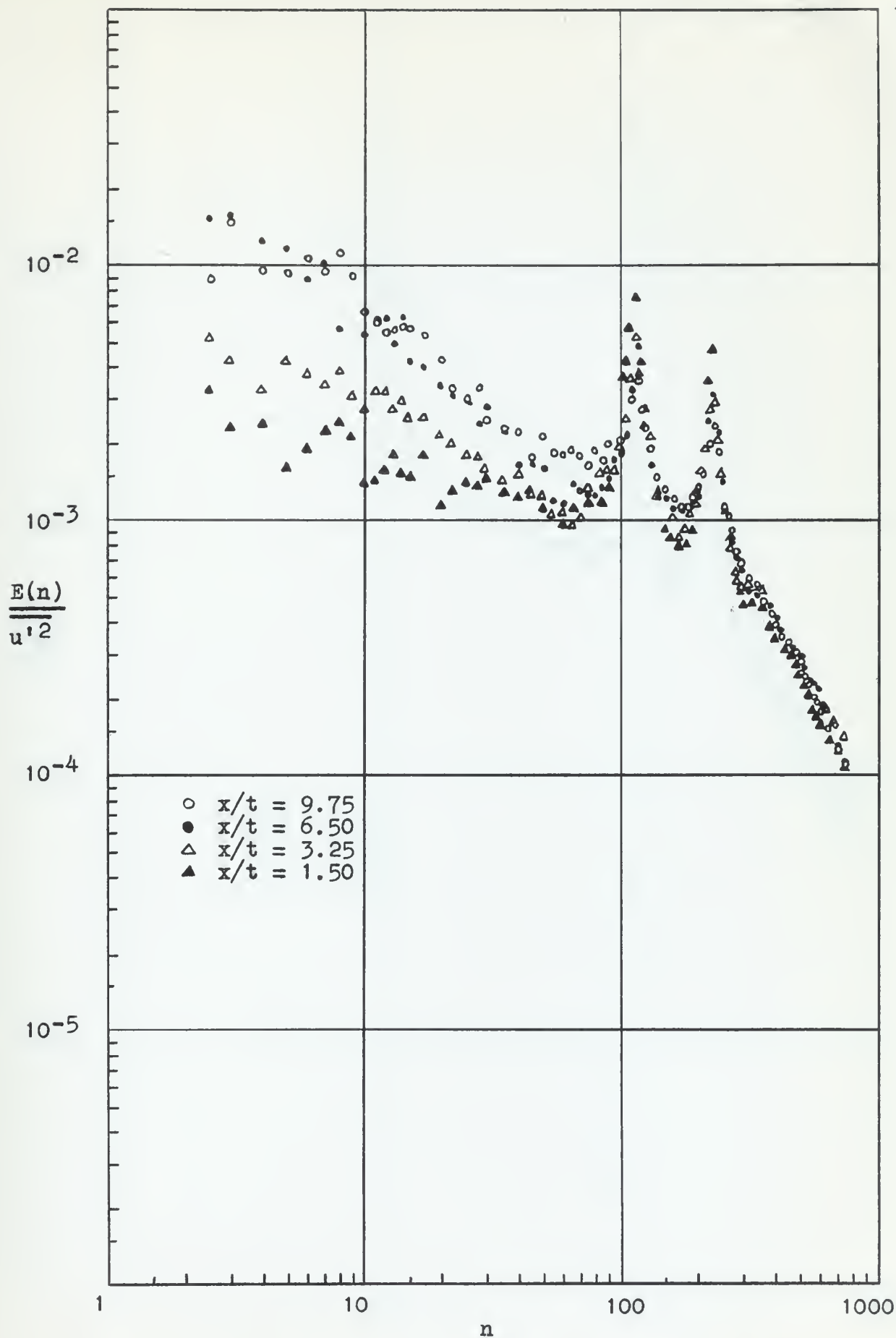
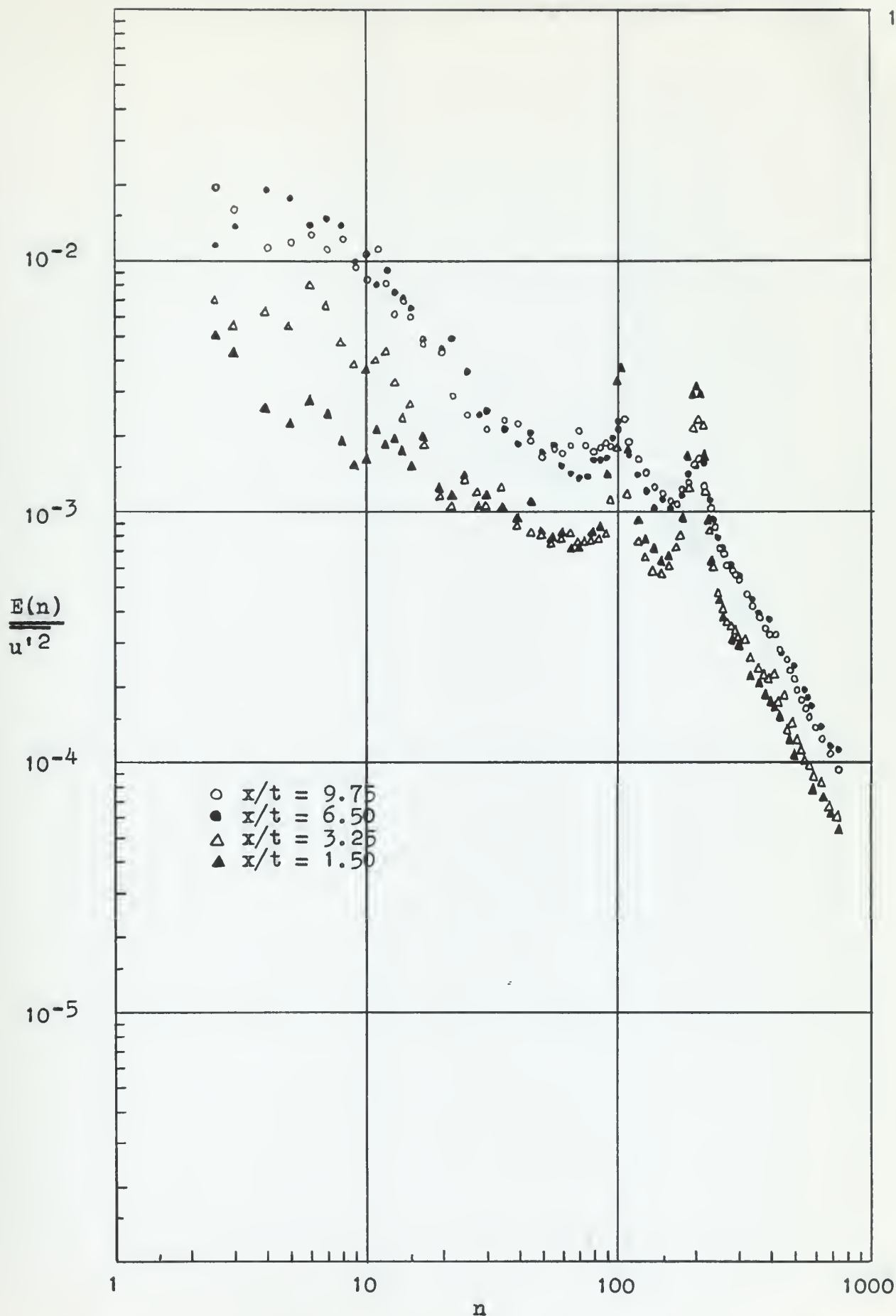
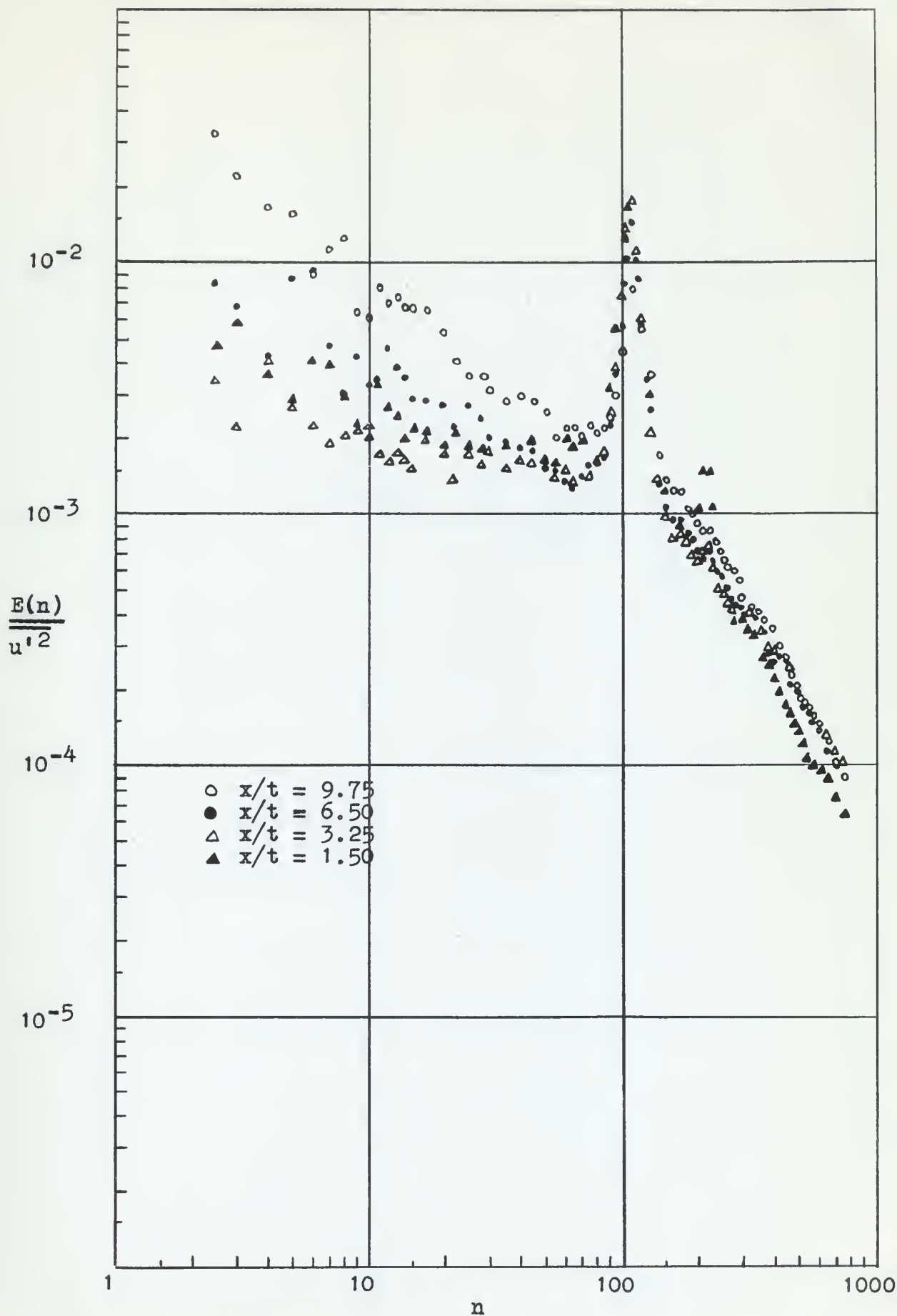
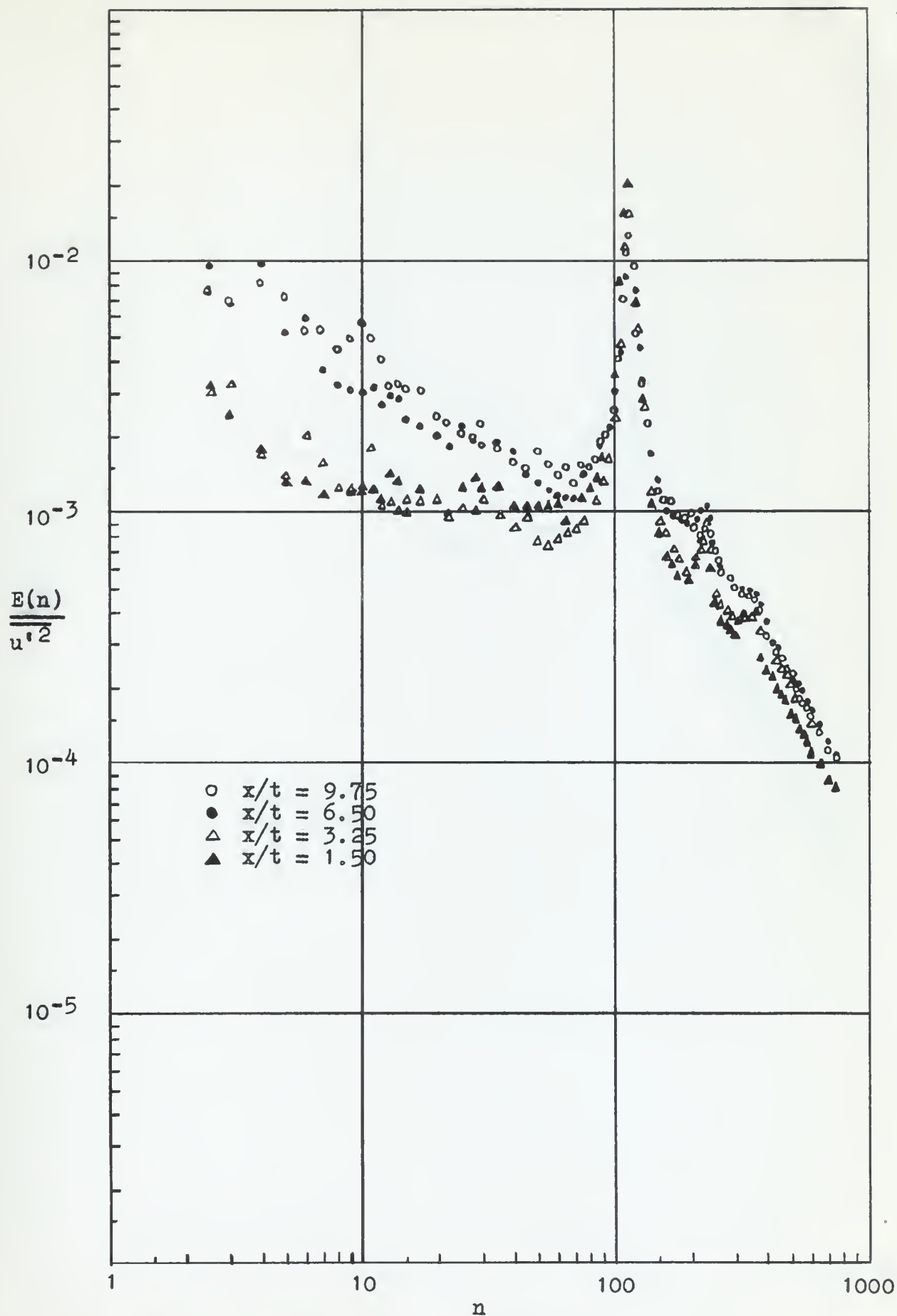


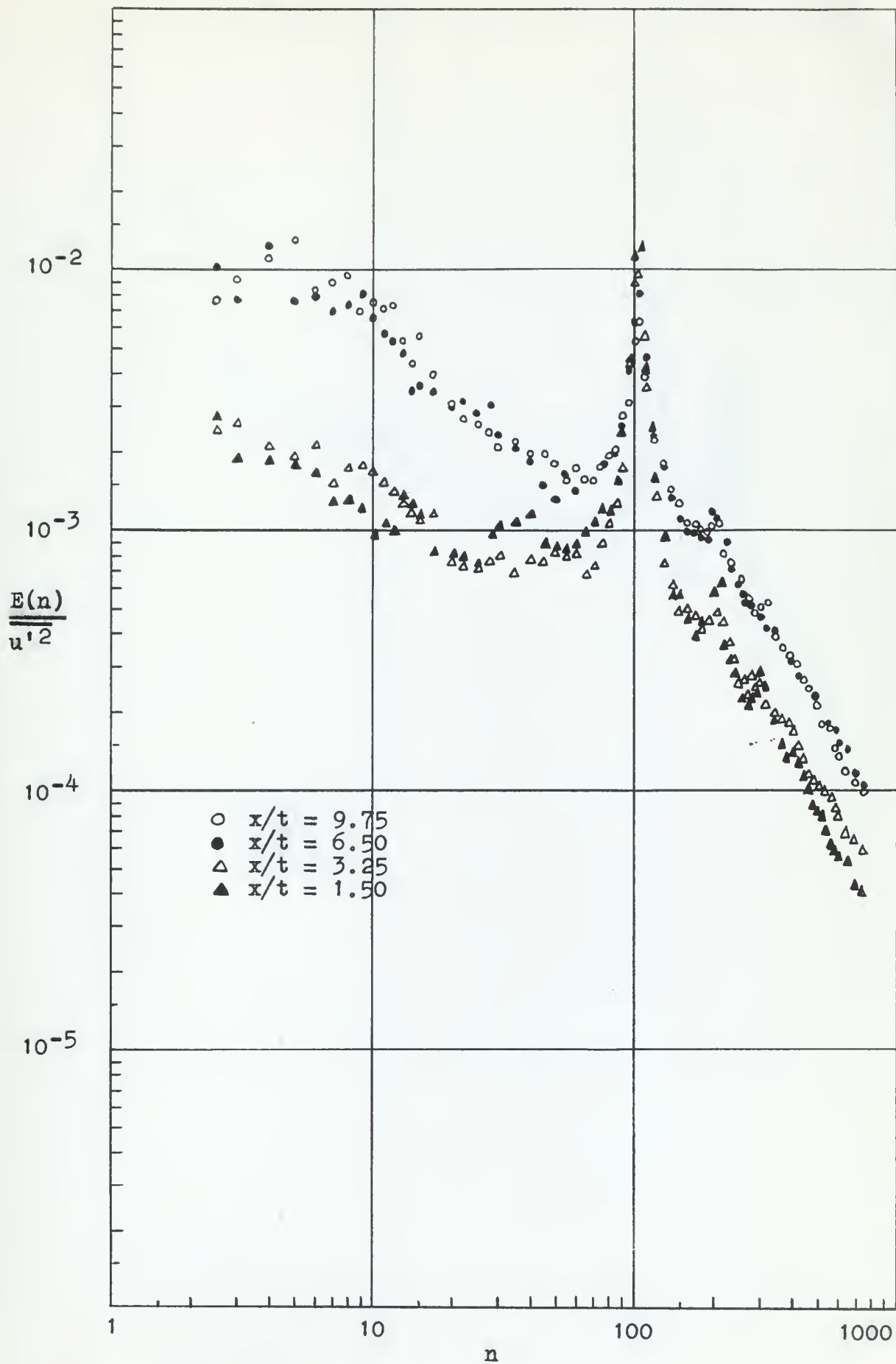
FIGURE C-1 Energy Density Spectra at $y/t = 0$, Plate A

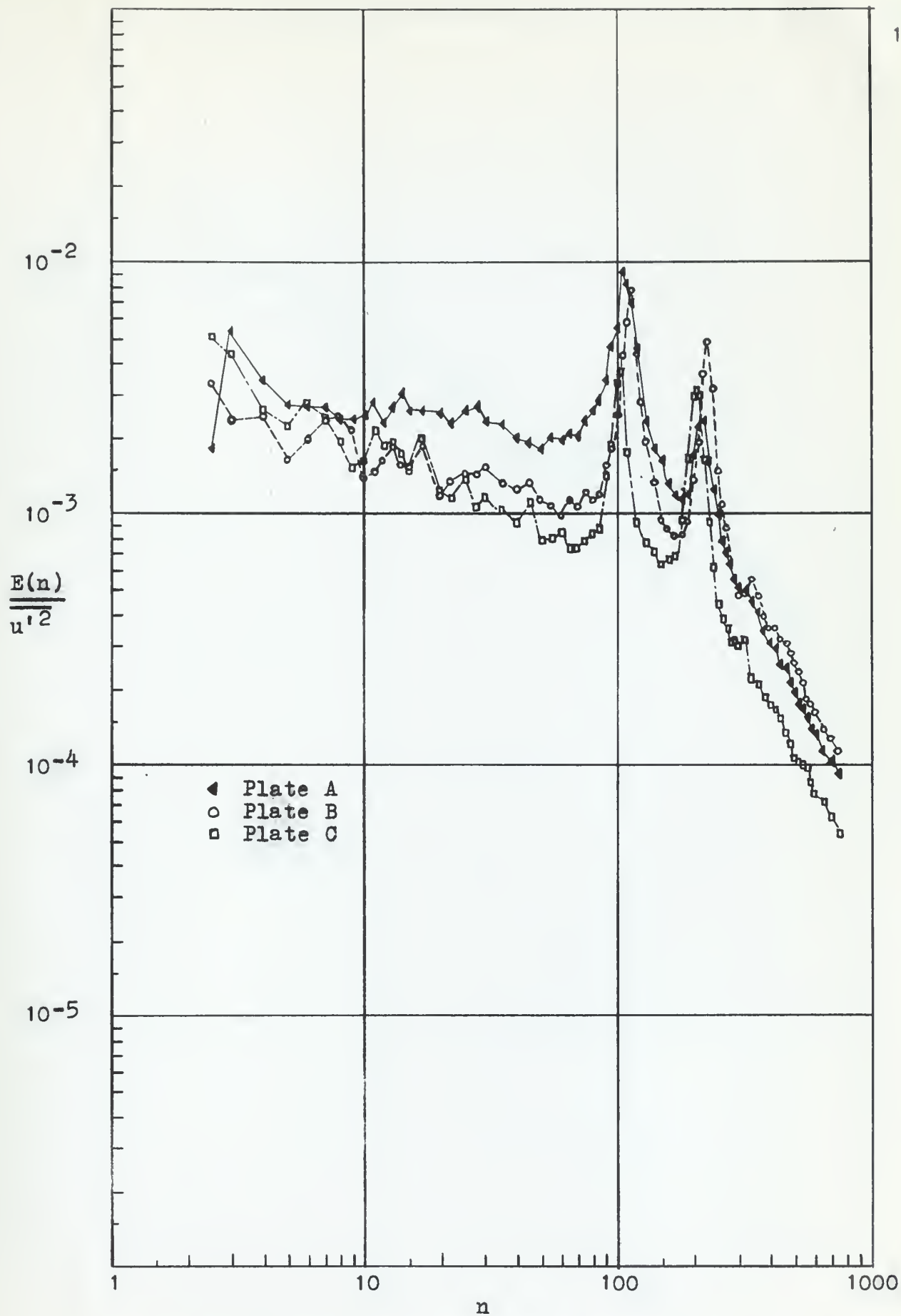
FIGURE C-2 Energy Density Spectra at $y/t = 0$, Plate B

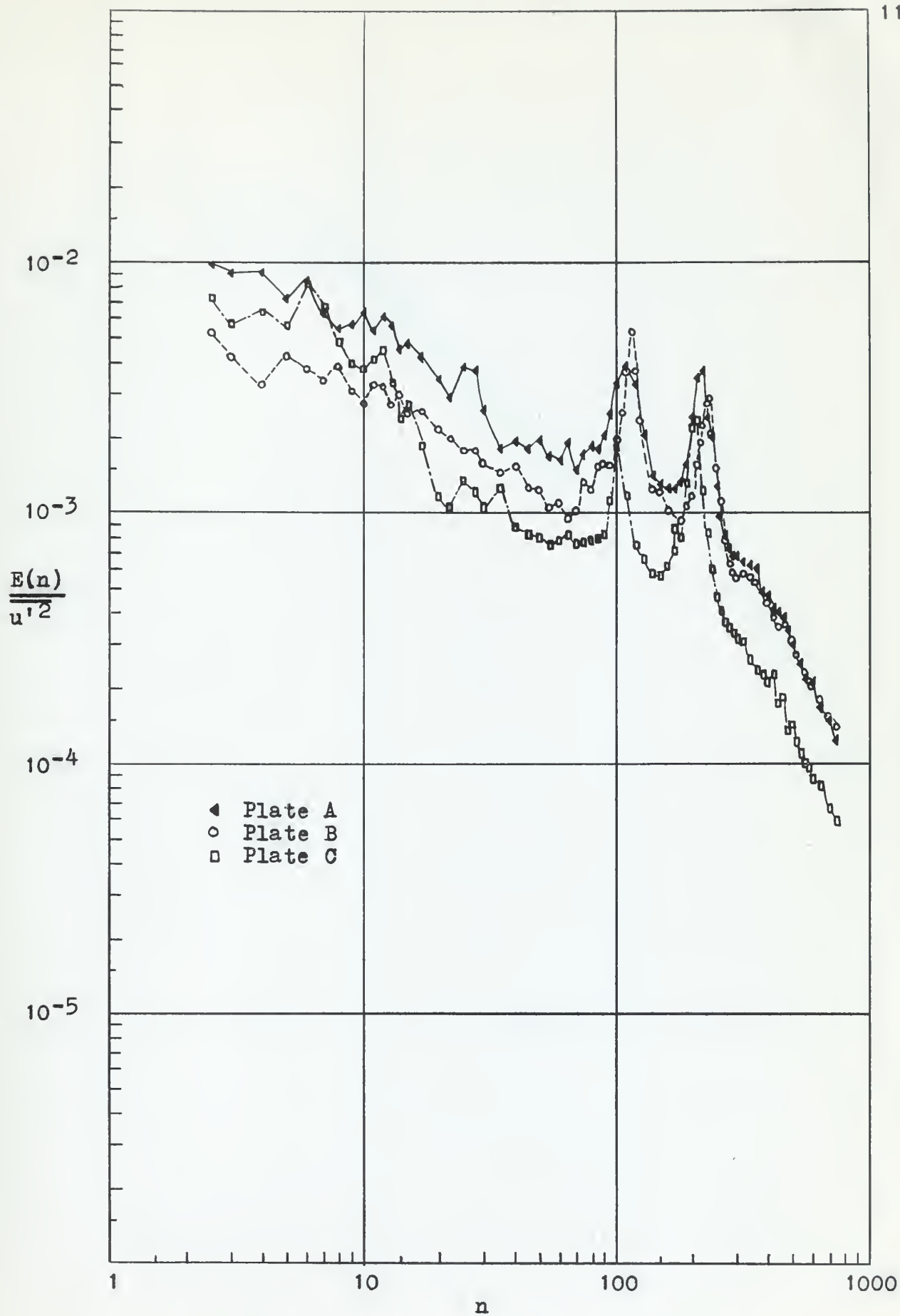
FIGURE C-3 Energy Density Spectra at $y/t = 0$, Plate C

FIGURE C-4 Energy Density Spectra at $y/t = 0.5$, Plate A

FIGURE C-5 Energy Density Spectra at $y/t = 0.5$, Plate B

FIGURE C-6 Energy Density Spectra at $y/t = 0.5$, Plate C

FIGURE C-7 Energy Density Spectra at $y/t = 0$, $x/t = 1.50$

FIGURE C-8 Energy Density Spectra at $y/t = 0$, $x/t = 3.25$

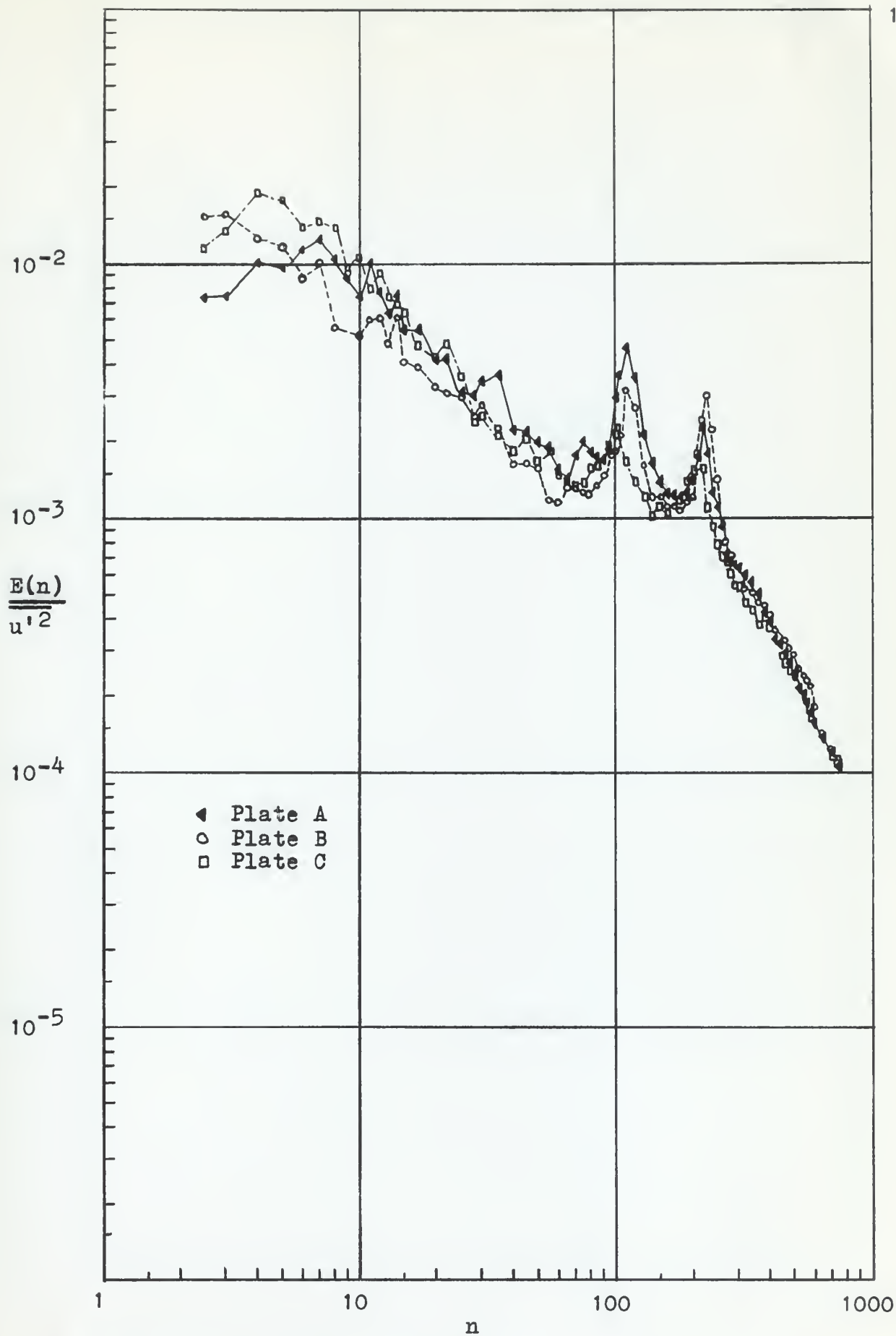


FIGURE C-9 Energy Density Spectra at $y/t = 0$, $x/t = 6.50$

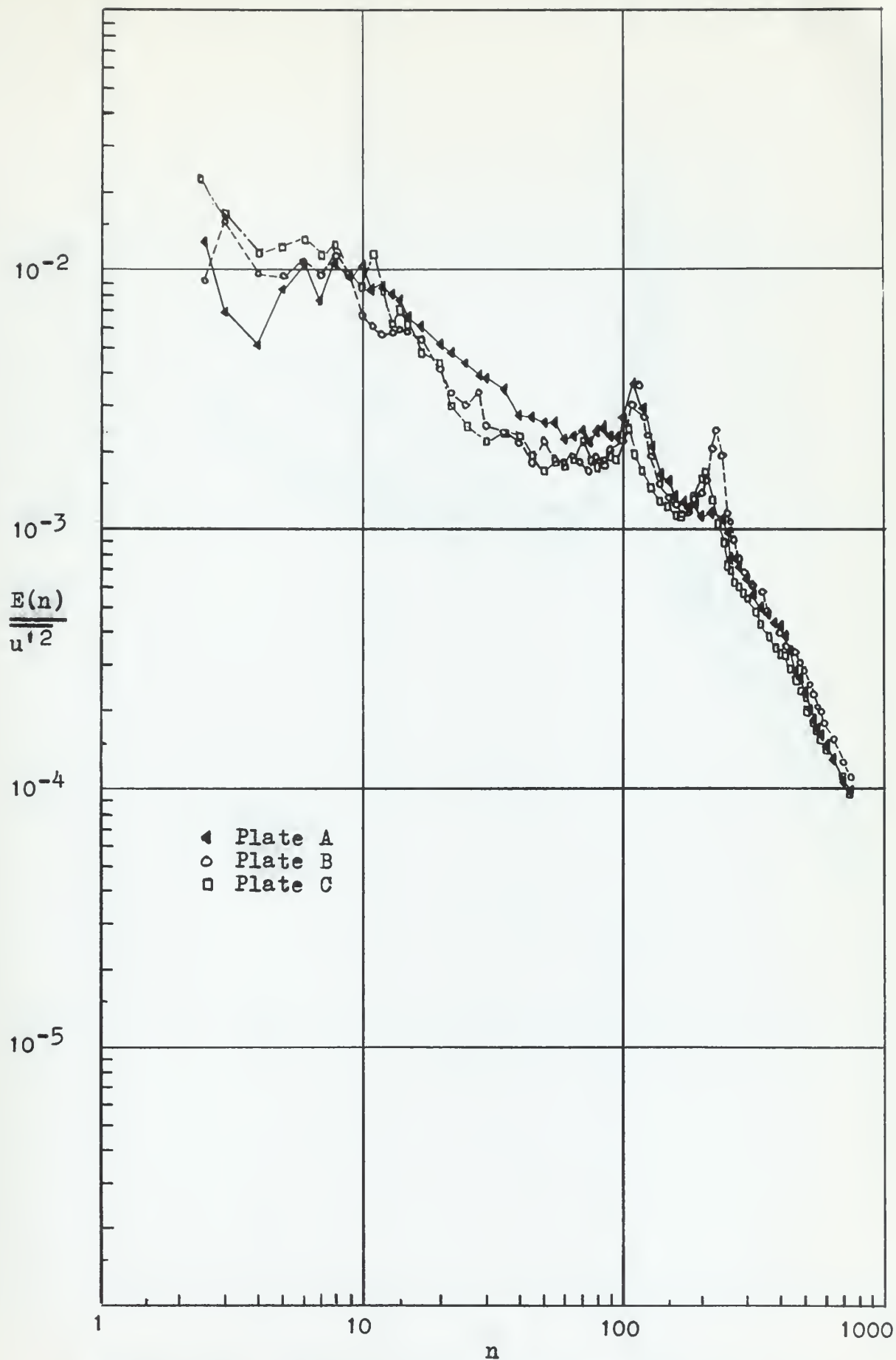
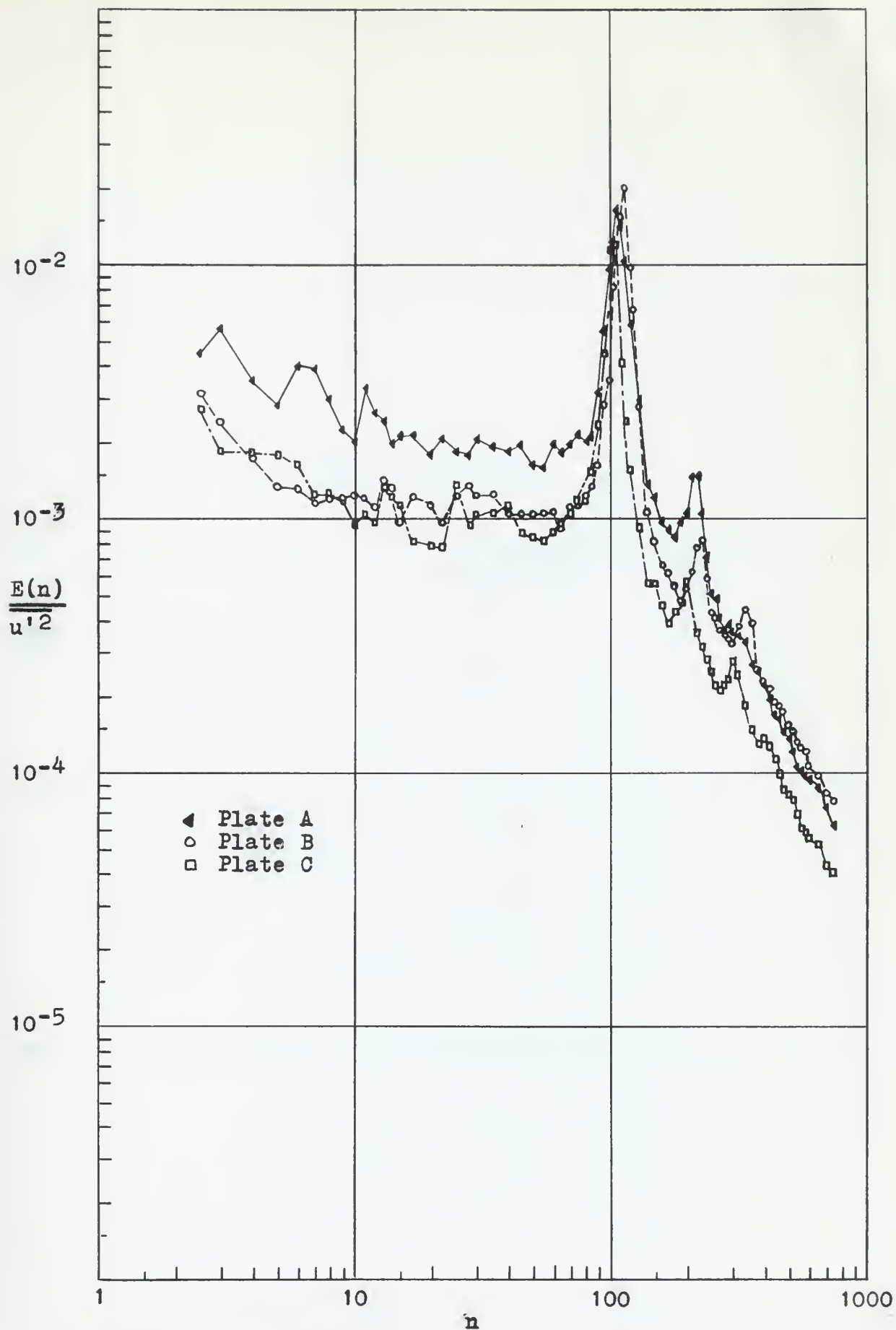
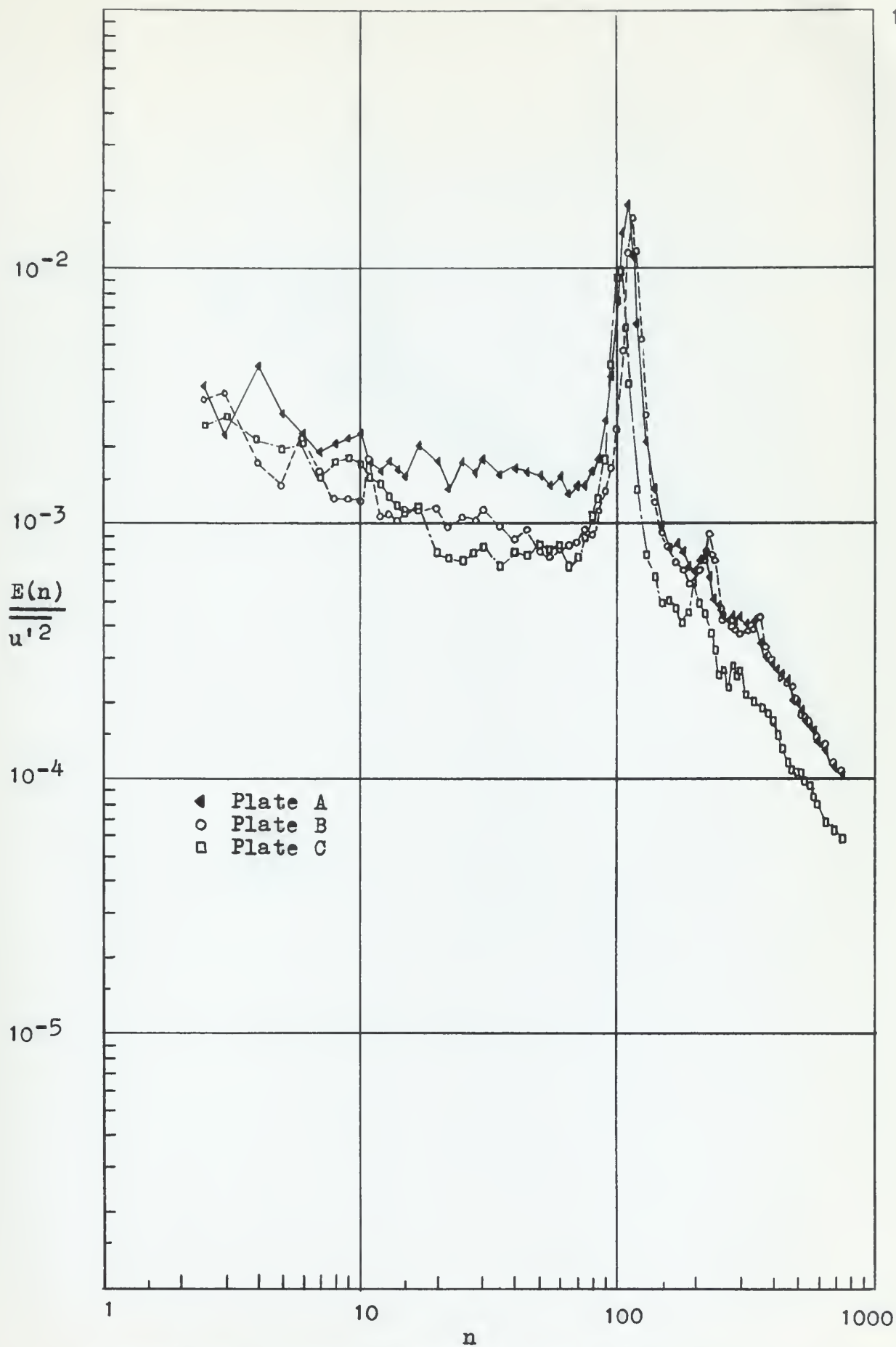


FIGURE C-10 Energy Density Spectra at $y/t = 0$, $x/t = 9.75$

FIGURE C-11 Energy Density Spectra, $y/t = 0.5$, $x/t = 1.50$

FIGURE C-12 Energy Density Spectra, $y/t = 0.5$, $x/t = 3.25$

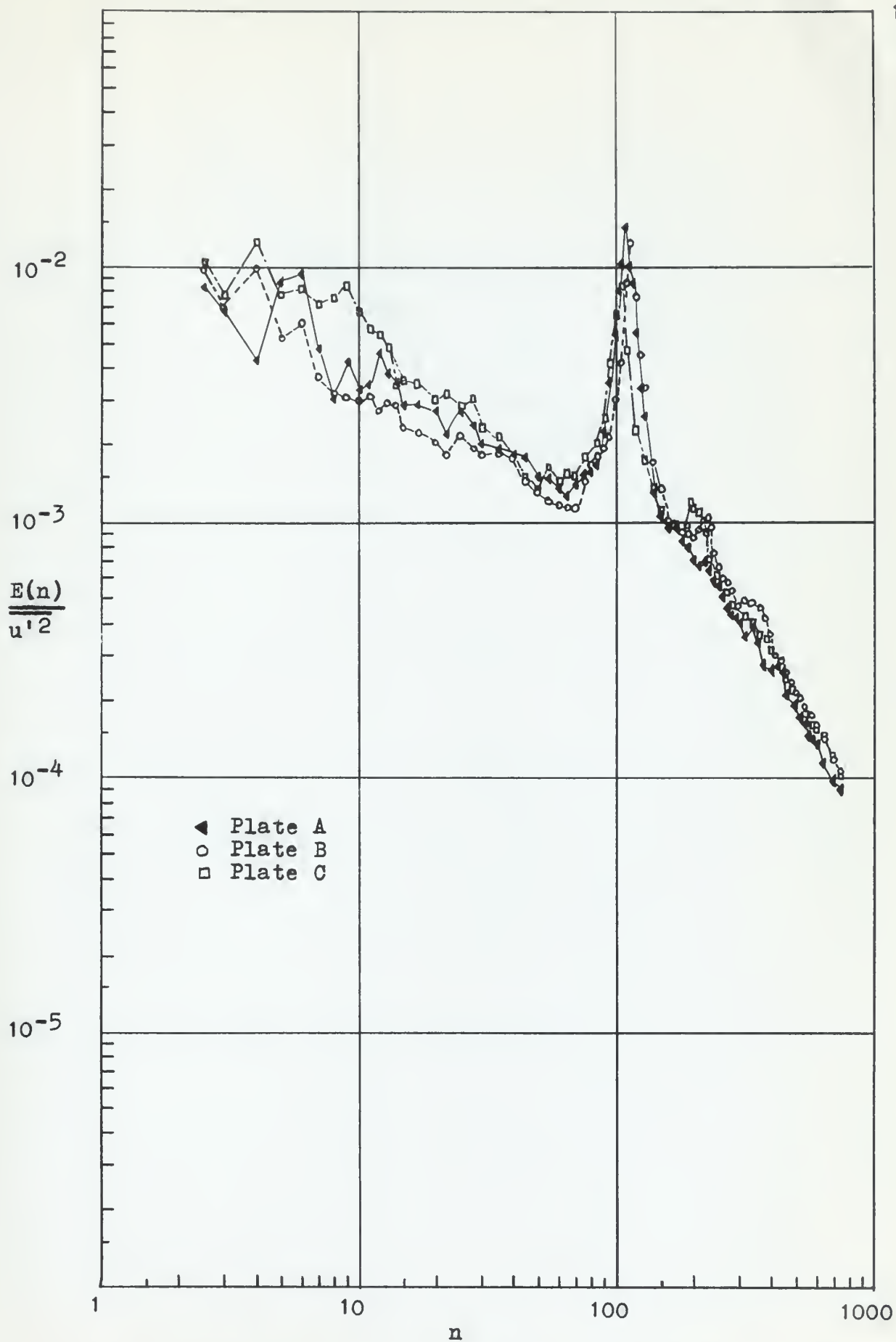


FIGURE C-13 Energy Density Spectra, $y/t = 0.5$, $x/t = 6.50$

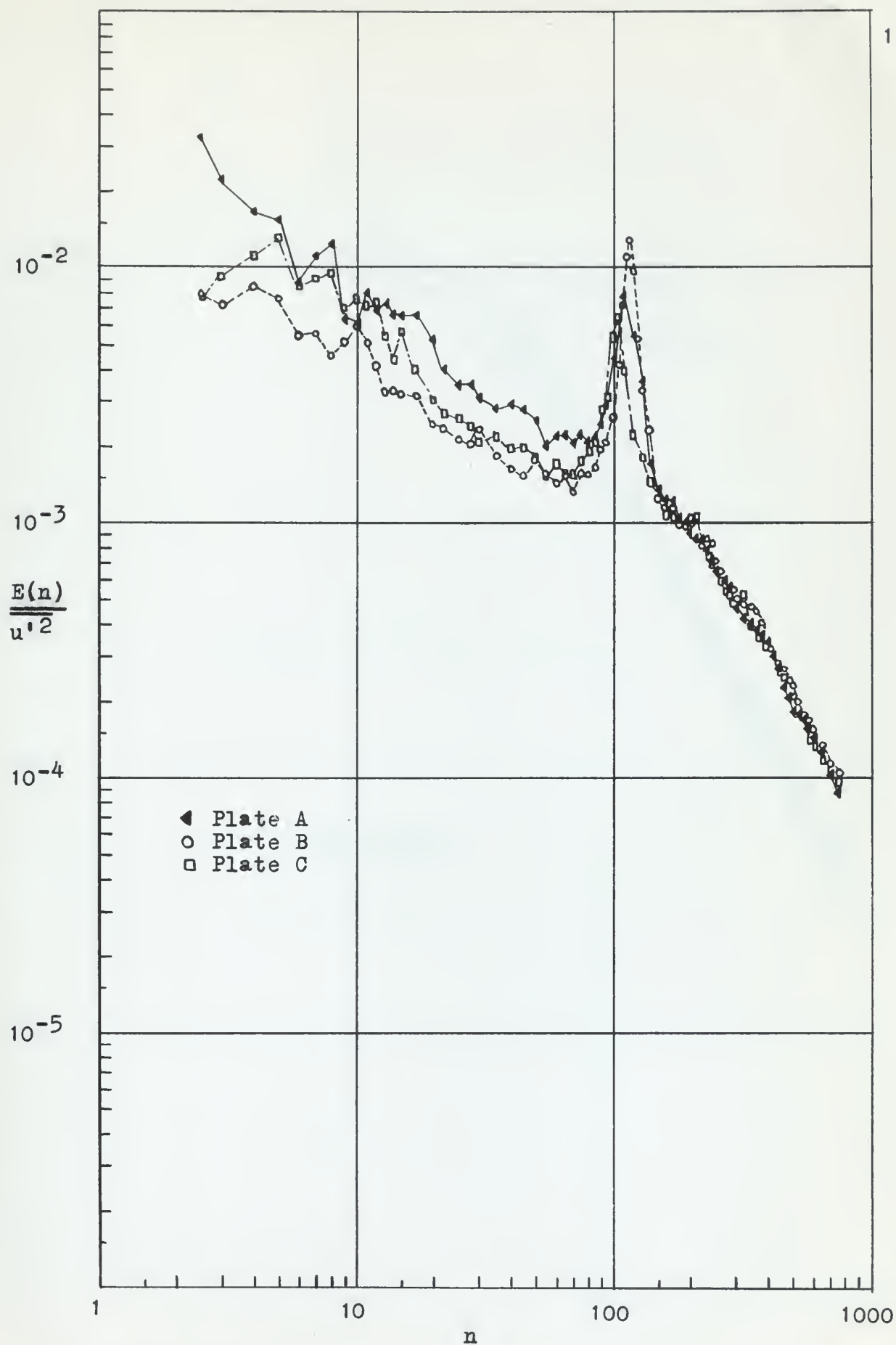


FIGURE C-14 Energy Density Spectra, $y/t = 0.5$, $x/t = 9.75$

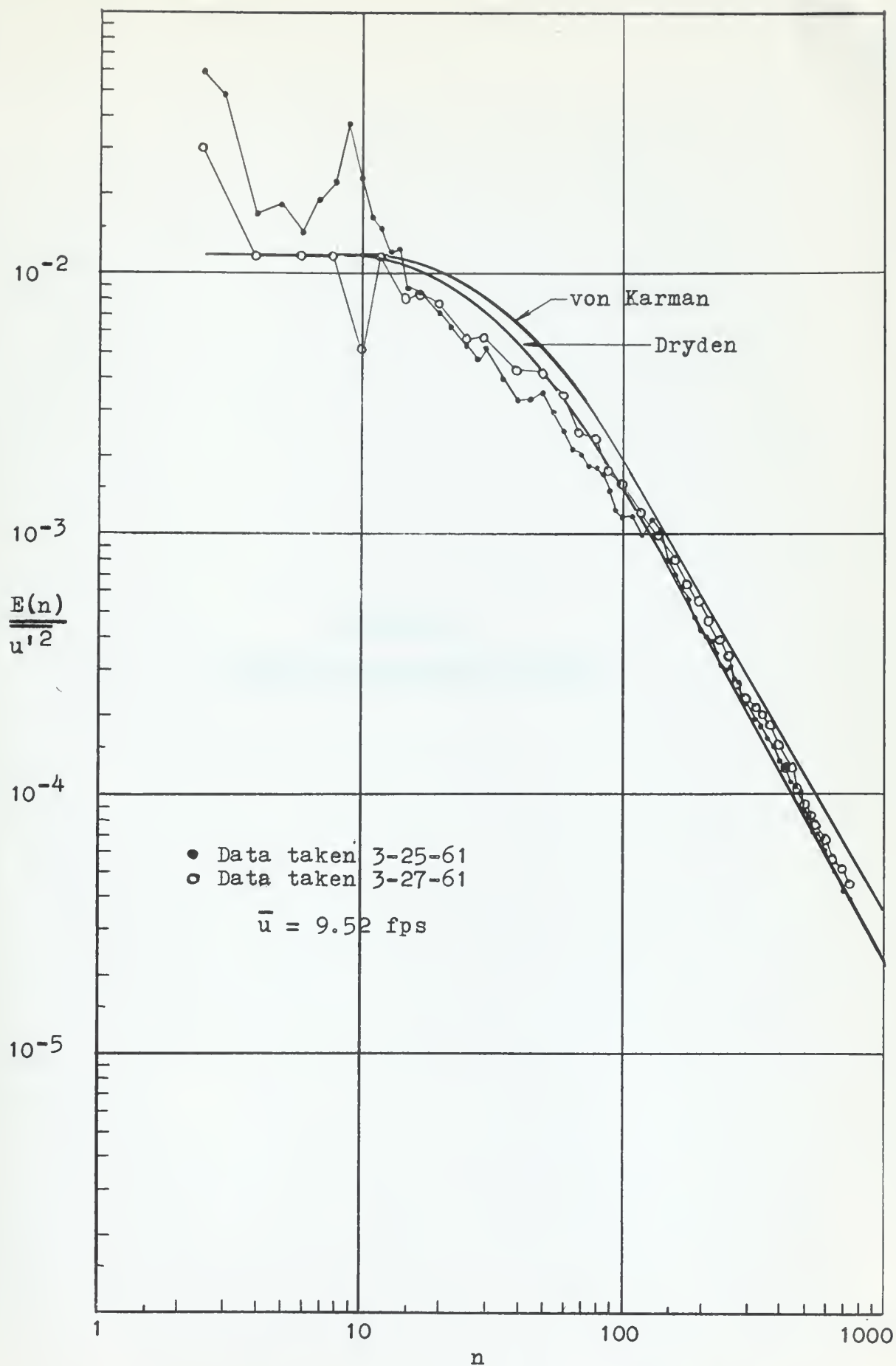


FIGURE C-15 Energy Density Spectrum, Empty Test Section

APPENDIX D
HELMHOLTZ RESONANCE EFFECTS

1. Plate Spindle Cavities.

During measurements incident to determination of the characteristics of the ambient tunnel turbulence spectrum a possible Helmholtz resonance effect was observed. With the desired flow established, the amplified turbulence intensity voltage was observed to be 40 mv rms. Monitoring the entire available spectrum with the vibration analyzer showed no significant peaks. The test plate had been removed from the tunnel test section; no plugs had been placed in either of the spindle cavities.

After several minutes the turbulence voltage level began to rise, reaching approximately 90 mv rms, and a discrete quantity of energy was observed with the vibration analyzer at about 40 cps. The remainder of the spectrum indicated an essentially constant level, down about 6 db from the peak reading. The rms voltage level gradually increased and the peak frequency was gradually noted to decrease, reaching as low as 33 cps.

At this point a large accumulation of air bubbles was noted in the upper spindle cavity under the top cover plate. The vent was opened, and as the bubbles vented off, the rms voltage level decreased to about 40 mv and the discrete peak disappeared.

This phenomenon indicated the possibility of Helmholtz resonance to the authors. Clearly only the air bubbles were causing the low frequency energy, but even a water-filled cavity might be expected to resonate and contribute energy to the flow. Even with the test plate installed and the mounting

spindles passing through the upper and lower tunnel walls, cavities of complicated geometry exist. See Fig. D-1 below.

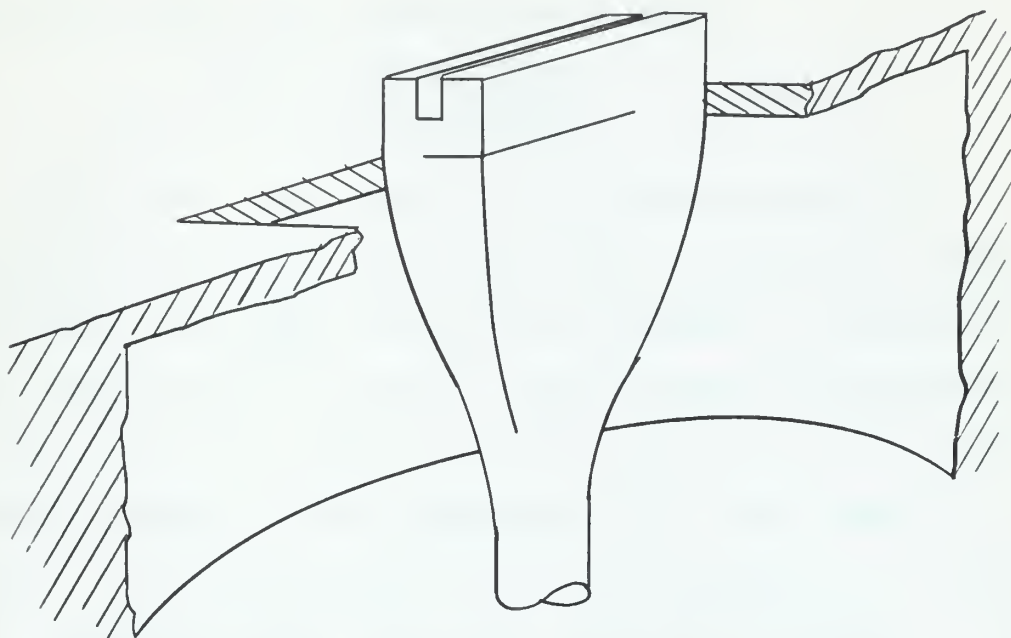


FIGURE D-1. Sketch of Spindle Cavity

The fundamental resonant frequency of a Helmholtz type cavity can be estimated^[33] using the electrical analogy of a simple tank circuit. For a cavity whose dimensions are known:

- S = surface area of the cavity opening,
- V = volume of the cavity,
- l_e = effective length of the "neck" of the cavity, approximated by actual length + $0.8\sqrt{S}$, and
- c = sonic velocity in the medium, taken as 4794 fps in fresh water, uncorrected for rigidity of cavity "neck."

Then the Helmholtz resonant frequency, n_H , is approximated by:

$$n_H = \frac{1}{2\pi} \sqrt{\frac{c^2 S}{l_e V}} \quad (D-1)$$

and in this case from actual measurements:

$$n_H = \frac{4794}{2\pi} \sqrt{\frac{(1.23)(144)}{(1.01)(14.62)}} = 2650 \text{ cps}$$

It is well known that the theoretically derived frequency is an upper limit and that in general any number of effects can reduce the derived frequency. Furthermore, Morse points out^[33] that the lumped circuit approximation is less valid for acoustical systems than it is for electrical circuits because of the shortness of the wave lengths involved. He notes that Eq. (D-1) is of questionable validity for frequencies above 1,000 cps, for when a system is longer than a half wave length it begins to behave like a transmission line and the wave equations become involved.

2. The Turbulence Probe Tip as a Helmholtz Resonator.

The above discussion led naturally to a consideration of the turbulence probe tip as a Helmholtz resonator. From the interior dimensions of the probe tip as cited in Reference (13), and using Eq. (D-1), it was found that for the turbulence probe tip:

$$n_H \approx 7060 \text{ cps}$$

It is considered probable that signals above this frequency will be attenuated at the rate of approximately 20 db per decade.

APPENDIX E
REPRESENTATIVE SAMPLES OF DATA

SAMPLE WAKE SURVEY DATAPLATE C, $x/t = 9.75$ DATE: 3-28-61AMPLIFIER GAIN: 30CONTRACTION MANOMETER: $\Delta h_M = 21.30$, $\Delta h_{Hg} = 1.27$

VALVE INDICATORS - FOOT VALVE: 1.9
PUMP DISCHARGE: 22.5
CIRCUIT STOP: 12.5

y/t	TURBULENCE VOLTAGE (RMS)		TOTAL HEAD		STATIC HEAD	
	Thermocouple	Ballantine	Pressure Side	Atmos. Side	Pressure Side	Atmos. Side
	mv	mv	"Hg	"Hg	"Hg	"Hg
+1.5	110	93	20.73	25.86	20.55	24.47
+1.4	115	102	20.74	25.85	20.56	24.47
+1.3	120	105	20.75	25.84	20.56	24.46
+1.2	125	110	20.76	25.84	20.56	24.46
+1.1	135	122	20.78	25.82	20.57	24.45
+1.0	139	127	20.80	25.77	20.57	24.45
+0.9	145	130	20.82	25.75	20.57	24.45
+0.8	151	132	20.83	25.74	20.57	24.45
+0.7	153	136	20.84	25.73	20.58	24.44
+0.6	156	138	20.86	25.72	20.58	24.44
+0.5	157	138	20.87	25.71	20.58	24.44
+0.4	155	142	20.88	25.70	20.58	24.44
+0.3	155	141	20.90	25.68	20.59	24.43
+0.2	157	143	20.90	25.68	20.59	24.43
+0.1	154	142	20.90	25.68	20.59	24.43
0	150	138	20.90	25.68	20.60	24.42
-0.1	155	143	20.90	25.68	20.59	24.43
-0.2	157	145	20.88	25.70	20.59	24.43
-0.3	154	140	20.86	25.73	20.59	24.43
-0.4	149	142	20.86	25.73	20.59	24.43
-0.5	149	139	20.82	25.76	20.57	24.45
-0.6	150	138	20.80	25.78	20.56	24.46
-0.7	147	132	20.80	25.78	20.56	24.46
-0.8	142	130	20.77	25.81	20.56	24.47
-0.9	135	123	20.76	25.83	20.56	24.47
-1.0	133	123	20.75	25.84	20.56	24.47
-1.1	122	110	20.74	25.85	20.55	24.47
-1.2	117	103	20.74	25.85	20.55	24.47
-1.3	115	95	20.73	25.86	20.55	24.47
-1.4	100	87	20.72	25.86	20.55	24.47
-1.5	97	82	20.72	25.87	20.56	24.48

SAMPLE ENERGY SPECTRUM DATAPLATE C, $x/t = 3.25$, $y/t = 0.5$ DATE: 3-29-61AMPLIFIER GAIN: 20AVERAGE RMS TURBULENCE VOLTAGE - THERMOCOUPLE: 131 mv
BALANTINE: 115 mvANALYZER SENSITIVITY: 10ANALYZER SELECTIVITY: SHARPANALYZER CALIBRATION CONSTANT: 5.31×10^5 volts⁻¹CONTRACTION MANOMETER: $\Delta h_M = 21.35$, $\Delta h_{Hg} = 1.30$ $\Delta h_{total} = 25.62 - 20.95$ $\Delta h_{static} = 24.36 - 20.66$

<u>FREQUENCY</u> <u>(cps)</u> <u>n</u>	<u>ANALYZER</u> <u>READING</u> <u>Rd</u>	<u>FREQUENCY</u> <u>(cps)</u> <u>n</u>	<u>ANALYZER</u> <u>READING</u> <u>Rd</u>	<u>FREQUENCY</u> <u>(cps)</u> <u>n</u>	<u>ANALYZER</u> <u>READING</u> <u>Rd</u>
2.5	7.5	70	22	230	28
3	9.4	75	25	240	26
4	8.9	80	28	250	24
5	9.5	85	31	260	25
6	11.0	90	38	270	24
7	9.9	95	60	280	27
8	11.7	98	75	290	26
9	12.1	100	92	300	27
10	12.5	102	95	320	25
11	12.6	104	88	340	25
12	12.6	106	75	360	25
13	12.4	108	70	380	25
14	12.4	110	60	400	25
15	12.5	115	45	420	24
17	13.4	120	39	440	23
20	11.8	130	30	460	22
22	12.2	140	28	480	22
25	12.8	150	26	500	22
28	14.0	160	27	520	22
30	14.8	170	27	540	22
35	14.8	180	26	560	22
40	17.0	190	28	580	21
45	17.8	195	30	600	21
50	19.6	200	33	650	20
55	20	205	32	700	20
60	21	210	31	750	20
65	20	220	30		

NOTE: Analyzer readings from $n = 2.5$ through $n = 50$ are time averages of a number of individual readings taken at fixed time increments in an attempt to smooth out data scatter.

APPENDIX F
REFERENCES

REFERENCES

- (1) Work, C.E., "Review of Marine Propeller Noise and Vibration Studies," U.S. Nav. Ord. Test Sta. Propulsion Memo 74, 7 September 1940.
- (2) Gutsche, F., "Das Singen von Schiffsschrauben," Zeit. des Ver. Deutsch. Ing., 3 July 1937, Vol. 81, pp. 882-883; TMB Trans. 123.
- (3) Hunter, H., "Singing Propellers," N.E.C.I.E.S., 1937-38, Vol. 53, 189-222, D73-D120.
- (4) Kerr, W., Shannon, J.F., and Arnold, R.N., "The Problems of the Singing Propeller," Inst. Mech. Engrs., London, December 1940, Vol. 144, 54-90.
- (5) Hughes, G., "On Singing Propellers," I.N.A., 1945, 185-216.
- (6) Work, C.E., "Singing Propellers," A.S.N.E., May 1951, 319-331.
- (7) Lankester, S.G., and Wallace, W.D., "Some Investigations into Singing Propellers," N.E.C.I.E.S., 7 June 1955, 293-318.
- (8) Gongwer, C.A., "A Study of Vanes Singing in Water," J. Appl. Mech., Vol. 19, No. 4, Dec. 1952, and Aerojet Eng. Corp. Res. Tech. Memo 76 ONR N6or1, 3 May 1951.
- (9) Saunders, H.E., Hydrodynamics in Ship Design, Vol. I, S.N.A.M.E., New York, 1957.
- (10) Jewell, D.A., "A Note on Hydroelasticity," J. of Ship Research, Vol. 3, No. 4, March 1960.
- (11) Abramson, H.N., and Chu, W., "A Discussion of the Flutter of Submerged Hydrofoils," J. of Ship Research, Vol. 3, No. 2, October 1959.
- (12) Den Hartog, J.P., Mechanical Vibrations, McGraw-Hill, New York, 1947.
- (13) Huval, C.J., "The Early Wake of a Fixed, Flat Plate," S.M. Thesis, M.I.T., 1 January 1961.
- (14) Ippen, A.T., Toebe, G.H., and Eagleson, P.S., "The Hydroelastic Behavior of Flat Plates as Influenced by Trailing Edge Geometry," M.I.T. Hydro. Lab. T.R. No. 36, April 1960.
- (15) Krivtsov, Y.V., and Pernik, A.J., "The Singing of Propellers," TMB Trans. 281, 1958.

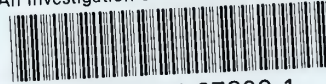
- (16) Rayleigh, Lord, The Theory of Sound, Vol. II, Dover Publications, 1945.
- (17) Kovasznay, J.S.G., "Hot Wire Investigation of the Wake Behind Cylinders at Low Reynolds Numbers," Proc. Royal Soc., London, Vol. 198, No. 1053, 15 August 1949.
- (18) Roshko, A., "On the Development of Turbulent Wakes from Vortex Streets," N.A.C.A Report 1191, 1954.
- (19) Fage, A., and Johansen, F.C., "On the Flow of Air Behind an Inclined Flat Plate of Infinite Span," R. and M. No. 1104, British A.R.C., 1927.
- (20) Betchov, R., "Simplified Analysis of Boundary-Layer Oscillations," J. of Ship Research, Vol. 4, No. 2, November 1960.
- (21) Cooper, R.D., and Iutzky, M., "Exploratory Investigation of the Turbulent Wakes Behind Bluff Bodies," TMB Report 963, October 1955.
- (22) Birkhoff, G., Hydrodynamics, Dover Publications, 1950.
- (23) Schlichting, H., Boundary Layer Theory, McGraw-Hill, 1955.
- (24) Jones, B.M., "The Measurement of Profile Drag by the Pitot Traverse Method," R. and M. No. 1668, British A.R.C., 1936.
- (25) Lamb, Sir Horace, Hydrodynamics, Sixth Edition, Dover Publications, 1945.
- (26) Karman, Th. von, "Über den Mechanismus des Flüssigkeits- und Luftwiderstandes," Phys. Zeit., Vol. 13, 1912.
- (27) Birkhoff, G., and Zarantonello, E.H., Jets, Wakes and Cavities, Academic Press, 1957.
- (28) Hinze, J.O., Turbulence, McGraw-Hill, 1959.
- (29) Liepmann, H.W., Laufer, J., and Liepmann, K., "On the Spectrum of Isotropic Turbulence," N.A.C.A T.N. 2473, November 1951.
- (30) Batchelor, G.K., The Theory of Homogenous Turbulence, Cambr. Univ. Press, 1959.
- (31) Liepmann, H.W., and Robinson, M.S., "Counting Methods and Equipment for Mean-Value Measurements in Turbulence Research," N.A.C.A. T.N. 3037, October 1953.
- (32) Perkins, F.E., and Eagleson, P.S., "The Development of a Total Head Tube for High Frequency Pressure Fluctuations in Water," M.I.T. Hydro Lab. T.N. No. 5, 1959, and

Addendum, April 1960.

- (33) Morse, P.M., Vibration and Sound, McGraw-Hill, 1948, 235.

thesP386

An investigation of the early wake behin



3 2768 001 97809 1

DUDLEY KNOX LIBRARY